ABSTRACT

GHASSEMI, PEDRAM. Multilevel Quasidiffusion Methods with Hybrid Temporal Discretization for Thermal Radiative Transfer Problems. (Under the direction of Dmitriy Y. Anistratov).

In this work, a new hybrid temporal discretization of the multi-level quasidiffusion equations is presented for time-dependent multifrequency thermal radiative transfer problems in 2D. This is a mixed-order method that consists of a first-order scheme for the high-order radiative transfer equation and a second-order scheme for the low-order quasidiffusion equations. A monotonization procedure is applied to the second-order hyperbolic low-order equations. The numerical results show that the hybrid scheme generates a more accurate solution than the uniform first-order method. The monotonization procedure does well in removing the oscillatory behavior in the solution inherently produced by hyperbolic equations discretized with a high-resolution scheme. Approximate models of time dependence in the radiative transfer equation are presented and α-approximation is analyzed. The numerical results show that the radiative transfer equation in α-approximation evolves the temperature and radiation waves well while reducing the memory requirements by a significant amount. The solution obtained with this model deviates from that calculated with the time-dependent radiative transfer equation when the change rate is large and where there are significant transport effects.

Multilevel Quasidiffusion Methods with Hybrid Temporal Discretization for Thermal Radiative
Transfer Problems

by
Pedram Ghassemi

A dissertation submitted to the Graduate Faculty of
North Carolina State University
in partial fulfillment of the
requirements for the Degree of
Doctor of Philosophy

Nuclear Engineering

Raleigh, North Carolina

2019

APPROVED BY:

_____   _____
Yousry Y. Azmy   Steve Shannon

_____   _____
Carl Kelley   Dmitriy Y. Anistratov
                                                                   Chair of Advisory Committee

DEDICATION

To Farshid and Nazila

ACKNOWLEDGEMENTS

TABLE OF CONTENTS

LIST OF TABLES

LIST OF FIGURES

vii

viii

LIST OF ALGORITHMS

CHAPTER

1

INTRODUCTION

There exists a wide class of problems where the transport of particles must be described to correctly simulate physical processes. This includes important areas of research such as astrophysics, plasma physics, nuclear reactor physics, and atmospheric science. Due to the complex nature of these problems, numerical simulations are required to accurately and efficiently model these phenomena and to achieve this, one must solve the transport equation. Specifically, the focus of this work is on radiative transfer problems. This introduction outlines the motivation, challenges, and previous efforts contributed to this area of research and then states the research items of interest.

1.1 Motivation

There is a strong motivation arising from the abundant applications that are modeled with the equations of radiative transfer. This ranges from high temperature combustion phenomena to lower temperature applications where the effects of radiative energy cannot be neglected. Radiative transfer problems became important first in astrophysics [1, 2]. In a field that does not have the luxury of laboratory experiments, detailed radiation transport is the only means of understanding the physics of these radiation dominated objects and astrophysical phenomena. Some examples of what scientists are interested in modeling are the formation, evolution, and death of stars, supernova core-collapse, and accretion disks near super massive black holes. The

need for solving radiative transfer problems began to spread into other areas as well.

There are multiple applications in the nuclear engineering field that are interested in this type of problem. The exchange between radiation and matter must be modeled with the interaction of the combustible rods and the surrounding heat conducting fluid. High energy density physics is another area of interest. With the start of research for nuclear fusion reactors, there became a need to model particle transport for inertial confinement fusion. This could be for either direct drive through photon or ion beams or with indirect drive via thermal photons in a hohlraum. It is also applicable to describing radiative transfer phenomena in the Tokamak or other magnetic confinement devices as well.

In atmospheric sciences, radiation interacts with different types of matter: gaseous, aqueous, particles, and surfaces [3]. Cloud variability and radiative transfer play a key role in understanding climate. Coupling radiative transfer with cloud fields is one example; another is coupling to plant canopies and the oceans. These problems consider different scales such as the wave spectra of solar and terrestrial radiation fields as well as the emission spectra of the Sun and Earth. Another application is related to the observation of Earth with satellites. This is used to estimate various quantities that drive climate change as well.

Glass manufacturing also involves temperatures high enough that radiation contributes to the exchange of energy. Other applications at a lower temperature scale also have effects that require the modeling of energy exchange due to radiative transfer. The design of ceilings and building insulation takes this phenomena into account when trying to reduce the amount of heat draining. This is only part of the research areas that require the detailed solution of radiative transfer problems.

1.2 Thermal Radiative Transfer Problems

The interaction of radiation and matter is a fundamental process that occurs in a variety of complex models. In thermal radiative transfer (TRT) problems, photons are absorbed and emitted by the material and both of these processes change the material temperature. Thermal radiation is radiation that is emitted by matter in a state of thermal excitation. If a region is in thermal equilibrium, the energy distribution can be described by the Planck function. Generally, this is not the case, and therefore it is necessary to solve a radiation transfer equation [4]. The radiative transfer equation describes the propagation, emission, scattering, and absorption of light. It is coupled with the energy balance equation which accounts for the effect of energy exchange on the temperature. The spectral radiative transfer (RT) equation in the absence of scattering and hydrodynamic motion is given by,

2

$$\frac{1}{c}\frac{\partial I_\nu(\boldsymbol{r},\boldsymbol{\Omega},\nu,t)}{\partial t} + \boldsymbol{\Omega}\cdot\boldsymbol{\nabla}I_\nu(\boldsymbol{r},\boldsymbol{\Omega},\nu,t) + \varkappa_\nu(\nu,T)I_\nu(\boldsymbol{r},\boldsymbol{\Omega},\nu,t) = \varkappa_\nu(\nu,T)B_\nu(\nu,T)\,, \qquad (1.1)$$

$$r \in G,\ \ \text{for all } \boldsymbol{\Omega},\ \ t \geq t_0,\ \ 0 \leq \nu < +\infty, \qquad (1.2)$$

with initial and boundary conditions,

$$I_\nu|_{t=t_0} = I_\nu^0,\ \ \text{for } r \in G \text{ and all } \boldsymbol{\Omega}, \qquad (1.3)$$

$$I_\nu|_{r=r_\gamma} = I_\nu^{in},\quad \text{for } r_\gamma \in \partial G \text{ and } \boldsymbol{\Omega}\cdot\boldsymbol{e}_n < 0,\ \ t \geq t_0, \qquad (1.4)$$

where G is the spatial domain of the problem,

$$G = [0 \leq x \leq X, 0 \leq y \leq Y]\,, \qquad (1.5)$$

and the Planck function is,

$$B_\nu(T) = \frac{2h\nu^3}{c^2}\left(e^{\frac{h\nu}{kT}} - 1\right)^{-1}\,, \qquad (1.6)$$

which is the distribution of black-body radiation. $I_\nu(\boldsymbol{r},\boldsymbol{\Omega},\nu,t)$ is the specific intensity of radiation, $\varkappa_\nu(\nu,T)$ is the spectral opacity. $\boldsymbol{r}$ is the position in space, ν is the photon frequency, $\boldsymbol{\Omega}$ is the direction of motion, and t is time. The energy balance (EB) equation without heat conduction is defined as,

$$\frac{\partial\varepsilon(T)}{\partial t} = \int_0^\infty \int_{4\pi} \varkappa_\nu(\nu,T)\Big(I_\nu(\boldsymbol{r},\boldsymbol{\Omega},\nu,t) - B_\nu(\nu,T)\Big)d\Omega d\nu\,, \qquad (1.7)$$

with the initial condition,

$$T(\boldsymbol{r},t)|_{t=t_0} = T^0(\boldsymbol{r}),\ \ \text{for } r \in G, \qquad (1.8)$$

where $\varepsilon(T)$ is the material energy density which is a known nonlinear function of material temperature.

1.3 Challenges

There are many obstacles one faces when solving radiative transfer problems. One feature that creates difficulty is the high dimensionality of the problem. The radiative transfer equation has 7 independent variables: three dimensions in space (x, y, z), two dimensions in angle (θ, ϕ), frequency, and time. When possible, approximations to the transfer equation are used to decrease the computational expense while minimizing the loss of accuracy in the solution. Some examples are solving a steady state equation that has no time dependence, a diffusion equation

3

which has no angular dependence, and grey equation which has no frequency dependence.

Another challenge is the radiative transfer problem encompasses different spatial and time scales. If the mean free path is much smaller than the characteristic length of the material and absorption is very small then the radiation field is virtually isotropic. In this regime, the radiative transfer equation can be approximated using the diffusion approximation. When modeling radiative transfer in a transparent medium, a different regime is entered that requires the radiative transfer equation because the radiation field is no longer isotropic and it requires nonlocal treatment. There are methods that perform well for each scale, but the difficulty lies in finding a method that performs well everywhere.

TRT problems are also highly nonlinear. In thermal equilibrium, the total radiation energy density is proportional to T^4. In addition, all material properties depend on the solution (temperature) which is changing due to both the absorption and emission of photons. For most problems, it is necessary to couple other physics to the radiative transfer equation which is another source of nonlinearity. In this class of problems, the transfer equation becomes a part of a complicated nonlinear system of multi-physics equations. The dimensionality of this multi-physics problem is determined by the dimensionality of the transfer equation.

Another challenge comes from the discretization of the TRT equations. High resolution discretization methods are desirable because they give a more accurate solution, but as a consequence they add complexity to the problem. Godonov's theorem states a two-level uniform linear scheme for approximating the advection (transport) equation is monotonic only if it is first order accurate [5]. A higher order scheme can produce artificial oscillations in the solution. Another requirement is then to apply a montonization procedure that adequately suppresses oscillations while maintaining a higher accuracy solution compared to the first order method.

1.4   History of Methods for TRT Problems

There are a variety of methods used to solve TRT problems and these are categorized as either stochastic or deterministic. A stochastic method possesses intrinsic randomness of particle transport phenomena. For stochastic methods, the implicit Monte Carlo (IMC) method has been the workhorse for many decades in this area. This method was developed by Fleck and Cummings as a solution methodology for frequency and time dependent TRT problems [6]. The previously proposed Monte Carlo methods had difficulties in optically thick regions and systems near thermal equilibrium [7, 8] which would require extremely small time steps to correctly resolve physics. IMC addresses these issues by calculating radiation and material energy fields implicitly by treating the absorption and emission of photons as a fission-like source that is converged on a given time level. This method is stable and can handle both optically thick and thin regimes.

4

There is also a wide range of approaches for solving TRT problems using deterministic methods. There is work ranging from radiation diffusion calculations to S_N and P_N transport methods as well. A class of methods used to solve these problems based on the quasidiffusion (QD) method which was introduced by Gol'din [9]. The QD method was developed for solving the linear Boltzmann transport equation. It is a two-level method that is formulated by a nonlinear system of equations consisting of the high-order RT equation for the intensity and low-order equations for the angular moments of the intensity. Gol'din and Chetverushkin used QD as a solution method for solving radiation hydrodynamics problems [10]. These problems involve the coupling of hydrodynamics equations with the radiative transfer equation. The solution of the hydrodynamics equations are dependent only on space and time; whereas, the solution to the radiative transfer equation depends of frequency and angle as well. Coupling is done through radiative energy flux which can be efficiently determined from equations that do not depend on frequency or angle. The high-order transport solution is used to define the QD tensor (also known as Eddington tensor). The QD factors are elements of the QD tensor. The multigroup QD equations can be reduced to a grey problem by averaging with respect to energy. The multigroup equations give a more accurate solution because it accounts for the spectral dependence of the opacities and source. This is the earliest example of multiphysics coupling using the QD method. The benefit is that the coupling is done in the lowest dimensional space possible without approximation of the equations. Gol'din, Gol'dina, Kolpakov, and Shilkov further developed the multilevel QD method for radiative hydrodynamics that involves also a methodology for multiphysics coupling based on multigroup and grey low-order QD equations [11, 12]. This multi-level QD methodology was applied to high-energy density physics problems in general 1D geometry.

Stone, Mihalas, and Norman developed independently such a method (referred to as Variable Eddington factor method) to evolve the radiative transfer equations for astrophyiscal flows in two dimensions [13]. One-dimensional calculations are not adequate for modeling some astrophysical phenomena such as accretion flows onto compact objects or radiatively driven winds from hot stars. Before this, multi-dimensional calculations used the diffusion approximation which is only valid in optically thick regions and also require flux limiters. The QD method does not require flux limiters and is valid in optically thick and thin regions because it is a full transport algorithm. The QD factors are obtained by solving a steady state, frequency integrated RT equation using the method of short characteristics. A cylindrical coordinate system is used. While it is possible to obtain a consistent solution between the RT equation and moment equations, this is unnecessary for multi-dimensional calculations. The QD factors are a measure of the anisotropy of the radiation field and can account for the transport equations when solving the radiation moment equations [14–16]. In some cases, the factors can be lagged in time if the system is not evolving on a radiation flow time scale. The results show the method does

5

well in the streaming limit as well as the diffusion limit which improves upon the previous multi-dimensional diffusion method.

Anistratov, Aristova, and Gol'din developed a multi-level QD method for TRT problems [17]. This consists of (i) the radiative transfer equation (ii) the multigroup QD equations and (iii) the grey QD equations coupled with the energy balance equation. A Frechet derivative is introduced which approximates the change in opacity with respect to temperature. Results showed it reduces the number of iterations by a significant amount. Aristova, Gol'din, and Kolpakov extended the multi-level QD method to 2D r-z geometry [18]. They also proposed a monotonic scheme for the low-order QD (LOQD) equations in r-z. Aristova used this QD method to simulate radiation transport in a channel [19]. Park, Knoll, Rauenzahn, Wollaber, and Densmore derive a general consistency term for the QD equations [20]. Anistratov performed stability analysis of multilevel QD method with independent discretization of high-order RT equation and low-order QD equations that demonstrated effectiveness of the iteration scheme of this method [21].

Morel, Larsen, and Matzen developed a linear synthetic acceleration method for 1-D multi-group radiation diffusion calculations which accelerates convergence using a one-group, or grey, diffusion equation [22]. Synthetic acceleration methods have been used extensively for neutron transport calculations [23–25]. This method is compared to the standard nonlinear multifrequency-grey acceleration method [26]. Alcouffe, Clark, and Larsen extend this work to accelerate transport iterations with the diffusion synthetic acceleration (DSA) method for TRT problems [27]. They introduced an additional multifrequency-grey problem that consists of frequency-dependent diffusion equations as well as a grey equation to accelerate the convergence. There is a linear and nonlinear variant of these methods. Fourier analysis shows this method has better convergence properties than source iterations and numerical results show the nonlinear and linear versions perform similarly in regards to acceleration. Consistent discretization between the multifrequency transport equations and multifrequency and grey diffusion equations is required for stability. This work was done for 1-D slab geometry as well. Larsen developed a grey transport acceleration method [28] for solving multifrequency TRT problems which improves on the standard source iteration method by additionally solving a grey RT equation. Morel, Yang, and Warsa recast the linear multifrequency-grey acceleration [29] in terms of a preconditioned Krylov method to resolve the degradation in convergence of iterations when applied to multidimensional problems or with significant material discontinuities. These issues were seen when using DSA as well. Banoczi and Kelley developed and analyzed a multi-level algorithm for conductive-radiative heat transfer equations [30] and this work was also extended to 2D [31].

McClarren, Holloway, and Brunner develop a spherical harmonics (P_N) method for TRT problems [32] in both 1D and 2D. The P_7 approximation reproduces most of the transport

6

effects. In 2D, the P_N method cannot guarantee a positive solution, but this result is mitigated by increase the order of expansion. McClarren, Evans, Lowrie, and Densmore presented a semi-implicit time integration scheme for the P_N equations for TRT problems [33]. They use a second-order Runge-Kutta scheme that treats the material coupling implicitly and the streaming term explicitly. This method allows for cheap computation at the cost of a time-step size restriction.

1.5 Significance and Novelty

This works focuses on a specific class of TRT problems. The geometry of interest is two-dimensional Cartesian. The discretization methods are developed for orthogonal spatial grids and the problem is frequency dependent. The radiative equation is discretized in angle using discrete ordinates. Various spatial approximations are used, ranging from robust first-order schemes like the subcell step method to high-order methods like simple corner balance. The low-order equations are discretized in space using the finite volume method. The focus of this work is the time discretization schemes for multi-level QD methods. Previous work uses α-approximation rather than the time-dependent high-order radiative transfer equation. A fully-implicit method in time is applied to the transport equation. The low-order equations are discretized using the θ-method which allows for high-order schemes. The opacities will be treated implicitly which means they are evaluated using the temperatures from the current time step. This approach is referred to as an implicitly balanced method [34].

The goal of this project is to develop an accurate and efficient computational methods for solving TRT problems. This work is based on the multi-level quasidiffusion method. The main results are:

1. Development of an approximation for the multi-level system of QD equations based on first-order accurate temporal-discretization schemes.

2. Development of a hybrid (mixed-order) temporal discretization of multi-level system of QD equations.

3. Development of a monotonization method for high-order schemes for approximating the hyperbolic time-dependent low-order QD equations.

4. Development and analysis of an approximation of time dependency in the radiative transfer equation for TRT problems based on multi-level QD method.

It is apparent that there is great motivation to solve this challenging problem. To understand the significance of the main results, it is important to highlight the beneficial features of the

7

multi-level QD method [9, 11, 17, 18]. Firstly, this method converges rapidly for thermal radiative transfer problems. The convergence rate is approximately the same as other rapidly converging acceleration methods such as DSA [35]. While there are other methods that exhibit similar efficiency in this respect, the performance of the QD method is realized without the restraint of consistent discretization of the high-order and low-order equations. This feature allows for extensive flexibility in development of discretization methods for different types of problems [36]. The versatility of this method is exploited to improve the accuracy and efficiency of an already well-performing scheme.

The efficiency of the multi-level QD method goes beyond just convergence of iterations. It reduces the dimensionality of the problem with respect to both the angular and energy dependence. Since the closures are exact, there are no approximations made to the RT equation. In addition, it is seldom that the transfer does not require coupling to other physics. The solution to most of these problems are dependent only on space and time. This method allows for very efficient coupling in a space of similar dimensionality as other equations [11, 17, 18, 37] and mimic tightly coupled physics.

The results of this research were presented at:

1. Winter Meeting of American Nuclear Society (ANS) in Washington DC (November 2015) in the technical section on Transport Methods of Math & Comp. Division,

2. Annual Meeting of ANS in Philadelphia (June 2018) in the technical section on Transport Methods of Math & Comp. Division,

3. Scientific Seminar at Lawrence Livermore National Laboratory (October 23, 2018),

and are published in [38, 39].

The remainder of this dissertation is organized as follows: in Chapter 2, the multi-level QD equations for TRT problems are formulated. This includes the discretization methods used to approximate the equations as well as the algorithm for solving the multi-level QD equations. In Chapter 3, new temporal discretization methods for the multi-level QD equations are introduced. This includes a first-order and hybrid temporal discretization in addition to a monotonization procedure for the second-order temporal discretization method. In Chapter 4, approximation models of time dependence in the RT equation are developed and analyzed. In Chapter 5, iterations of the multi-level QD methods are analyzed. The final chapter is the conclusion of this work.

CHAPTER

$$2$$

MULTI-LEVEL QD METHOD FOR TRT PROBLEMS

In this chapter, the multi-level QD method for TRT problems is formulated. Then, the discretization methods used to approximate these equations are detailed. The RT equation is discretized in time using the backward-Euler method and discretized in space using several different schemes. The multigroup low-order QD equations are discretized in time using the backward-Euler and Crank-Nicolson methods and in space using a finite-volume method. The grey low-order equations are consistently discretized with the multigroup low-order equations and coupled with the energy balance equation.

2.1   Formulation of the QD Method

The spectral radiative transfer equation (1.1) is discretized in frequency using the multigroup approximation. The multigroup RT equation is solved for the group intensity and is obtained by integrating Equation (1.1) over frequency interval $\nu_g < \nu < \nu_{g+1}$,

$$\frac{1}{c}\frac{\partial I_g(\boldsymbol{r},\boldsymbol{\Omega},t)}{\partial t} + \boldsymbol{\Omega}\cdot\boldsymbol{\nabla}I_g(\boldsymbol{r},\boldsymbol{\Omega},t) + \varkappa_{E,g}(T)I_g(\boldsymbol{r},\boldsymbol{\Omega},t) = \varkappa_{pl,g}(T)B_g(T)\,, \qquad (2.1)$$

9

with initial (2.2) and boundary conditions (2.3),

$$I_g(\boldsymbol{r}, \boldsymbol{\Omega}, 0) = I_{g,0}, \quad \boldsymbol{r} \in G, \tag{2.2}$$

$$I_g(\boldsymbol{r}_b, \boldsymbol{\Omega}, t) = I_{g,in}, \quad r_b \in \partial G, \quad t \geq t_0, \tag{2.3}$$

The group intensity (2.4) and group Planckian function (2.5) are defined as,

$$I_g(\boldsymbol{r}, \boldsymbol{\Omega}, t) = \int_{\nu_g}^{\nu_{g+1}} I_\nu(\boldsymbol{r}, \boldsymbol{\Omega}, \nu, t) d\nu, \tag{2.4}$$

$$B_g(T) = \int_{\nu_g}^{\nu_{g+1}} B_\nu(\nu, T) d\nu, \tag{2.5}$$

and the group opacities (2.6) and (2.7) are,

$$\varkappa_{E,g}(T) = \frac{\int_{\nu_g}^{\nu_{g+1}} \varkappa_\nu(\nu, T) B_\nu(\nu, T_r) d\nu}{\int_{\nu_g}^{\nu_{g+1}} B_\nu(\nu, T_r) d\nu}, \tag{2.6}$$

$$\varkappa_{pl,g}(T) = \frac{\int_{\nu_g}^{\nu_{g+1}} \varkappa_\nu(\nu, T) B_\nu(\nu, T) d\nu}{\int_{\nu_g}^{\nu_{g+1}} B_\nu(\nu, T) d\nu}. \tag{2.7}$$

The group opacity, $\varkappa_{E,g}$, should be computed with the spectral intensity, I_ν, as the averaging function, but this function is unknown. Instead, it is averaged with the Planck function evaluated at the temperature of radiation, T_r, which is defined by some approximation. $\varkappa_{pl,g}$ is averaged with the Planck function evaluated at the material temperature, T.

The multigroup low-order quasidiffusion (MLOQD) equations are obtained by taking the zeroth and first angular moments of the multigroup radiative transfer equation. These equations are solved for the angular moments of the RT equation. The MLOQD equations are defined as,

$$\frac{\partial E_g(\boldsymbol{r}, t)}{\partial t} + \boldsymbol{\nabla} \cdot \boldsymbol{F}_g(\boldsymbol{r}, t) + c\varkappa_{E,g}(T) E_g(\boldsymbol{r}, t) = 4\pi \varkappa_{pl,g}(T) B_g(T), \tag{2.8}$$

$$\frac{1}{c} \frac{\partial \boldsymbol{F}_g(\boldsymbol{r}, t)}{\partial t} + c\boldsymbol{\nabla} \cdot \boldsymbol{f}_g(\boldsymbol{r}, t) E_g(\boldsymbol{r}, t) + \varkappa_{ros,g}(T) F_g(\boldsymbol{r}, t) = 0, \tag{2.9}$$

with initial (2.10) and boundary (2.11) conditions,

$$E_g(\boldsymbol{r}, t)|_{t=t_0} = E_g^0(\boldsymbol{r}), \quad \boldsymbol{F}_g(\boldsymbol{r}, t)|_{t=t_0} = \boldsymbol{F}_g^0(\boldsymbol{r}), \quad \text{for } \boldsymbol{r} \in G \tag{2.10}$$

$$\boldsymbol{n} \cdot \boldsymbol{F}_g(\boldsymbol{r}_\gamma, t) = cC_{g,n}(\boldsymbol{r}_\gamma, t)(E_g(\boldsymbol{r}, t) - E_{g,in}(\boldsymbol{r}_\gamma, t)) + F_{g,in}(\boldsymbol{r}_\gamma, t), \quad r_\gamma \in \partial G, \quad t \geq t_0, \tag{2.11}$$

10

where the zeroth angular moment is the group radiation energy density,

$$E_g(\boldsymbol{r}, t) = \frac{1}{c} \int_{4\pi} I_g(\boldsymbol{r}, \boldsymbol{\Omega}, t) d\Omega, \tag{2.12}$$

and the first angular moment is the group radiative flux,

$$\boldsymbol{F}_g(\boldsymbol{r}, t) = \int_{4\pi} \boldsymbol{\Omega} I_g(\boldsymbol{r}, \boldsymbol{\Omega}, t) d\Omega. \tag{2.13}$$

The system of equations is closed exactly with the QD tensor (2.14) which is also known as the Eddington tensor,

$$\boldsymbol{f}_g(\boldsymbol{r}, t) = \frac{\int_{4\pi} \boldsymbol{\Omega}\boldsymbol{\Omega} I_g(\boldsymbol{r}, \boldsymbol{\Omega}, t) d\Omega}{\int_{4\pi} I_g(\boldsymbol{r}, \boldsymbol{\Omega}, t) d\Omega}. \tag{2.14}$$

where the components of the tensor have the form,

$$f_{\alpha\beta,g}(\boldsymbol{r}, t) = \frac{\int_{4\pi} \Omega_\alpha \Omega_\beta I_g(\boldsymbol{r}, \boldsymbol{\Omega}, t) d\Omega}{\int_{4\pi} I_g(\boldsymbol{r}, \boldsymbol{\Omega}, t) d\Omega}. \tag{2.15}$$

The boundary factor (2.16) is defined as,

$$C_{g,n}(\boldsymbol{r}_\gamma, t) = \frac{\int_{(\boldsymbol{n}\cdot\boldsymbol{\Omega})>0} (\boldsymbol{n} \cdot \boldsymbol{\Omega}) I_g(\boldsymbol{r}, \boldsymbol{\Omega}, t) d\Omega}{\int_{(\boldsymbol{n}\cdot\boldsymbol{\Omega})>0} I_g(\boldsymbol{r}, \boldsymbol{\Omega}, t) d\Omega}. \tag{2.16}$$

The nonlinearity of this method stems from the QD and boundary factors dependence on the intensity. Because the factors weakly depend on the solution of the high-order problem, iterations converge rapidly for different types of problems. The initial group energy density and group radiative flux is,

$$E_g^0(\boldsymbol{r}) = \frac{1}{c} \int_{4\pi} I_g^0(\boldsymbol{r}, \boldsymbol{\Omega}) d\Omega, \tag{2.17}$$

$$\boldsymbol{F}_g^0(\boldsymbol{r}) = \int_{4\pi} \boldsymbol{\Omega} I_g^0(\boldsymbol{r}, \boldsymbol{\Omega}) d\Omega, \tag{2.18}$$

and the incoming group energy density and group radiative flux is,

$$E_{g,in}(\boldsymbol{r}_\gamma, t) = \frac{1}{c} \int_{(\boldsymbol{n}\cdot\boldsymbol{\Omega})<0} I_{g,in}(\boldsymbol{r}_\gamma, \boldsymbol{\Omega}, t) d\Omega, \tag{2.19}$$

$$\boldsymbol{F}_{g,in}(\boldsymbol{r}_\gamma, t) = \int_{(\boldsymbol{n}\cdot\boldsymbol{\Omega})<0} \boldsymbol{\Omega} I_{g,in}(\boldsymbol{r}_\gamma, \boldsymbol{\Omega}, t) d\Omega. \tag{2.20}$$

Note that in the first moment equation, the Rosseland opacity is used instead of the standard

11

absorption opacity. The group Rosseland opacity (2.21) is defined as,

$$\varkappa_{ros,g}(T) = \left(\frac{\int_{\nu_g}^{\nu_{g+1}} \left(\varkappa_\nu(\nu, T) \right)^{-1} \frac{dB_\nu(\nu, T_r)}{dT} d\nu}{\int_{\nu_g}^{\nu_{g+1}} \frac{dB_\nu(\nu, T_r)}{dT} d\nu} \right)^{-1}, \tag{2.21}$$

where the reciprocal of the opacity is averaged with the derivative of the Planck function with respect to temperature evaluated at the temperature of radiation. The Rosseland opacity is used to guarantee the correct flux is yielded in the equilibrium diffusion limit [40] and is derived for these equations in this regime.

The MLOQD equations are collapsed in energy thus formulating the effective grey low-order quasidiffusion (GLOQD) equations. This is the level in which the radiative transfer problem is coupled with the energy balance (EB) equation. The effective GLOQD equations are,

$$\frac{\partial E(\boldsymbol{r}, t)}{\partial t} + \boldsymbol{\nabla} \cdot \boldsymbol{F}(\boldsymbol{r}, t) + c\bar{\varkappa}_E(T)E(\boldsymbol{r}, t) = c\bar{\varkappa}_{pl}(T)a_R T^4, \tag{2.22}$$

$$\frac{1}{c}\frac{\partial \boldsymbol{F}(\boldsymbol{r}, t)}{\partial t} + c\boldsymbol{\nabla} \cdot \bar{\boldsymbol{f}}(\boldsymbol{r}, t)E(\boldsymbol{r}, t) + \bar{\varkappa}_{ros}(T)\boldsymbol{F}(\boldsymbol{r}, t) + \eta(\boldsymbol{r}, t)E(\boldsymbol{r}, t) = 0, \tag{2.23}$$

with initial (2.24) and boundary (2.25) conditions,

$$E(\boldsymbol{r}, t)|_{t=t_0} = E^0(\boldsymbol{r}), \quad \boldsymbol{F}(\boldsymbol{r}, t)|_{t=t_0} = \boldsymbol{F}^0(\boldsymbol{r}), \quad \text{for } \boldsymbol{r} \in G \tag{2.24}$$

$$\boldsymbol{n} \cdot \boldsymbol{F}(\boldsymbol{r}_\gamma, t) = c\bar{C}_n(\boldsymbol{r}_\gamma, t)(E(\boldsymbol{r}, t) - E_{in}(\boldsymbol{r}_\gamma, t)) + F_{in}(\boldsymbol{r}_\gamma, t), \quad r_\gamma \in \partial G, \quad t \geq t_0, \tag{2.25}$$

coupled with the EB equation,

$$\frac{\partial \varepsilon(T)}{\partial t} = c\bar{\varkappa}_E(T)E(\boldsymbol{r}, t) - c\bar{\varkappa}_{pl}(T)a_R T^4, \tag{2.26}$$

where the total radiation energy density is,

$$E(\boldsymbol{r}, t) = \sum_{g=1}^{N_g} E_g(\boldsymbol{r}, t) \tag{2.27}$$

the total radiative flux is,

$$\boldsymbol{F}(\boldsymbol{r}, t) = \sum_{g=1}^{N_g} \boldsymbol{F}_g(\boldsymbol{r}, t), \tag{2.28}$$

and $\varepsilon(T)$ is the material energy density. a_R is Stefan's constant. The grey QD and boundary

12

factors averaged such that,

$$\bar{f}_{\alpha\beta}(\boldsymbol{r},t) = \frac{\sum_{g=1}^{N_g} f_{\alpha\beta,g}(\boldsymbol{r},t)E_g(\boldsymbol{r},t)}{\sum_{g=1}^{N_g} E_g(\boldsymbol{r},t)}, \tag{2.29}$$

$$\bar{C}_n(\boldsymbol{r}_\gamma,t) = \frac{\sum_{g=1}^{N_g} C_{n,g}(\boldsymbol{r}_\gamma,t)\left(E_g(\boldsymbol{r}_\gamma,t) - E_g^{in}(\boldsymbol{r}_\gamma,t)\right)}{\sum_{g=1}^{N_g}\left(E_g(\boldsymbol{r}_\gamma,t) - E_g^{in}(\boldsymbol{r}_\gamma,t)\right)}, \tag{2.30}$$

The initial total energy density and total radiative flux is,

$$E^0(\boldsymbol{r}) = \sum_{g=1}^{N_g} E_g^0(\boldsymbol{r}), \tag{2.31}$$

$$\boldsymbol{F}^0(\boldsymbol{r}) = \sum_{g=1}^{N_g} \boldsymbol{F}_g^0(\boldsymbol{r}), \tag{2.32}$$

and the incoming total energy density and total radiative flux is,

$$E_{in}(\boldsymbol{r}_\gamma,t) = \sum_{g=1}^{N_g} E_g^{in}(\boldsymbol{r}_\gamma,t), \tag{2.33}$$

$$\boldsymbol{F}_{in}(\boldsymbol{r}_\gamma,t) = \sum_{g=1}^{N_g} \boldsymbol{F}_g^{in}(\boldsymbol{r}_\gamma,t). \tag{2.34}$$

The grey opacities are defined such that,

$$\bar{\varkappa}_E(T) = \frac{\sum_{g=1}^{N_g} \varkappa_{E,g}(T)E_g(\boldsymbol{r},t)}{\sum_{g=1}^{N_g} E_g(\boldsymbol{r},t)}, \tag{2.35}$$

$$\bar{\varkappa}_{pl}(T) = \frac{\sum_{g=1}^{N_g} \varkappa_{pl,g}(T)B_g(T)}{\sum_{g=1}^{N_g} B_g(T)}, \tag{2.36}$$

$$\bar{\varkappa}_{ros}(T) = \frac{\sum_{g=1}^{N_g} \varkappa_{ros,g}(T)|\boldsymbol{F}_g(\boldsymbol{r},t)|}{\sum_{g=1}^{N_g} |\boldsymbol{F}_g(\boldsymbol{r},t)|}. \tag{2.37}$$

Since the radiative flux is an alternating function, it is possible that $\sum_{g=1}^{N_g} \boldsymbol{F}_g(\boldsymbol{r},t) = 0$. The corresponding term in the grey first-moment equation can be re-formulated such that,

$$\sum_{g=1}^{N_g} \varkappa_{ros,g}(T)\boldsymbol{F}_g(\boldsymbol{r},t) = \bar{\varkappa}_{ros}(T)\boldsymbol{F}(\boldsymbol{r},t) + \frac{\sum_{g=1}^{N_g}(\varkappa_{ros,g}(T) - \bar{\varkappa}_{ros}(T))\boldsymbol{F}_g(\boldsymbol{r},t)}{\sum_{g=1}^{N_g} E_g(\boldsymbol{r},t)}E(\boldsymbol{r},t). \tag{2.38}$$

13

This compensation term is defined as,

$$\eta(\boldsymbol{r}, t) = \frac{\sum_{g=1}^{N_g}(\varkappa_{ros,g}(T) - \bar{\varkappa}_{ros}(T))\boldsymbol{F}_g(\boldsymbol{r}, t)}{\sum_{g=1}^{N_g} E_g(\boldsymbol{r}, t)}. \tag{2.39}$$

which leads to the following closure,

$$\sum_{g=1}^{N_g} \varkappa_{ros,g}(T)\boldsymbol{F}_g(\boldsymbol{r}, t) = \bar{\varkappa}_{ros}(T)\boldsymbol{F}(\boldsymbol{r}, t) + \eta(\boldsymbol{r}, t)E(\boldsymbol{r}, t). \tag{2.40}$$

The dimensionality of the problem has been reduced as the solution to these equations no longer depend on frequency or angle. The GLOQD problem is now coupled to the energy balance equation with an equation of similar dimensionality. The nonlinear coupling is simplified immensely by doing so in this reduced dimensional space.

2.2 Discretization of the High-Order Radiative Transfer Equation

The multigroup RT equation (2.1) is dependent on angle, time, and space. Discrete ordinates, or the S_N method [41], is used to discretize the RT equation in angle. This approximation consists of solving (2.1) only for a distinct number of directions. The multigroup RT equation discretized in angle is,

$$\frac{1}{c}\frac{\partial I_{g,m}(\boldsymbol{r}, t)}{\partial t} + \boldsymbol{\Omega}_m \cdot \boldsymbol{\nabla} I_{g,m}(\boldsymbol{r}, t) + \varkappa_{E,g}(T)I_{g,m}(\boldsymbol{r}, t) = \varkappa_{pl,g}(T)B_g(T), \tag{2.41}$$

where the m index indicates the direction of motion of particles.

2.2.1 Backward-Euler Temporal Discretization Method

The RT equation (2.41) is discretized in time using the backward-Euler (B-E) scheme,

$$\frac{1}{c}\frac{I_{g,m}^n(\boldsymbol{r}) - I_{g,m}^{n-1}(\boldsymbol{r})}{\tau^n} + \boldsymbol{\Omega}_m \cdot \boldsymbol{\nabla} I_{g,m}^n(\boldsymbol{r}) + \varkappa_{E,g}^n(T)I_{g,m}^n(\boldsymbol{r}) = \varkappa_{pl,g}^n(T)B_g^n(T), \tag{2.42}$$

where $\tau^n = t^n - t^{n-1}$ and the opacities and Planckian source are evaluated at the current time step. This fully implicit method is first-order accurate. The terms in Equation (2.42) are rearranged and take the form of a steady state RT equation,

$$\boldsymbol{\Omega}_m \cdot \boldsymbol{\nabla} I_{g,m}^n(\boldsymbol{r}) + \left(\varkappa_{E,g}^n(T) + \frac{1}{c\tau^n}\right)I_{g,m}^n(\boldsymbol{r}) = \varkappa_{pl,g}^n(T)B_g^n(T) + \frac{I_{g,m}^{n-1}(\boldsymbol{r})}{c\tau^n} \tag{2.43}$$

14

The advantage of independent discretization of the high-order and low-order equations allows one to optimize the benefits of different approaches where possible. In regards to temporal discretization, alternate methods can be applied to the low-order problem in order to gain an increase in accuracy. Chapter 3 details the work done using mixed-order temporal discretizations for the whole system of multi-level QD equations. Another approach involves alternate treatments to the RT equation. Approximate models of time dependence can be used as a means to avoid temporal discretization of an equation with high dimensionality. Chapter 4 introduces new models of the time dependence of the transfer equation as well as analysis of previous models.

The flexibility of the QD method allows for a wide range of spatial discretizations of the RT equation. The subcell step method [42] and simple corner balance method [43] are described. To avoid complicated notation, the indices for groups and angles are omitted for the description of these methods. The steady-state RT equation (2.44) is presented in a compact form such that $\tilde{\varkappa}$ is the effective total opacity and S is the effective source term.

$$\boldsymbol{\Omega} \cdot \boldsymbol{\nabla} I(\boldsymbol{r}) + \tilde{\varkappa}(\boldsymbol{r}) I(\boldsymbol{r}) = S(\boldsymbol{r}) \,. \tag{2.44}$$

For the backward-Euler temporal discretization, the effective total opacity is defined as,

$$\tilde{\varkappa}(\boldsymbol{r}) = \varkappa_{E,g}^n(T) + \frac{1}{c\tau^n}, \tag{2.45}$$

and the effective source term is,

$$S(\boldsymbol{r}) = \varkappa_{pl,g}^n(T) B_g^n(T) + \frac{I_{g,m}^{n-1}(\boldsymbol{r})}{c\tau^n}. \tag{2.46}$$

Based on the treatment of time dependence in the RT equation, the definition of the effective opacity and source can vary. A 2D Cartesian spatial mesh is considered where the domain is defined over,

$$G = [0 \leq x \leq X, 0 \leq y \leq Y] \,. \tag{2.47}$$

Orthogonal spatial grids are considered. The indices i and j refer to the x and y-direction, respectively. The area of a cell (i,j) is defined as, $A_{ij} = \Delta x_i \Delta y_j$, where $\Delta x_i = x_{i+\frac{1}{2}} - x_{i-\frac{1}{2}}$ and $\Delta y_j = y_{j+\frac{1}{2}} - y_{j-\frac{1}{2}}$.

2.2.2 Subcell Step (SS) Method

The basic idea of subcell transport discretization schemes is to subdivide the spatial cell into subcells defined by characteristics going through cell vertices [42, 44, 45]. This class of subcell methods are shown to be robust even when extended to unstructured grids.

The rectangular cell (ij) is split into subcells along the streaming direction which creates 3

subcells: 2 triangles and 1 parallelogram. For each subcell, a local coordinate system (u,v) is defined such that the origin exists at the point joining the inflow and parallel to flow faces. The u-axis is defined along the given direction of particle motion in the 2D plane and the v-axis is perpendicular to the u-axis. Figure 2.1 shows the subcells formed by a particular streaming direction and the local coordinate system for the first triangle subcell in cell (ij). Equation (2.44) is reformulated on this local coordinate system,

$$\mu'\frac{\partial I(u,v)}{\partial u} + \tilde{\varkappa}(u,v)I(u,v) = S(u,v), \tag{2.48}$$

where μ' is given by,

$$\mu' = \sqrt{\Omega_x^2 + \Omega_y^2} = \sqrt{1 - \Omega_z^2} = \sin\theta, \tag{2.49}$$
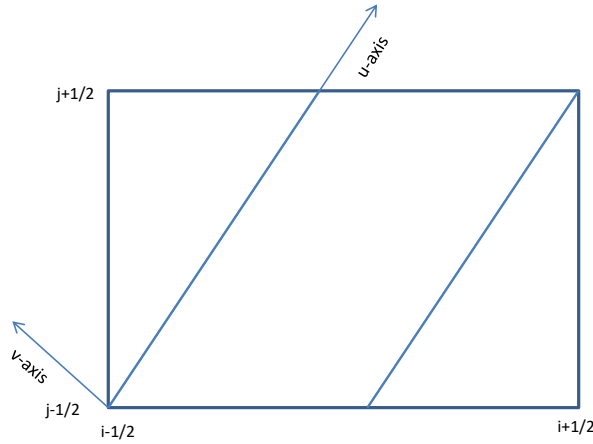
Figure 2.1 Subcells formed by a particular streaming direction and the local coordinate system for the first triangle subcell in cell (ij).

and Ω_x, Ω_y, and Ω_z are the components of $\boldsymbol{\Omega}$ that are defined for Cartesian geometry as follows:

$$\begin{aligned}
\Omega_x &= \sin\theta\cos\chi, \\
\Omega_x &= \sin\theta\cos\chi, \\
\Omega_x &= \cos\theta,
\end{aligned} \tag{2.50}$$

where $0 \le \theta \le \pi$ and $0 \le \chi \le 2\pi$. The effective opacity, $\tilde{\varkappa}(u,v) = \tilde{\varkappa}$, and source, $S(u,v) = S_A$, are constant in a cell. The subcell step method assumes the incoming intensity is constant along the incoming face of the subcell $I_{in}(v) = I_{in}$, and that the flux is constant in the interior and on

16

the outflow face of the subcell. In each subcell p, the subcell-averaged intensity is obtained by integrating the intensity over the subcell area, A_p,

$$I_{A,p} = \frac{1}{A_p} \int_0^{\Delta v_p} dv \int_{u_{in}(v)}^{u_{out}(v)} I(u,v) du, \tag{2.51}$$

where $u_{in}(v)$ is the inflow face of the subcell, $u_{out}(v)$ is the outflow face of the subcell, and Δv_p is the height of the subcell with respect to the v-axis. The face-averaged intensity is obtained by

$$I_{out,p} = \frac{1}{L_{out}} \int_0^{L_{out}} I_{out}(s_{out}) ds_{out}, \tag{2.52}$$

where s_{out} measures the distance along the outflow face and L_{out} is the length of the outflow face. It can be rewritten as,

$$I_{out,p} = \frac{1}{\Delta v_p} \int_0^{\Delta v_p} I(u_{out}(v), v) dv. \tag{2.53}$$

The auxiliary condition for the subcell step method is that it assumes,

$$I_{A,p} = I_{out,p}. \tag{2.54}$$

These quantities are defined for both the triangle and parallelogram case and the equations are derived for each type of subcell. For the triangle subcell, the inflow and outflow face are defined as,

$$u_{in}(v) = \gamma \Delta u \frac{v}{\Delta v}, \tag{2.55}$$

and,

$$u_{out}(v) = \Delta u (1 - (1 - \gamma) \frac{v}{\Delta v}), \tag{2.56}$$

where Δu is the base of the triangle, Δv is the height of the triangle, and γ is the ratio of $\frac{\Delta u}{\Delta v}$. The area of the triangle subcell is,

$$A_p = \frac{\Delta u \Delta v}{2}. \tag{2.57}$$

The equation for the subcell-averaged intensity is given by,

$$I_{A,p} = I_{out,p} = \frac{\frac{S_A \Delta u}{\mu'} + 2I_{in}}{\tau + 2}, \tag{2.58}$$

where I_{in} is the incoming intensity on the incoming face of the subcell, and τ is given by,

$$\tau = \frac{\tilde{\varkappa} \Delta u}{\mu'}. \tag{2.59}$$

17

For a parallelogram, the inflow and outflow face are defined as,

$$u_{in}(v) = \gamma \Delta u \frac{v}{\Delta v}, \tag{2.60}$$

$$u_{out}(v) = \gamma \Delta u \frac{v}{\Delta v} + \Delta u, \tag{2.61}$$

where Δu is the base of the parallelogram, Δv is the height of the parallelogram, and γ is the ratio of $\frac{\Delta u}{\Delta v}$. The area of the parallelogram subcell is,

$$A_p = \Delta u \Delta v. \tag{2.62}$$

The equation for the subcell intensity is given by,

$$I_{A,p} = I_{out,p} = \frac{\frac{S_A \Delta u}{\mu'} + I_{in}}{\tau + 1}, \tag{2.63}$$

where τ is given by,

$$\tau = \frac{\tilde{\varkappa} \Delta u}{\mu'}. \tag{2.64}$$

The cell-averaged intensity is calculated with an area-weighted average of each subcell averaged intensity such that,

$$I_A = \frac{I_{A,1} A_1 + I_{A,2} A_2 + I_{A,3} A_3}{A_1 + A_2 + A_3}, \tag{2.65}$$

where $A_1 + A_2 + A_3$ is equal to the area of the cell, A_{ij}. The face-averaged intensity on the outflow face of the cell is a length-weighted average of each subcell outflow intensity such that,

$$I_{out} = \frac{I_{out,1} u_{out,1} + I_{out,2} u_{out,2}}{u_{out,1} + u_{out,2}}, \tag{2.66}$$

where $u_{out,1} + u_{out,2}$ is equal to Δx_i or Δy_j depending on the face that shares two subcell faces. The main benefit of this method is that it is robust and cheap. This method is first order accurate and therefore preserves monotonicity. It also does not require the evaluation of expensive functions like exponentials and each subcell has one unknown. The downside is that this method is not very accurate and smears the solution in a cell. The unknowns for this method are 4 cell-face values, 1 cell-averaged value, and 3 subcell-averaged values.

2.2.3 Simple Corner Balance (SCB) Method

The Simple Corner Balance (SCB) method [43, 46–48] is a robust and accurate for optically thick problems on orthogonal grids. The SCB method for orthogonal grids in 2D is presented. Each cell in the grid is divided into rectangular subcells that are called corners which is shown

18

www.manaraa.com

in Figure 2.2. The corner, c, has two neighboring corners, c_1 and c_2. It also has 4 bounding surfaces: 2 inside the cell and 2 outside the cell. The inner surfaces are denoted as s_1 and s_2 which correspond to the neighboring corners, respectively. The outer surfaces are defined as c_+ and c_-. There are 16 unknowns within a cell: 4 corner-averaged intensities, 4 inner face-averaged intensities, and 8 outer face-averaged intensities.
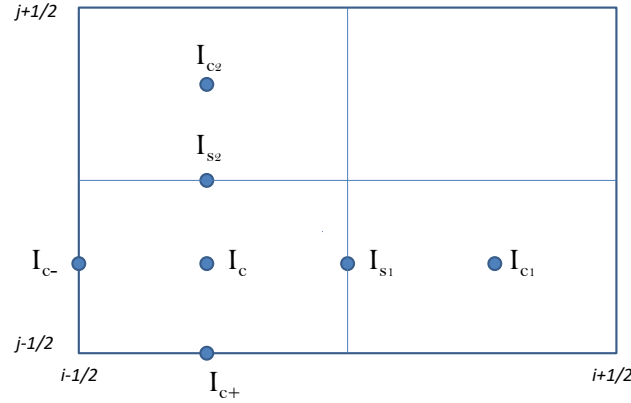
Figure 2.2 Cell unknowns of the SCB scheme.

The 2D RT equation is integrated over each corner which leads to 4 corner balance equations,

$$\frac{1}{2}\Omega_x \Delta y_j \left(I_{s_1} - I_{c_-}\right) + \frac{1}{2}\Omega_y \Delta x_i \left(I_{s_2} - I_{c_+}\right) + \frac{1}{4}\tilde{\varkappa}_{ij}A_{ij}I_c = \frac{1}{4}A_{ij}\tilde{S}_c, \qquad (2.67)$$

where I_c is the corner-averaged intensity, I_{c+} and I_{c-} are the face-averaged intensities on the outer faces, I_{s1} and I_{s2} are the face-averaged intensities on the inner faces, and $\tilde{S}_c$ is the effective source in corner c. One auxiliary condition relates the inner face-averaged intensities to the corner-averaged intensities such that,

$$I_{s1} = \frac{(I_c + I_{c1})}{2}, \quad I_{s2} = \frac{(I_c + I_{c2})}{2}, \qquad (2.68)$$

The other auxiliary condition used to close the system of equations is to relate the outgoing face-averaged intensities to the corner-averaged intensities through upwinding such that,

$$I_{c_\pm} = I_c, \quad \boldsymbol{n} \cdot \boldsymbol{\Omega} > 0, \qquad (2.69)$$

where $\boldsymbol{n}$ is the outward facing normal. Figure 2.3 shows the upwinding condition for $\Omega_x > 0$ and $\Omega_y > 0$. There are 4 corner balance equations, 4 equations for the inner faces, and 4 equations

19

for the outgoing faces. 4 outer face-averaged intensities are known from information from the downstream neighboring cell or boundary conditions. The cell-averaged intensity is obtained by averaging the 4 corner-averaged intensities and the cell face-averaged intensities are obtained by averaging the two outgoing face-averaged intensities on each corner that correspond to the face of the cell.
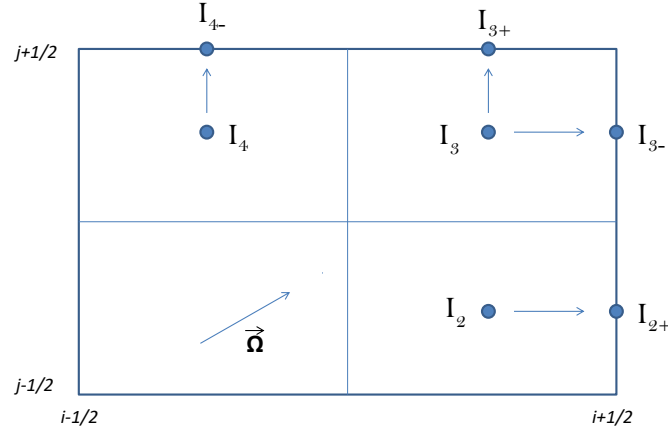
Figure 2.3 Upwinding condition for SCB scheme.

2.3 Discretization of Multigroup Low-Order QD Equations

The MLOQD equations are discretized in space using the finite volume method which is second order accurate. For each cell, there are 9 unknowns: 4 face-averaged energy densities, 4 face-averaged radiative fluxes, and 1 cell-averaged energy density. The spatially discretized zeroth moment equation is derived by integrating Equation (2.8) over the area of the cell,

$$
\frac{d}{dt}E_{ij}^g A_{ij} + \left(F_{x,i+\frac{1}{2}j}^g - F_{x,i-\frac{1}{2}j}^g\right)\Delta y_j
$$
$$
+ \left(F_{y,ij+\frac{1}{2}}^g - F_{y,ij-\frac{1}{2}}^g\right)\Delta x_i + c\varkappa_{E,ij}^g E_{ij}^g A_{ij} = Q_{pl,ij}^g A_{ij}, \tag{2.70}
$$

where the group cell-averaged Planckian source is,

$$
Q_{pl,g,ij}^g = 4\pi\varkappa_{pl,ij}^g B_{ij}^g \tag{2.71}
$$

and E_{ij}^g is the group cell-averaged energy density, $F_{x,i\pm 1/2,j}^g$ is the group face-averaged radiative flux in the x-direction, and $F_{y,i,j\pm 1/2}^g$ is the group face-averaged radiative flux in the y-direction,

20

and $\varkappa_{E,ij}^g$ is the group cell-average absorption opacity. For the first moment equations, Equation (2.9) is integrated over the left, right, bottom, and top halves of the cell and this gives 4 discrete first moment equations. The shaded regions of Figure 2.4 show the areas of integration.

$$\frac{1}{c}\frac{d}{dt}F_{x,i-\frac{1}{2}j}^g A_{ij} + c\Delta y_j\left(f_{xx,ij}^g E_{ij}^g - f_{xx,i-\frac{1}{2}j}^g E_{i-\frac{1}{2}j}^g\right)$$
$$+ \frac{c\Delta x_i}{2}\left(f_{xy,ij+\frac{1}{2}}^g E_{ij+\frac{1}{2}}^g - f_{xy,ij-\frac{1}{2}}^g E_{ij-\frac{1}{2}}^g\right) + \frac{1}{2}A_{ij}\varkappa_{ros,ij}^g F_{x,i-\frac{1}{2}j}^g = 0, \tag{2.72}$$
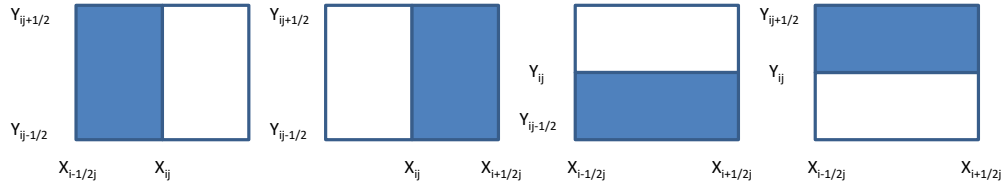
Figure 2.4 Areas of integration for Left, Right, Bottom, and Top first moment equations, respectively.

$$\frac{1}{c}\frac{d}{dt}F_{x,i+\frac{1}{2}j}^g A_{ij} + c\Delta y_j\left(f_{xx,i+\frac{1}{2}j}^g E_{i+\frac{1}{2}j}^g - f_{xx,ij}^g E_{ij}^g\right)$$
$$+ \frac{c\Delta x_i}{2}\left(f_{xy,ij+\frac{1}{2}}^g E_{ij+\frac{1}{2}}^g - f_{xy,ij-\frac{1}{2}}^g E_{ij-\frac{1}{2}}^g\right) + \frac{1}{2}A_{ij}\varkappa_{ros,ij}^g F_{x,i+\frac{1}{2}j}^g = 0, \tag{2.73}$$

$$\frac{1}{c}\frac{d}{dt}F_{y,ij-\frac{1}{2}}^g A_{ij} + c\Delta x_i\left(f_{yy,ij}^g E_{ij}^g - f_{yy,ij-\frac{1}{2}}^g E_{ij-\frac{1}{2}}^g\right)$$
$$+ \frac{c\Delta y_j}{2}\left(f_{xy,i+\frac{1}{2}j}^g E_{i+\frac{1}{2}j}^g - f_{xy,i-\frac{1}{2}j}^g E_{i-\frac{1}{2}j}^g\right) + \frac{1}{2}A_{ij}\varkappa_{ros,ij}^g F_{y,ij-\frac{1}{2}}^g = 0, \tag{2.74}$$

$$\frac{1}{c}\frac{d}{dt}F_{y,ij+\frac{1}{2}}^g A_{ij} + c\Delta x_i\left(f_{yy,ij+\frac{1}{2}}^g E_{ij+\frac{1}{2}}^g - f_{yy,ij}^g E_{ij}^g\right)$$
$$+ \frac{c\Delta y_j}{2}\left(f_{xy,i+\frac{1}{2}j}^g E_{i+\frac{1}{2}j}^g - f_{xy,i-\frac{1}{2}j}^g E_{i-\frac{1}{2}j}^g\right) + \frac{1}{2}A_{ij}\varkappa_{ros,ij}^g F_{y,ij+\frac{1}{2}}^g = 0. \tag{2.75}$$

21

$f^g_{\alpha\beta,ij}$ is the group cell-averaged QD factor where $\alpha, \beta = x, y$. $f^g_{\alpha\beta,i\pm1/2j}$ is the group face-averaged QD factor in the x-direction and $f^g_{\alpha\beta,ij\pm1/2}$ is the group face-averaged QD factor in the y-direction. $\varkappa^g_{ros,ij}$ is the group cell-averaged Rosseland opacity. A θ-weighted time integration scheme is applied to the spatial discretized equations (2.70-2.75) to get the MLOQD equations fully discretized in space and time. θ is a specified parameter that can range from zero to one. The zeroth moment equation is,

$$
\begin{aligned}
\left(F^{g,n}_{x,i+\frac{1}{2}j} - F^{g,n}_{x,i-\frac{1}{2}j} \right) \Delta y_j &+ \left(F^{g,n}_{y,ij+\frac{1}{2}} - F^{g,n}_{y,ij-\frac{1}{2}} \right) \Delta x_i \\
&+ \left(c\varkappa^{g,n}_{E,ij} + \frac{1}{\theta\tau^n} \right) E^{g,n}_{ij} A_{ij} = Q^{g,n}_{pl,ij} A_{ij} + \frac{A_{ij}}{\theta\tau^n} E^{n-1,g}_{ij} + G^{g,n-1}_{ij},
\end{aligned}
\tag{2.76}
$$

where,

$$
\begin{aligned}
G^{g,n-1}_{ij} = \frac{\theta-1}{\theta} &\left[\left(F^{g,n-1}_{x,i+\frac{1}{2}j} - F^{g,n-1}_{x,i-\frac{1}{2}j} \right) \Delta y_j \right. \\
&\left. + \left(F^{g,n-1}_{y,ij+\frac{1}{2}} - F^{g,n-1}_{y,ij-\frac{1}{2}} \right) \Delta x_i + \left(c\varkappa^{g,n-1}_{E,ij} E^{g,n-1}_{ij} - Q^{g,n-1}_{pl,ij} \right) A_{ij} \right].
\end{aligned}
\tag{2.77}
$$

The first moment equations are discretized such that the left moment equation is,

$$
\begin{aligned}
c\Delta y_j \left(f^{g,n}_{xx,ij} E^{g,n}_{ij} - f^{g,n}_{xx,i-\frac{1}{2}j} E^{g,n}_{i-\frac{1}{2}j} \right) &+ \frac{c\Delta x_i}{2} \left(f^{g,n}_{xy,ij+\frac{1}{2}} E^{g,n}_{ij+\frac{1}{2}} - f^{g,n}_{xy,ij-\frac{1}{2}} E^{g,n}_{ij-\frac{1}{2}} \right) \\
&+ \frac{1}{2} A_{ij} \left(\varkappa^g_{ros,ij} + \frac{1}{\theta c\tau^n} \right) F^{g,n}_{x,i-\frac{1}{2}j} = \frac{A_{ij}}{2\theta c\tau^n} F^{g,n-1}_{x,i-\frac{1}{2}j} + P^{g,n-1}_{L,ij},
\end{aligned}
\tag{2.78}
$$

where,

$$
\begin{aligned}
P^{g,n-1}_{L,ij} = \frac{\theta-1}{\theta} &\left[c\Delta y_j \left(f^{g,n-1}_{xx,ij} E^{g,n-1}_{ij} - f^{g,n-1}_{xx,i-\frac{1}{2}j} E^{g,n-1}_{i-\frac{1}{2}j} \right) \right. \\
&\left. + \frac{c\Delta x_i}{2} \left(f^{g,n-1}_{xy,ij+\frac{1}{2}} E^{g,n-1}_{ij+\frac{1}{2}} - f^{g,n-1}_{xy,ij-\frac{1}{2}} E^{g,n-1}_{ij-\frac{1}{2}} \right) + \frac{1}{2} A_{ij} \varkappa^{g,n-1}_{ros,ij} F^{g,n-1}_{x,i-\frac{1}{2}j} \right],
\end{aligned}
$$

the right moment equation is,

$$
\begin{aligned}
c\Delta y_j \left(f^{g,n}_{xx,i+\frac{1}{2}j} E^{g,n}_{i+\frac{1}{2}j} - f^{g,n}_{xx,ij} E^{g,n}_{ij} \right) &+ \frac{c\Delta x_i}{2} \left(f^{g,n}_{xy,ij+\frac{1}{2}} E^{g,n}_{ij+\frac{1}{2}} - f^{g,n}_{xy,ij-\frac{1}{2}} E^{g,n}_{ij-\frac{1}{2}} \right) \\
&+ \frac{1}{2} A_{ij} \left(\varkappa^g_{ros,ij} + \frac{1}{\theta c\tau^n} \right) F^{g,n}_{x,i+\frac{1}{2}j} = \frac{A_{ij}}{2\theta c\tau^n} F^{g,n-1}_{x,i+\frac{1}{2}j} + P^{g,n-1}_{R,ij},
\end{aligned}
\tag{2.79}
$$

22

where,

$$P_{R,ij}^{g,n-1} = \frac{\theta-1}{\theta}\left[c\Delta y_j\left(f_{xx,i+\frac{1}{2}j}^{g,n-1}E_{i+\frac{1}{2}j}^{g,n-1} - f_{xx,ij}^{g,n-1}E_{ij}^{g,n-1}\right)\right.$$
$$\left. + \frac{c\Delta x_i}{2}\left(f_{xy,ij+\frac{1}{2}}^{g,n-1}E_{ij+\frac{1}{2}}^{g,n-1} - f_{xy,ij-\frac{1}{2}}^{g,n-1}E_{ij-\frac{1}{2}}^{g,n-1}\right) + \frac{1}{2}A_{ij}\varkappa_{ros,ij}^{g,n-1}F_{x,i+\frac{1}{2}j}^{g,n-1}\right],$$

the top moment equation is,

$$c\Delta x_i\left(f_{yy,ij}^{g,n}E_{ij}^{g,n} - f_{yy,ij-\frac{1}{2}}^{g,n}E_{ij-\frac{1}{2}}^{g,n}\right) + \frac{c\Delta y_j}{2}\left(f_{xy,i+\frac{1}{2}j}^{g,n}E_{i+\frac{1}{2}j}^{g,n} - f_{xy,i-\frac{1}{2}j}^{g,n}E_{i-\frac{1}{2}j}^{g,n}\right)$$
$$+ \frac{1}{2}A_{ij}\left(\varkappa_{ros,ij}^g + \frac{1}{\theta c\tau^n}\right)F_{y,ij-\frac{1}{2}}^{g,n} = \frac{A_{ij}}{2\theta c\tau^n}F_{y,ij-\frac{1}{2}}^{g,n-1} + P_{B,ij}^{g,n-1}, \tag{2.80}$$

where,

$$P_{B,ij}^{g,n-1} = \frac{\theta-1}{\theta}\left[c\Delta x_i\left(f_{yy,ij}^{g,n-1}E_{ij}^{g,n-1} - f_{yy,ij-\frac{1}{2}}^{g,n-1}E_{i-\frac{1}{2}j}^{g,n-1}\right)\right.$$
$$\left. + \frac{c\Delta y_j}{2}\left(f_{xy,i+\frac{1}{2}j}^{g,n-1}E_{i+\frac{1}{2}j}^{g,n-1} - f_{xy,i-\frac{1}{2}j}^{g,n-1}E_{i-\frac{1}{2}j}^{g,n-1}\right) + \frac{1}{2}A_{ij}\varkappa_{ros,ij}^{g,n-1}F_{y,ij-\frac{1}{2}}^{g,n-1}\right],$$

and the bottom moment equation is,

$$c\Delta x_i\left(f_{yy,ij+\frac{1}{2}}^{g,n}E_{ij+\frac{1}{2}}^{g,n} - f_{yy,ij}^{g,n}E_{ij}^{g,n}\right) + \frac{c\Delta y_j}{2}\left(f_{xy,i+\frac{1}{2}j}^{g,n}E_{i+\frac{1}{2}j}^{g,n} - f_{xy,i-\frac{1}{2}j}^{g,n}E_{i-\frac{1}{2}j}^{g,n}\right)$$
$$+ \frac{1}{2}A_{ij}\left(\varkappa_{ros,ij}^g + \frac{1}{\theta c\tau^n}\right)F_{y,ij+\frac{1}{2}}^{g,n} = \frac{A_{ij}}{2\theta c\tau^n}F_{y,ij+\frac{1}{2}}^{g,n-1} + P_{T,ij}^{g,n-1}, \tag{2.81}$$

where,

$$P_{T,ij}^{g,n-1} = \frac{\theta-1}{\theta}\left[c\Delta x_i\left(f_{yy,ij+\frac{1}{2}}^{g,n-1}E_{ij+\frac{1}{2}}^{g,n-1} - f_{yy,ij}^{g,n-1}E_{ij}^{g,n-1}\right)\right.$$
$$\left. + \frac{c\Delta y_j}{2}\left(f_{xy,i+\frac{1}{2}j}^{g,n-1}E_{i+\frac{1}{2}j}^{g,n-1} - f_{xy,i-\frac{1}{2}j}^{g,n-1}E_{i-\frac{1}{2}j}^{g,n-1}\right) + \frac{1}{2}A_{ij}\varkappa_{ros,ij}^{g,n-1}F_{y,ij-\frac{1}{2}}^{g,n-1}\right].$$

To solve this system of equations, the radiatve flux is eliminated such that the primary unknowns are the cell-averaged and face-averaged energy densities. After the system of equations have been solved, the radiative fluxes are restored. The equations are solved with BiCGStab and an incomplete LU preconditioner [49].

2.4 Discretization of Grey Low-Order QD Equations and the Energy Balance Equation

The MLOQD equations are summed over all energies to form the spatial discretization scheme for the GLOQD equations that is algebraicly consistent with the spatial discretization of the MLOQD equations. There are a few methods to average the MLOQD equations over energy. The averaging of the zeroth moment equation is a straightforward procedure; all of the averaging functions are positive. The grey zeroth moment equation (2.82) is,

$$
\left(F_{x,i+\frac{1}{2}j}^{n} - F_{x,i-\frac{1}{2}j}^{n}\right)\Delta y_j + \left(F_{y,ij+\frac{1}{2}}^{n} - F_{y,ij-\frac{1}{2}}^{n}\right)\Delta x_i \\
+ \left(c\bar{\varkappa}_{E,ij}^{n} + \frac{1}{\theta\tau^n}\right)E_{ij}^{g,n}A_{ij} = \bar{Q}_{pl,ij}^{n}A_{ij} + \frac{A_{ij}}{\theta\tau^n}\tilde{E}_{ij}^{n-1} + \tilde{G}_{ij}^{n-1},
\tag{2.82}
$$

where the total cell-averaged energy density is,

$$
E_{ij}^{n} = \sum_{g=1}^{N_g} E_{g,ij}^{n},
\tag{2.83}
$$

the total face-averaged radiative flux in the x and y-direction is,

$$
F_{x,i\pm 1/2j}^{n} = \sum_{g=1}^{N_g} F_{g,x,i\pm 1/2j}^{n},
\tag{2.84}
$$

$$
F_{y,ij\pm 1/2}^{n} = \sum_{g=1}^{N_g} F_{g,y,ij\pm 1/2}^{n},
\tag{2.85}
$$

the cell-averaged grey opacity is,

$$
\bar{\varkappa}_{E,ij}^{n} = \frac{\sum_{g=1}^{N_g} \varkappa_{E,g,ij}^{n} E_{g,ij}^{n}}{\sum_{g=1}^{N_g} E_{g,ij}^{n}},
\tag{2.86}
$$

and the total cell-averaged Planckian source is,

$$
\bar{Q}_{pl,ij}^{n} = 4\sigma_R \bar{\varkappa}_{pl,ij}^{n} \left(T_{ij}^{n}\right)^4.
\tag{2.87}
$$

The terms from the previous time step are collapsed in energy such that,

$$\tilde{E}_{ij}^{n-1} = \sum_{g=1}^{N_g} E_{ij}^{g,n-1}, \tag{2.88}$$

$$\tilde{G}_{ij}^{n-1} = \sum_{g=1}^{N_g} G_{ij}^{g,n-1}. \tag{2.89}$$

The radiative flux can be negative or zero which is not desired for an averaging function. Averaging can be done such that the averaging function is always positive. This modified Rosseland opacity is defined as,

$$\tilde{\varkappa}_{ros,ij}^{g,n} = \varkappa_{ros,ij}^{g,n} + \frac{1}{\theta c \tau^n}. \tag{2.90}$$

which leads to the formulation of grey quantities that can be interpreted as effective diffusion coefficients. The discretized grey first moment equations are shown. The multigroup left and right first moment equations divided by the modified Rosseland opacity is,

$$\frac{c\Delta y_j}{\tilde{\varkappa}_{ros,ij}^{g,n}} \left(f_{xx,ij}^{g,n} E_{ij}^{g,n} - f_{xx,i-\frac{1}{2}j}^{g,n} E_{i-\frac{1}{2}j}^{g,n} \right) + \frac{c\Delta x_i}{2\tilde{\varkappa}_{ros,ij}^{g,n}} \left(f_{xy,ij+\frac{1}{2}}^{g,n} E_{ij+\frac{1}{2}}^{g,n} - f_{xy,ij-\frac{1}{2}}^{g,n} E_{ij-\frac{1}{2}}^{g,n} \right)$$
$$+ \frac{1}{2} A_{ij} F_{x,i-\frac{1}{2}j}^{g,n} = \frac{1}{\tilde{\varkappa}_{ros,ij}^{g,n}} \left[\frac{A_{ij}}{2\theta c \tau^n} F_{x,i-\frac{1}{2}j}^{g,n-1} + P_{L,ij}^{g,n-1} \right], \tag{2.91}$$

$$\frac{c\Delta y_j}{\tilde{\varkappa}_{ros,ij}^{g,n}} \left(f_{xx,i+\frac{1}{2}j}^{g,n} E_{i+\frac{1}{2}j}^{g,n} - f_{xx,ij}^{g,n} E_{ij}^{g,n} \right) + \frac{c\Delta x_i}{2\tilde{\varkappa}_{ros,ij}^{g,n}} \left(f_{xy,ij+\frac{1}{2}}^{g,n} E_{ij+\frac{1}{2}}^{g,n} - f_{xy,ij-\frac{1}{2}}^{g,n} E_{ij-\frac{1}{2}}^{g,n} \right)$$
$$+ \frac{1}{2} A_{ij} F_{x,i+\frac{1}{2}j}^{g,n} = \frac{1}{\tilde{\varkappa}_{ros,ij}^{g,n}} \left[\frac{A_{ij}}{2\theta c \tau^n} F_{x,i+\frac{1}{2}j}^{g,n-1} + P_{R,ij}^{g,n-1} \right], \tag{2.92}$$

where the grey coefficients H at the energy density are defined as,

$$H_{xx,ij}^{c,n} = \frac{\sum_{g=1}^{N_g} \frac{f_{xx,ij}^{g,n} E_{ij}^{g,n}}{\tilde{\varkappa}_{ros,ij}^{g,n}}}{\sum_{g=1}^{N_g} E_{ij}^{g,n}}, \tag{2.93}$$

$$H_{xx,ij}^{L/R,n} = \frac{\sum_{g=1}^{N_g} \frac{f_{xx,i\pm\frac{1}{2}j}^{g,n} E_{i\pm\frac{1}{2}j}^{g,n}}{\tilde{\varkappa}_{ros,ij}^{g,n}}}{\sum_{g=1}^{N_g} E_{i\pm\frac{1}{2}j}^{g,n}}, \tag{2.94}$$

25

$$H_{xy,ij}^{T/B,n} = \frac{\sum_{g=1}^{N_g} \frac{f_{xy,ij\pm\frac{1}{2}}^{g,n} E_{ij\pm\frac{1}{2}}^{g,n}}{\tilde{\varkappa}_{ros,ij}^{g,n}}}{\sum_{g=1}^{N_g} E_{ij\pm\frac{1}{2}}^{g,n}}. \tag{2.95}$$

This leads to the grey left moment equation,

$$c\Delta y_j \left(H_{xx,ij}^{c,n} E_{ij}^n - H_{xx,ij}^{L,n} E_{i-\frac{1}{2}j}^n \right)$$
$$+ \frac{c\Delta x_i}{2} \left(H_{xy,ij}^{T,n} E_{ij+\frac{1}{2}}^n - H_{xy,ij}^{B,n} E_{ij-\frac{1}{2}}^n \right) + \frac{1}{2} A_{ij} F_{x,i-\frac{1}{2}j}^n = \hat{P}_{L,ij}^{n-1}, \tag{2.96}$$

where,

$$\hat{P}_{L,ij}^{n-1} = \sum_{g=1}^{N_g} \frac{1}{\tilde{\varkappa}_{ros,ij}^{g,n}} \left(\frac{A_{ij}}{c\theta\tau^n} F_{x,i-\frac{1}{2}j}^{g,n-1} + P_{L,ij}^{g,n-1} \right), \tag{2.97}$$

and the grey right first moment equation,

$$c\Delta y_j \left(H_{xx,ij}^{R,n} E_{i+\frac{1}{2}j}^n - H_{xx,ij}^{c,n} E_{ij}^n \right)$$
$$+ \frac{c\Delta x_i}{2} \left(H_{xy,ij}^{T,n} E_{ij+\frac{1}{2}}^n - H_{xy,ij}^{B,n} E_{ij-\frac{1}{2}}^n \right) + \frac{1}{2} A_{ij} F_{x,i-\frac{1}{2}j}^n = \hat{P}_{R,ij}^{n-1}, \tag{2.98}$$

where,

$$\hat{P}_{R,ij}^{n-1} = \sum_{g=1}^{N_g} \frac{1}{\tilde{\varkappa}_{ros,ij}^{g,n}} \left(\frac{A_{ij}}{c\theta\tau^n} F_{x,i+\frac{1}{2}j}^{g,n-1} + P_{R,ij}^{g,n-1} \right). \tag{2.99}$$

The same is done for the multigroup top and bottom first moment equations such that,

$$\frac{c\Delta x_i}{\tilde{\varkappa}_{ros,ij}^{g,n}} \left(f_{yy,ij}^{g,n} E_{ij}^{g,n} - f_{yy,ij-\frac{1}{2}}^{g,n} E_{ij-\frac{1}{2}}^{g,n} \right) + \frac{c\Delta y_j}{2\tilde{\varkappa}_{ros,ij}^{g,n}} \left(f_{xy,i+\frac{1}{2}j}^{g,n} E_{i+\frac{1}{2}j}^{g,n} - f_{xy,i-\frac{1}{2}j}^{g,n} E_{i-\frac{1}{2}j}^{g,n} \right)$$
$$+ \frac{1}{2} A_{ij} F_{y,ij-\frac{1}{2}}^{g,n} = \frac{1}{\tilde{\varkappa}_{ros,ij}^{g,n}} \left[\frac{A_{ij}}{2\theta c\tau^n} F_{y,ij-\frac{1}{2}}^{g,n-1} + P_{B,ij}^{g,n-1} \right], \tag{2.100}$$

$$\frac{c\Delta x_i}{\tilde{\varkappa}_{ros,ij}^{g,n}} \left(f_{yy,ij+\frac{1}{2}}^{g,n} E_{ij+\frac{1}{2}}^{g,n} - f_{yy,ij}^{g,n} E_{ij}^{g,n} \right) + \frac{c\Delta y_j}{2\tilde{\varkappa}_{ros,ij}^{g,n}} \left(f_{xy,i+\frac{1}{2}j}^{g,n} E_{i+\frac{1}{2}j}^{g,n} - f_{xy,i-\frac{1}{2}j}^{g,n} E_{i-\frac{1}{2}j}^{g,n} \right)$$
$$+ \frac{1}{2} A_{ij} F_{y,ij+\frac{1}{2}}^{g,n} = \frac{1}{\tilde{\varkappa}_{ros,ij}^{g,n}} \left[\frac{A_{ij}}{2\theta c\tau^n} F_{y,ij+\frac{1}{2}}^{g,n-1} + P_{T,ij}^{g,n-1} \right], \tag{2.101}$$

where the grey coefficients H at the energy density are defined as,

$$H_{yy,ij}^{c,n} = \frac{\sum_{g=1}^{N_g} \frac{f_{yy,ij}^{g,n} E_{ij}^{g,n}}{\tilde{\varkappa}_{ros,ij}^{g,n}}}{\sum_{g=1}^{N_g} E_{ij}^{g,n}}, \tag{2.102}$$

26

$$H_{yy,ij}^{T/B,n} = \frac{\sum_{g=1}^{N_g} \frac{f_{yy,ij\pm\frac{1}{2}}^{g,n} E_{ij\pm\frac{1}{2}}^{g,n}}{\tilde{\varkappa}_{ros,ij}^{g,n}}}{\sum_{g=1}^{N_g} E_{ij\pm\frac{1}{2}}^{g,n}}, \tag{2.103}$$

$$H_{xy,ij}^{L/R,n} = \frac{\sum_{g=1}^{N_g} \frac{f_{xy,i\pm\frac{1}{2}j}^{g,n} E_{i\pm\frac{1}{2}j}^{g,n}}{\tilde{\varkappa}_{ros,ij}^{g,n}}}{\sum_{g=1}^{N_g} E_{i\pm\frac{1}{2}j}^{g,n}}, \tag{2.104}$$

This leads to the grey bottom first moment equation,

$$
c\Delta x_i \left(H_{yy,ij}^{c,n} E_{ij}^n - H_{yy,ij}^{B,n} E_{ij-\frac{1}{2}}^n \right) \\
+ \frac{c\Delta y_j}{2} \left(H_{xy,ij}^{R,n} E_{i+\frac{1}{2}j}^n - H_{xy,ij}^{L,n} E_{i-\frac{1}{2}j}^n \right) + \frac{1}{2} A_{ij} F_{x,ij-\frac{1}{2}}^n = \hat{P}_{B,ij}^{n-1}, \tag{2.105}
$$

where,

$$\hat{P}_{B,ij}^{n-1} = \sum_{g=1}^{N_g} \frac{1}{\tilde{\varkappa}_{ros,ij}^{g,n}} \left(\frac{A_{ij}}{c\theta\tau^n} F_{x,ij-\frac{1}{2}}^{g,n-1} + P_{B,ij}^{g,n-1} \right), \tag{2.106}$$

and the grey top first moment equation,

$$
c\Delta x_i \left(H_{yy,ij}^{T,n} E_{ij+\frac{1}{2}}^n - H_{yy,ij}^{c,n} E_{ij}^n \right) \\
+ \frac{c\Delta y_j}{2} \left(H_{xy,ij}^{R,n} E_{i+\frac{1}{2}j}^n - H_{xy,ij}^{L,n} E_{i-\frac{1}{2}j}^n \right) + \frac{1}{2} A_{ij} F_{x,ij+\frac{1}{2}}^n = \hat{P}_{T,ij}^{n-1}, \tag{2.107}
$$

where,

$$\hat{P}_{T,ij}^{n-1} = \sum_{g=1}^{N_g} \frac{1}{\tilde{\varkappa}_{ros,ij}^{g,n}} \left(\frac{A_{ij}}{c\theta\tau^n} F_{x,ij+\frac{1}{2}}^{g,n-1} + P_{T,ij}^{g,n-1} \right). \tag{2.108}$$

The discretized EB equation in space is,

$$\frac{d\epsilon_{ij}}{dt} = \sum_{g=1}^{N_g} \left(c\varkappa_{E,ij}^g E_{ij}^g - Q_{pl,ij}^g \right), \tag{2.109}$$

and it is discretized in time using the theta-weighted method which yields,

$$\frac{\epsilon_{ij}^n - \epsilon_{ij}^{n-1}}{\tau^n} = \theta \left(\sum_{g=1}^{N_g} \left(c\varkappa_{E,ij}^{g,n} E_{ij}^{g,n} - Q_{pl,ij}^{g,n} \right) \right) + (1-\theta) \left(\sum_{g=1}^{N_g} \left(c\varkappa_{E,ij}^{g,n-1} E_{ij}^{g,n-1} - Q_{pl,ij}^{g,n-1} \right) \right) \tag{2.110}$$

After summing over all groups, the EB equation is

$$\frac{1}{\theta\tau^n}\epsilon_{ij}^n + \bar{Q}_{pl,ij}^n - c\bar{\varkappa}_{E,ij}E_{ij}^n = \frac{1}{\theta\tau^n}\epsilon_{ij}^{n-1} + R_{ij}^{n-1}, \tag{2.111}$$

27

where,

$$R_{ij}^{n-1} = \frac{1-\theta}{\theta}\left(c\bar{\varkappa}_{E,ij}^{n-1}E_{ij}^{n-1} - \bar{Q}_{pl,ij}^{n-1}\right). \tag{2.112}$$

The unknowns in each cell are: 4 face-averaged energy densities, 1 cell-averaged energy density, 4 face-averaged radiative fluxes, and 1 cell-averaged material temperature.

2.5 Iteration Scheme for the Multi-Level QD Method

Algorithm 1 shows the general algorithm for solving the TRT problem using the QD method.

Algorithm 1: Iteration scheme for solving multi-level system of QD equations for TRT problem.

---

while $t^n < t^{end}$ **do**

    while$||\Delta T^{(s)}||>\epsilon_T||T^{(s)}||+\epsilon_T^*,||\Delta E^{(s)}||>\epsilon_E||E^{(s)}||+\epsilon_E^*$ **do**

        • Transport iteration: given $T^{(s)}$;

        $s = 0$: $T^{(0)} = T^{n-1}$, $f_{g,\beta\gamma}^{(1/2)} = f_{g,\beta\gamma}^{j-1}$;

        if $s > 0$ **then**

            Solve time-dependent multigroup RT eqs. for $I_g^{(s+1/2)}$;

            Compute group QD factors $f_{g,\beta\gamma}^{(s+1/2)}$;

        end

        while $||\Delta T^{(l,s)}|| > \tilde{\epsilon}_T||T^{(l,s)}|| + \tilde{\epsilon}_T^*$, $||\Delta E^{(l,s)}|| > \tilde{\epsilon}_E||E^{(l,s)}|| + \tilde{\epsilon}_E^*$ **do**

            • Multigroup low-order iteration: given $T^{(l,s)}$ and $f_{g,\beta\gamma}^{(s+1/2)}$;

            Solve MLOQD eqs. for $E_g^{(l+1,s)}$ and $\boldsymbol{F}_g^{(l+1,s)}$;

            Compute grey opacities $\bar{\varkappa}_E^{(l+1,s)}$, $\bar{\varkappa}_{ros}^{(l+1,s)}$ and factors $\bar{f}_{\beta\gamma}^{(l+1,s+1/2)}$;

            • Grey low-order iteration: solve GLOQD eqs. coupled with EB eq. for

              $E^{(l+1,s)}$, $\boldsymbol{F}^{(l+1,s)}$, and $T^{(l+1,s)}$

        end

        $T^{(s+1)} \leftarrow T^{(l+1,s)}$;

    end

    $T^n \leftarrow T^{(s+1)}$;

end

The first transport iteration can be skipped because the intensity from the previous time step is a good initial guess to evaluate the group QD factors on the new time level. The group opacities and Planckian source are evaluated at the given temperature and the MLOQD equations are solved to obtain the spectrum. Solving the MLOQD equations is referred to as a multigroup low-order iteration. The group coefficients are averaged with the spectrum and the algebraically consistent GLOQD equations are coupled to the EB equation. This nonlinear system

of equations is solved using Newton's method to obtain an update for the material temperature. This is referred to as a grey (Newton) iteration. Once the temperature has converged for the given spectrum, the group opacities and source are re-evaluated and this iteration process continues until the temperature and spectrum have converged for a given set of QD factors. This temperature is used to re-evaluate the group opacities and source for the transport problem. The RT equation is solved to update the angular distribution. This is referred to as a transport iteration. Once the transport iterations have converged, the temperature and intensity have been obtained for a given time step.

The estimation of temperature is obtained by solving the nonlinearly coupled EB (2.111) and GLOQD (2.96), (2.98), (2.105), (2.107) equations. These equations are linearized and solved by means of Newton's method. The unknowns are linearized such that,

$$
\begin{aligned}
T_{ij}^{(k+1)} &= T_{ij}^{(s)} + \Delta T_{ij}^{(k)}, \\
E_{ij}^{(k+1)} &= E_{ij}^{(s)} + \Delta E_{ij}^{(k)}, \\
\boldsymbol{F}_{ij}^{(k+1)} &= \boldsymbol{F}_{ij}^{(k)} + \Delta \boldsymbol{F}_{ij}^{(k)},
\end{aligned}
\tag{2.113}
$$

where k is the index of Newton iterations. A relationship between $\Delta T^{(s)}$ and $\Delta E^{(s)}$ is obtained from the linearized coupled GLOQD and EB equations. Linearization also requires the evaluation of derivatives of the grey opacities and Planckian sources,

$$
\begin{aligned}
Q_{pl,ij}^{n(s+1)} &= Q_{pl,ij}^{n(s)} + \frac{dQ_{pl,ij}}{dT}\Delta T_{ij}^{(s)}, \\
\bar{\varkappa}_{E,ij}^{n(s+1)} &= \bar{\varkappa}_{E,ij}^{n(s)} + \frac{d\bar{\varkappa}_{E,ij}}{dT}\Delta T_{ij}^{(s)}.
\end{aligned}
\tag{2.114}
$$

Both the group opacities and Planckian sources get re-evaluated after each temperature update. The Planckian source is a local function of material temperature, but the group opacities, $\varkappa_E^g$ averaged with the group energy densities obtained from the multigroup problem. This means the grey opacity depends on both the group coefficients and the spectrum. Accounting for the change in spectrum is important for finding a good estimate of temperature. For an approximate Newton method to work well, the derivative should be as accurate as possible. When only accounting for the change in temperature, the derivative was not correct when the spectrum is changing rapidly and sometimes would even have the wrong sign. A Frechet derivative is used to account for the changes due to both the local temperature and the spectrum [17]. $\frac{d\bar{\varkappa}_E}{dT}$ is fixed during Newton iterations and is updated using,

$$
\bar{\varkappa}_{E,ij}^{(k+1,l)} = \bar{\varkappa}_{E,ij}^{(k,l)} + \frac{d\bar{\varkappa}_{E,ij}^{(l)}}{dT}\Delta T_{ij}^{(k)},
\tag{2.115}
$$

29

where l is the index of multigroup iterations. The Frechet derivative is calculated using the grey opacity and temperature on successive multigroup iterations,

$$\frac{d\bar{\varkappa}_{E,ij}}{dT}^{(l)} = \frac{\bar{\varkappa}_{E,ij}^{(l)} - \bar{\varkappa}_{E,ij}^{(l-1)}}{T_{ij}^{(l)} - T_{ij}^{(l-1)}}. \tag{2.116}$$

The grey opacity on a multigroup iteration is defined as,

$$\bar{\varkappa}_{E,ij}^{(l)} = \frac{\sum_{g=1} \varkappa_{E,ij}^{g} \left(T_{ij}^{(l)} \right) E_{g,ij}^{(l)}}{\sum_{g=1} E_{g,ij}^{(l)}}. \tag{2.117}$$

Further details of this are describe in Chapter 5 where the iterations of the multilevel QD method are analyzed.

CHAPTER

3

TEMPORAL DISCRETIZATION METHODS FOR THE MULTI-LEVEL QD EQUATIONS

In this chapter, new multi-level QD (MLQD) methods based on the fully implicit time discretization of the RT equation are introduced. The modified subcell step (MSS) and the modified simple corner balance (MSCB) methods are formulated based on the backward Euler (B-E) time discretization of the RT equation. Three multi-level QD methods are established such that the RT equation is discretized in time using a first-order accurate scheme and the time discretization of the low-order QD equations vary based on the method. The first-order, hybrid, and monotonized hybrid schemes are formulated and analyzed. Numerical results show that the hybrid scheme gives better accuracy compared to the first-order temporal scheme. The monotonization hybrid scheme removes oscillatory behavior generated by the high resolution method. The convergence study shows that the hybrid method converges with the first order. Adaptive monotonization procedures are developed which improve the accuracy while reducing the computational expense. Analysis of the monotonization procedures applied to the P_1 equations is shown. This method is a commonly used approach for solving TRT problems. A part of the results presented in this chapter are published in [39].

3.1 Modified Discretization of the RT equation

In Chapter 2, the spatial discretization methods that are described were applied to Equation (2.44). The same is done for Equation (2.43) where the modified opacity is now defined as $\tilde{\varkappa} = \varkappa_E^n + \frac{1}{c\tau^n}$ and the modified source now has a term from the previous time step such that $S_A = \varkappa_{pl}^n B^n + \frac{1}{c\tau^n} I_m^{n-1}$. A new variant of the subcell step method and simple corner balance method for discretization of the time-dependent RT equation is developed to resolve this.

A desired feature of the discretization of the RT equation is that it reproduces the discrete steady state solution at equilibrium on a given spatial grid that corresponds to one of the spatial discretization scheme itself. In the SS method, the modified source is assumed to be constant in the cell. Since the temperature is constant in a cell, the Planckian source is constant for each subcell. The discretized RT equation has a cell-average intensity from the previous time step in the source term which is an area-weighted average of the subcell-averaged intensities. The modified source takes the form,

$$S_{A,p} = \varkappa_{pl}^n B^n + \frac{1}{c\tau^n} I_A^{n-1}, \tag{3.1}$$

where p is the subcell index and the group and angle indices are dropped for simplicity. Using the previous cell-averaged intensity in each subcell smears the time-dependent solution over a cell. As equilibrium is approached, the solution does not tend to the discrete steady state solution produced by this scheme. A modification of the SS method is developed to remove this effect which introduces the previous subcell-averaged intensity. This method is referred to as the modified subcell step (MSS) method. Equation (3.2) shows the effective source of the MSS method which now has a previous intensity with an index, p, for each subcell,

$$S_{A,p} = \varkappa_{pl}^n B^n + \frac{1}{c\tau^n} I_{A,p}^{n-1}. \tag{3.2}$$

The numerical solution obtained with this scheme tends to the discrete steady state solution on any given finite spatial grid as the TRT phenomenon approaches equilibrium.. The same modification is applied to the equations for the SCB method. The effective source in the corner balance equation, Equation (2.67), must be modified such that the previous intensity is the corner-averaged quantity rather than the cell-averaged quantity. This method is referred to as the Modified Simple Corner Balance (MSCB) method and the effective source is,

$$S_{A,c} = \varkappa_{pl}^n B^n + \frac{1}{c\tau^n} I_{A,c}^{n-1}, \tag{3.3}$$

where $I_{A,c}^{n-1}$ is the corner-averaged intensity from the previous time step. This will lead to an increase in storage by a factor of 4 because there are 4 corners per cell.

32

3.2 Formulation of First-Order and Hybrid Temporal Discretization of the Multi-Level System of QD Equations

One benefit of the multi-level QD method is the capability to independently discretize the RT equation and the LOQD equations. This allows for a broad range of discretization combinations that can potentially improve the accuracy or efficiency of the method. The spatially and angularly discretized RT equation (2.1) has the following general form:

$$\frac{1}{c}\frac{dI_g}{dt} = H\left[I_g, T\right],\tag{3.4}$$

Equation (3.4) is discretized in time using the B-E scheme which gives,

$$I_g^n - I_g^{n-1} = c\tau_n H^n[I_g^n, T^n].\tag{3.5}$$

This scheme is robust with first-order accuracy. A high-order time discretization of the RT equation gives better accuracy, but would add more complexity. High-order schemes require storage of more previous time step data which is rather expensive due to the high dimensionality of the RT equation. The idea is to develop a mixed-order scheme and take advantage of a high-order discretization of LOQD equations. A class of methods are introduced such that the RT equation is discretized with B-E while the discretization of the low-order equations is varied. The time-dependent RT equation is discretized in space using the MSS and MSCB method.

3.2.1 Formulation of First-Order Scheme

To introduce the new MLQD methods, the spatially discretized MLOQD equations (2.8) and (2.9) are presented in operator form,

$$\frac{dE_g}{dt} = L_{0,g}[E_g, \mathbf{F}_g, T],\tag{3.6}$$

$$\frac{1}{c}\frac{d\mathbf{F}_g}{dt} = \boldsymbol{L}_{1,g}[E_g, \mathbf{F}_g, T],\tag{3.7}$$

and the spatially discretized GLOQD and EB equations (2.22-2.26) are presented in operator form as well,

$$\frac{dE}{dt} = L_0[E, \mathbf{F}, T],\tag{3.8}$$

$$\frac{1}{c}\frac{d\mathbf{F}}{dt} = \boldsymbol{L}_1[E, \mathbf{F}, T],\tag{3.9}$$

33

$$\frac{d\varepsilon}{dt} = M[E, T]. \tag{3.10}$$

The first-order scheme consists of the B-E time discretization for the RT equation, LOQD equations, and the EB equation. The MLOQD equations are discretized in space with the finite-volume method which is second-order accurate presented in Chapter 2. The complete system of discretized equations for the first-order scheme consists of the RT equation,

$$I_g^n - I_g^{n-1} = c\tau_n H^n, \tag{3.11}$$

fully discretized MLOQD equations,

$$E_g^n - E_g^{n-1} = \tau^n L_{0,g}^n, \tag{3.12}$$

$$\mathbf{F}_g^n - \mathbf{F}_g^{n-1} = c\tau^n \boldsymbol{L}_{1,g}^n, \tag{3.13}$$

and the fully discretized GLOQD and EB equations,

$$E^n - E^{n-1} = \tau^n L_0^n, \tag{3.14}$$

$$\boldsymbol{F}^n - \boldsymbol{F}^{n-1} = c\tau^n \boldsymbol{L}_1^n, \tag{3.15}$$

$$\varepsilon^n - \varepsilon^{n-1} = \tau^n M^n. \tag{3.16}$$

3.2.2 Formulation of Hybrid Scheme

While high resolution schemes come with complexity and increased storage, the reduced dimensionality of the low-order equations mitigate these issues. Referring to Equations (2.76-2.81), the terms from the previous time step can be lumped into a single term that is required for each spatial cell in each group. This is negligible compared to storing the transport solution which would require the same, but for each direction as well. The class of subcell spatial discretization schemes would require even more storage. The hybrid scheme consists of B-E time discretization of the RT equation and Crank-Nicolson (C-N) time discretization for the MLOQD and EB equations. The term hybrid is used to reflect the combination of a first-order and second-order accurate scheme. The complete system of discretized equations for the hybrid scheme consists of the RT equation,

$$I_g^n - I_g^{n-1} = c\tau_n H^n, \tag{3.17}$$

fully discretized MLOQD equations,

$$E_g^n - E_g^{n-1} = \frac{\tau^n}{2}\left(L_{0,g}^n + L_{0,g}^{n-1}\right), \tag{3.18}$$

$$\mathbf{F}_g^n - \mathbf{F}_g^{n-1} = \frac{c\tau^n}{2}\left(\boldsymbol{L}_{1,g}^n + \boldsymbol{L}_{1,g}^{n-1}\right), \tag{3.19}$$

and the fully discretized GLOQD and EB equations,

$$E^n - E^{n-1} = \frac{\tau^n}{2}\left(L_0^n + L_0^{n-1}\right), \tag{3.20}$$

$$\mathbf{F}^n - \mathbf{F}^{n-1} = \frac{c\tau^n}{2}\left(\boldsymbol{L}_1^n + \boldsymbol{L}_1^{n-1}\right), \tag{3.21}$$

$$\varepsilon^n - \varepsilon^{n-1} = \frac{\tau^n}{2}(M^n + M^{n-1}). \tag{3.22}$$

The expected benefits are that it will have better accuracy. The low-order problem is discretized with a second-order accurate scheme, but in the limit, quadratic convergence in time is not expected. It should converge linearly because the method is restricted by the QD factors generated by the solution of the RT equation which is discretized with B-E. Nonetheless, any increase in the rate of convergence is beneficial. This coupled with the minimal extra storage should provide a better method with little cost.

3.3 Monotonization of Second-Order Temporal Scheme for the Low-Order QD Equations

Because the hybrid method involves applying a high-order discretization scheme to hyperbolic equations, monotonization is needed to suppress numerical oscillations. A third multi-level QD method is developed by applying the L-TRAP scheme to the MLOQD equations and is referred to as the monotonized hybrid method.

The L-TRAP scheme [50] is used as a monotonization procedure when using the second-order method. This scheme was developed for hyperbolic conservation laws and it is applied to the MLOQD equations. The L-TRAP scheme is shown to significantly reduce the oscillatory behavior of the solution, which is especially notable in the high energy groups. The θ-weighted temporal discretization is applied to the MLOQD equations (3.6) and (3.7) which gives,

$$E_g^n - E_g^{n-1} = \tau^n\left(\theta L_{0,g}^n + (1-\theta)L_{0,g}^{n-1}\right), \tag{3.23}$$

$$\mathbf{F}_g^n - \mathbf{F}_g^{n-1} = c\tau^n\left(\theta\boldsymbol{L}_{1,g}^n + (1-\theta)\boldsymbol{L}_{1,g}^{n-1}\right). \tag{3.24}$$

A feature of the θ-weighted method is the order of accuracy can vary by changing a parameter, θ. When $\theta = 1$, this scheme is equivalent to the B-E method which is first-order accurate in time. When $\theta = \frac{1}{2}$, it becomes the C-N method which is second-order accurate. The L-TRAP method restricts θ such that a local monotonicity condition is not violated [50]. It is based off a lemma by Hyunh [51] that states: given $f(x_1)$, $f(x_2)$ and $f'(x_1)$, $f'(x_2)$ at x_1 and x_2, the resulting *quadratic interpolant* is monotone in $[x_1, x_2]$ if,

$$f'(x_1), f'(x_2) \in [0, 2s], \tag{3.25}$$

where,

$$s = \frac{f(x_2) - f(x_1)}{x_2 - x_1}. \tag{3.26}$$

The finite difference approximation of the derivative can be estimated by using the solution to the equations using a first-order scheme. This extra step of calculation is analogous to a predictor step which approximates the expected sign and value of the derivative and operator. The derivatives and operators for the local monotonicty condition are defined as

$$s_0^{g,n+\frac{1}{2}} = \frac{E_g^{n+\frac{1}{2}} - E_g^n}{\tau^n}, \tag{3.27}$$

$$s_\alpha^{g,n+\frac{1}{2}} = \frac{1}{c} \frac{F_{g,\alpha}^{n+\frac{1}{2}} - F_{g,\alpha}^n}{\tau^n}, \tag{3.28}$$

and

$$E_g^{n+\frac{1}{2}} = E_g^n + \tau^n L_{0,g}^{n+\frac{1}{2}}, \tag{3.29}$$

$$F_{g,\alpha}^{n+\frac{1}{2}} = F_{g,\alpha}^n + \tau^n L_{1,g,\alpha}^{n+\frac{1}{2}}, \tag{3.30}$$

where $n + \frac{1}{2}$ is the intermediate level of the predictor step, $F_{g,\alpha}^n = \boldsymbol{F}_g^n \cdot \boldsymbol{n}_\alpha$, $\boldsymbol{n}_\alpha$ is the face normal, and $\alpha = $ L,R,T,B is the index of the cell face. A parameter, r_{ij}, is defined for each cell in the domain with $\theta_{ij} = 1.0 - 0.5 r_{ij}$. This monotonization scheme checks whether $L_{0,g}^n$, $L_{0,g}^{n+\frac{1}{2}}$ and $\boldsymbol{L}_{1,g}^n$, $\boldsymbol{L}_{1,g}^{n+\frac{1}{2}}$ are contained on the intervals $\left[0, 2s_{0,g}^{n+\frac{1}{2}}\right]$ and $\left[0, 2s_{1,g,\alpha}^{n+\frac{1}{2}}\right]$, respectively. If these conditions are met, the interpolant is monotonic and r_{ij} is set to 1. If one or both quantities are of opposite sign, they can be non-monotonic and therefore r_{ij} is set to 0 which reverts to a first-order scheme. If neither condition is met, this is a case where the derivative has the same sign but is too large. The minimum r_{ij} that preserves monotonicity is selected. The L-TRAP scheme is shown in Algorithm 2,

---

Algorithm 2: Monotonization procedure for L-TRAP scheme.

---

if $L_p^{n+\frac{1}{2}}(L_p^{n+\frac{1}{2}} - 2s_p^{n+\frac{1}{2}}) \leq \epsilon_H$ and $L_p^n\left(L_p^n - 2s_p^n\right) \leq \epsilon_H$ **then**
| $r_{ij} = 1$
else if $L_p^{n+\frac{1}{2}} \leq -\tilde{\epsilon}_H(s_p^{n+\frac{1}{2}} + \epsilon_H)$ or $L_p^n \leq -\tilde{\epsilon}_H(s_p^n + \epsilon_H)$ **then**
| $r_{ij} = 0$
else

$$r_{ij} = \min\left[\frac{2s_p^{n+\frac{1}{2}}}{L_p^n + \epsilon_H}, \frac{2s_p^{n+\frac{1}{2}}}{L_p^{n+\frac{1}{2}} + \epsilon_H}, 1\right]$$

---

where ϵ_H and $\tilde{\epsilon}_H$ are a small value that prevents breaking the condition due to small changes in the solution. The full system of discretized equations for the monotonized hybrid scheme consists of the RT equation,

$$I_g^n - I_g^{n-1} = c\tau_n H^n, \tag{3.31}$$

fully discretized MLOQD equations,

$$E_g^n - E_g^{n-1} = \tau^n\left(\theta_g L_{0,g}^n + (1-\theta_g)L_{0,g}^{n-1}\right), \tag{3.32}$$

$$\mathbf{F}_g^n - \mathbf{F}_g^{n-1} = c\tau^n\left(\theta_g \boldsymbol{L}_{1,g}^n + (1-\theta_g)\boldsymbol{L}_{1,g}^{n-1}\right). \tag{3.33}$$

and the fully discretized GLOQD and EB equations,

$$E^n - E^{n-1} = \tau^n\left(\bar{\theta}_E L_0^n + (1-\bar{\theta}_E)L_0^{n-1}\right), \tag{3.34}$$

$$\mathbf{F}^n - \mathbf{F}^{n-1} = c\tau^n\left(\bar{\theta}_F \boldsymbol{L}_1^n + (1-\bar{\theta}_F)\boldsymbol{L}_1^{n-1}\right), \tag{3.35}$$

$$\varepsilon^n - \varepsilon^{n-1} = \tau^n(\bar{\theta}_\varepsilon M^n + (1-\bar{\theta}_\varepsilon)M^{n-1}), \tag{3.36}$$

where $\theta_g = \theta_g[E_g, \mathbf{F}_g, T]$, $\theta_g \in [0.5, 1]$ and $\bar{\theta}_E, \bar{\theta}_F, \bar{\theta}_\varepsilon$ are averaged such that the GLOQD and EB equations are algebraicly consistent with the MLOQD equations. θ_g is spatially and group dependent and no longer a constant value. Since the monotonization procedure adds a stage for evaluating $E_g^{n+\frac{1}{2}}$ and $F_{g,\alpha}^{n+\frac{1}{2}}$ and the weights depend on the solution, the temporal scheme is nonlinear. However, the multilevel QD method is a nonlinear one originally. In Chapter 5, the effects of the nonlinear monotonization algorithm on iterations for solving the multilevel system of equations are studied.

37

3.4 Numerical Results for Multi-Level QD Methods

In this section, results and analysis are presented for the first-order, hybrid, and monotonized hybrid schemes. This is done for the MSS and MSCB methods for spatial discretization of the RT equation. The accuracy, convergence, and shape of the temperature and radiation wave are analyzed. The computational results are of Fleck-Cummings test problem [6]. Adaptive monotonization procedures are analyzed in order to reduce the work of the monotonization procedure when applicable. This monotonization scheme is also applied to the multilevel method for TRT problems based P_1 equations. In this case, the photon transport is modeled with the P_1 approximation. Thus, the group low-order equations are the group P_1 equations. The RT equation is not involved. This is rather common way of solving TRT problems. It is a part of the family of methods based on the method of spherical harmonics.

Fleck & Cummings Test Problem

Figure 3.1 depicts a 2D version of Fleck and Cummings test problem [6]. It consists of a 4 cm x 4 cm square that is heated by a 1 keV blackbody source at the left boundary while the other boundaries are vacuum. The initial temperature in the domain is $kT_0 = 10^{-3}$ keV. The initial distribution of radiation is $I_\nu|_{t=0} = B_\nu(T_0)$. There is one material with the spectral opacity defined as $\varkappa_\nu = \frac{27}{\nu^3}(1 - e^{-\frac{\nu}{T}})$. The material energy density is a linear function of temperature $\varepsilon(T) = c_v T$ with $c_v = a T_b^3$. This test is solved with a time step of $\tau = 2 \times 10^{-3}$ shakes (1 shake $= 10^{-8}$ sec) up to ct = 90 cm. Results are shown for a 10x10 and 20x20 spatial meshes. 17 groups and a quadruple-range quadrature with 36 angles/octant are used [52]. The group structure is shown in Table 3.1. The parameters of convergence criteria for transport iterations are $\epsilon_T = \epsilon_E = 10^{-7}$.

Table 3.1 Boundaries of energy intervals [keV] defining the 17-group structure for 2D version of Fleck and Cummings TRT test problem.

g	1	2	3	4	5	6	7	8	9
ν_g [keV]	0.0×10^0	3.0×10^{-1}	6.0×10^{-1}	8.0×10^{-1}	1.2×10^0	1.5×10^0	1.8×10^0	2.4×10^0	2.7×10^0

g	10	11	12	13	14	15	16	17	18
ν_g [keV]	3.0×10^0	4.0×10^0	5.0×10^0	7.0×10^0	9.0×10^0	1.1×10^1	1.5×10^1	2.0×10^1	1.0×10^5
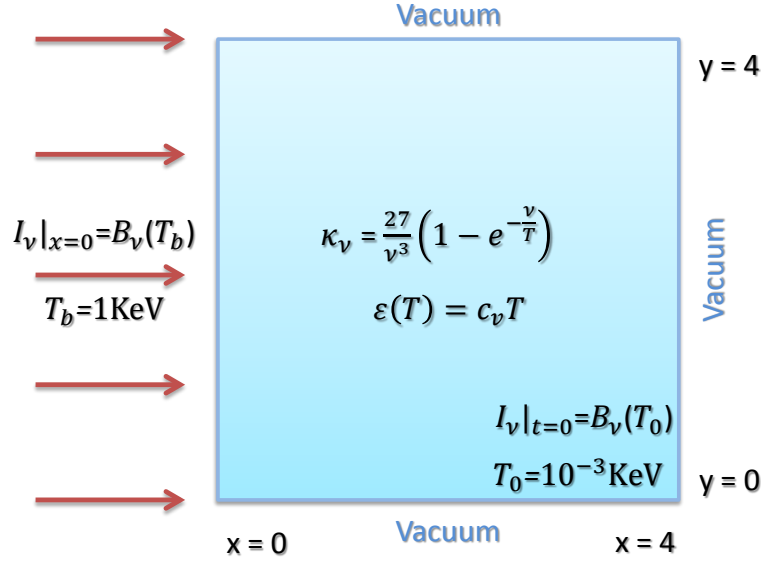
Figure 3.1 2D version of Fleck and Cummings TRT test problem.

3.4.1 Modified Subcell Step (MSS) Method

In this section, numerical results of the multi-level QD method with MSS transport scheme and different temporal discretization of the LOQD equations are presented. The solution of this test problem is presented at the three characteristic stages of wave development. The first instant (ct=6 cm) is the initial stage of forming the wave where the change rate of the intensity is large at the boundary with incoming radiation. The second instant (ct=15 cm) is the developed stage of the wave propagation at which the wave has a well-formed shape. The third one (ct=90 cm) is the final stage when the wave reached the opposite side of the domain that is now significantly warmed up and is close to equilibrium. Figures 3.2 and 3.4 compare the solution of the first-order scheme with that of the hybrid scheme on a 10x10 mesh. Figures 3.3 and 3.5 show the same comparison with the cell-averaged values of temperature and total energy density in each cell on a 10x10 mesh. There are no oscillations in the material temperature or energy density, but at $ct = 6$ cm, the energy density has a change in the sign of the second derivative after the wave front. This is caused by non-monotonicity of the energy density in some groups. The other two stages do not exhibit this behavior.

(a) $ct = 6$ cm **(b)** $ct = 15$ cm **(c)** $ct = 90$ cm

Figure 3.2 Temperature (in keV) computed by the multi-level QD method using the MSS transport scheme with $\tau=2\times10^{-3}$sh using (i) the first order method (top-half) and (ii) the hybrid method (bottom-half) on a 10x10 mesh.

(a) $ct = 6$ cm **(b)** $ct = 15$ cm **(c)** $ct = 90$ cm

Figure 3.3 Cell-averaged values of temperature (in keV) computed by the multi-level QD method using the MSS transport scheme with $\tau=2\times10^{-3}$sh using (i) the first order method (top-half) and (ii) the hybrid method (bottom-half) on a 10x10 mesh.

(a) $ct = 6$ cm **(b)** $ct = 15$ cm **(c)** $ct = 90$ cm

Figure 3.4 Total energy density ($E\times10^{-13}\frac{erg}{cm^3}$) computed by the multi-level QD method using the MSS transport scheme with $\tau=2\times10^{-3}$sh using (i) the first order method (top-half) and (ii) the hybrid method (bottom-half) on a 10x10 mesh.

40

(a) $ct = 6$ cm **(b)** $ct = 15$ cm **(c)** $ct = 90$ cm
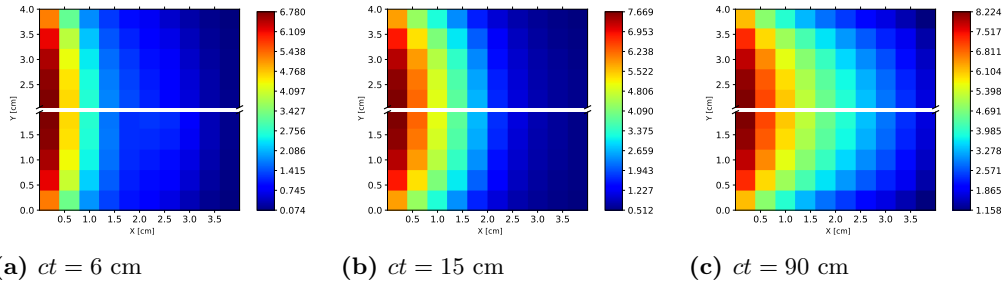
Figure 3.5 Cell-averaged values of the total energy density ($E \times 10^{-13} \frac{erg}{cm^3}$) computed by the multi-level QD method using the MSS transport scheme with $\tau = 2 \times 10^{-3}$sh using (i) the first order method (top-half) and (ii) the hybrid method (bottom-half) on a 10x10 mesh.

Figures 3.6 and 3.8 compare the solution of the first-order scheme with that of the hybrid scheme on a 20x20 mesh. Figures 3.7 and 3.9 show the comparison of cell-averaged values of temperature and total energy density in each cell on the 20x20 mesh. The radiation wave at $ct = 6$ cm computed with the hybrid scheme has a similar effect to what is seen on the 10x10 mesh where the shape is noticeably different compared to the first order scheme. The behavior of the solution for each method on the refined mesh is not significantly different from what is seen on the 10x10 mesh. The optical thickness drives the problem. For any given mesh, some energy groups will have a large optical thickness and concurrently others will have an extremely small optical thickness. Because of this, there is not a perfect mesh for this type of problem and a significant change in the behavior of the solution is not expected.

(a) $ct = 6$ cm **(b)** $ct = 15$ cm **(c)** $ct = 90$ cm
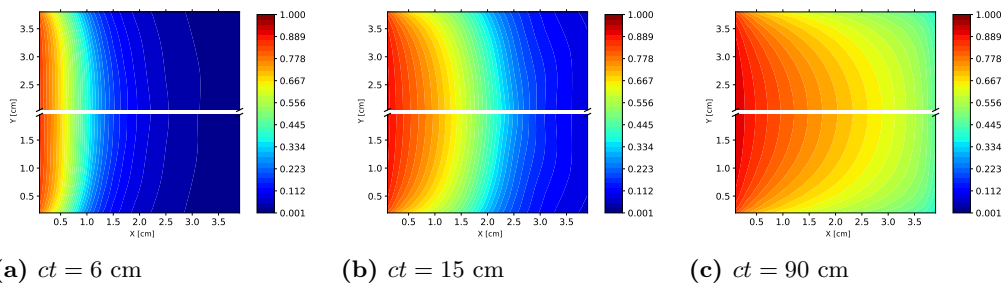
Figure 3.6 Temperature (in keV) computed by the multi-level QD method using the MSS transport scheme with $\tau = 2 \times 10^{-3}$sh using (i) the first order method (top-half) and (ii) the hybrid method (bottom-half) on a 20x20 mesh.

41

(a) $ct = 6$ cm **(b)** $ct = 15$ cm **(c)** $ct = 90$ cm
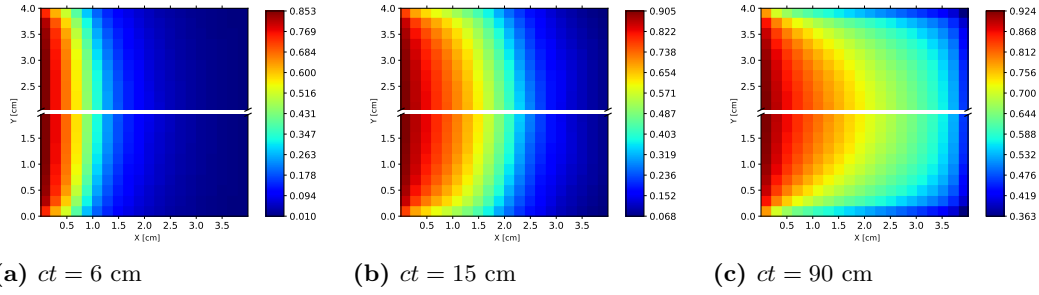
Figure 3.7 Cell-averaged values of temperature (in keV) computed by the multi-level QD method using the MSS transport scheme with $\tau = 2 \times 10^{-3}$sh using (i) the first order method (top-half) and (ii) the hybrid method (bottom-half) on a 20x20 mesh.

(a) $ct = 6$ cm **(b)** $ct = 15$ cm **(c)** $ct = 90$ cm
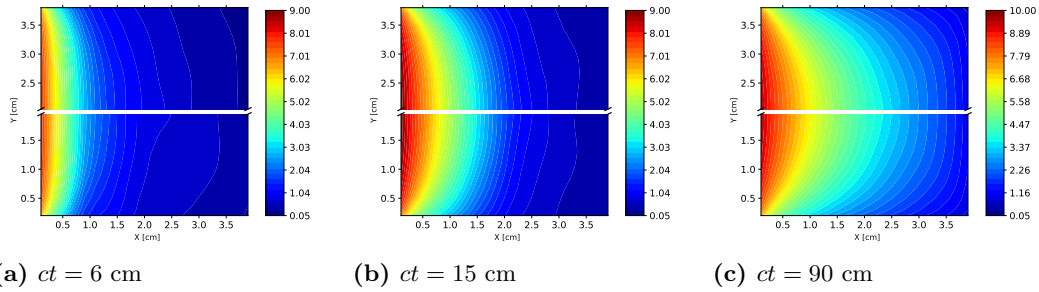
Figure 3.8 Total energy density ($E \times 10^{-13} \frac{erg}{cm^3}$) computed by the multi-level QD method using the MSS transport scheme with $\tau = 2 \times 10^{-3}$sh using (i) the first order method (top-half) and (ii) the hybrid method (bottom-half) on a 20x20 mesh.

(a) $ct = 6$ cm **(b)** $ct = 15$ cm **(c)** $ct = 90$ cm
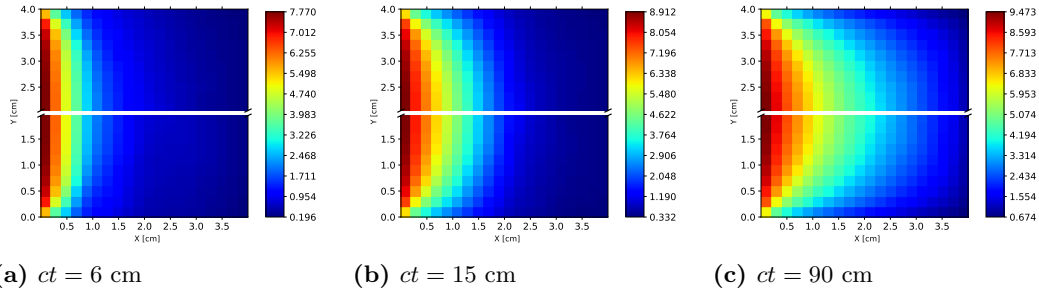
Figure 3.9 Cell-averaged values of the total energy density ($E \times 10^{-13} \frac{erg}{cm^3}$) computed by the multi-level QD method using the MSS transport scheme with $\tau = 2 \times 10^{-3}$sh using (i) the first order method (top-half) and (ii) the hybrid method (bottom-half) on a 20x20 mesh.

42

Figures 3.10 and 3.11 show the relative difference between these two methods on a 10x10 mesh. The largest difference is at the right boundary which is where the unphysical behavior occurs. Note that this is before the wave front therefore the non-local radiation is not prominent in this sub-domain. Figures 3.12 and 3.13 show the relative difference between the solution obtained these two methods on a 20x20 mesh. The maps show that the largest differences are near the right boundary.

(a) $ct = 6$ cm   (b) $ct = 15$ cm   (c) $ct = 90$ cm
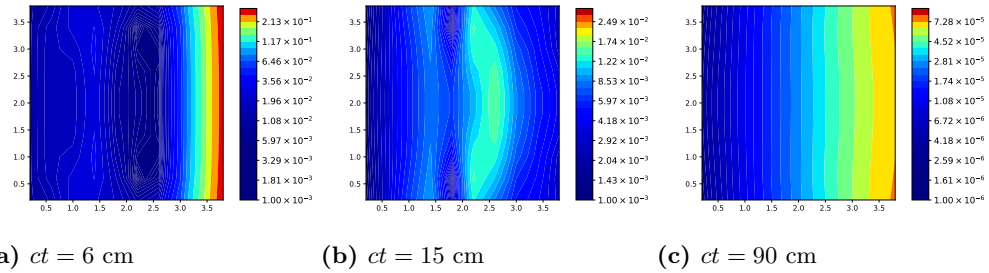
Figure 3.10 Relative difference in temperature computed by the multi-level QD method using the MSS transport scheme with $\tau=2\times10^{-3}$sh using (i) the first order method (top-half) and (ii) the hybrid method (bottom-half) on a 10x10 mesh.

(a) $ct = 6$ cm   (b) $ct = 15$ cm   (c) $ct = 90$ cm
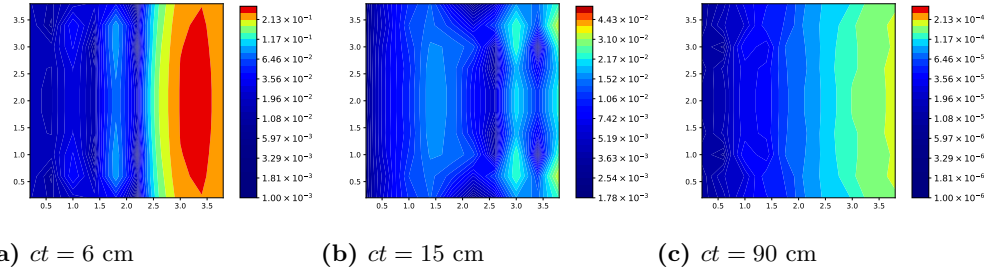
Figure 3.11 Relative difference in total energy density ($E\times10^{-13}\frac{erg}{cm^3}$) computed by the multi-level QD method using the MSS transport scheme with $\tau=2\times10^{-3}$sh using (i) the first order method (top-half) and (ii) the hybrid method (bottom-half) on a 10x10 mesh.

43

(a) $ct = 6$ cm   **(b)** $ct = 15$ cm   **(c)** $ct = 90$ cm
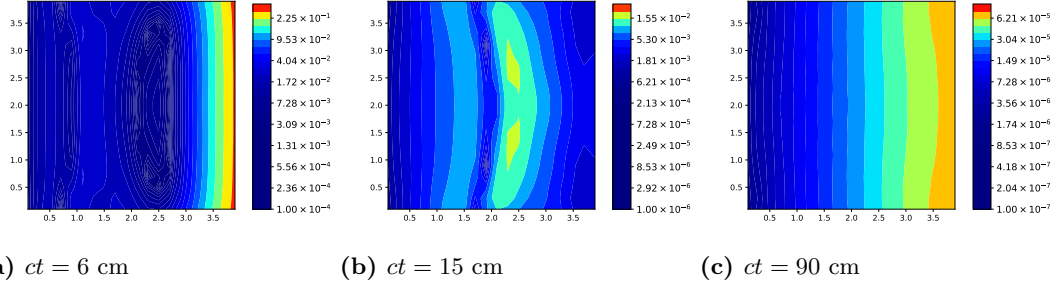
Figure 3.12 Relative difference in temperature computed by the multi-level QD method using the MSS transport scheme with $\tau=2\times10^{-3}$sh using (i) the first order method (top-half) and (ii) the hybrid method (bottom-half) on 20x20 mesh.

(a) $ct = 6$ cm   **(b)** $ct = 15$ cm   **(c)** $ct = 90$ cm
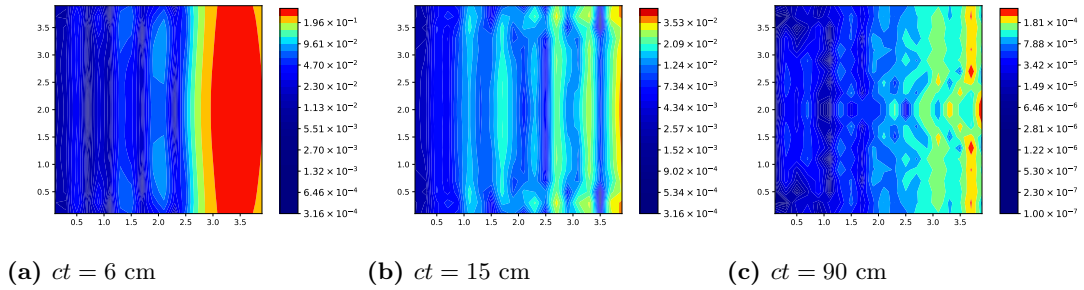
Figure 3.13 Relative difference in total energy density $(E\times10^{-13}\frac{erg}{cm^3})$ computed by the multi-level QD method using the MSS transport scheme with $\tau=2\times10^{-3}$sh using (i) the first order method (top-half) and (ii) the hybrid method (bottom-half) on 20x20 mesh.

Figures 3.14 and 3.15 compare the solution of the monotonized hybrid scheme with that of the hybrid scheme on a 10x10 mesh. The monotonized hybrid scheme generates a solution without oscillations. The radiation wave resembles that of the first-order scheme which is expected because the L-TRAP method switches to a first-order method locally when the monotonicity condition is not satisfied in a cell. Figures 3.16 and 3.17 show that the maximum difference is at the right boundary once again. Figures 3.18 and 3.19 compare the solution of the monotonized hybrid and hybrid scheme on a 20x20 mesh. The monotonized hybrid scheme does well in removing the oscillatory behavior that causes the effect seen in the radiative wave at $ct = 6$ cm. Like the 10x10 mesh, the solution at the other stages of evolution have no visible differences on this scale.

44

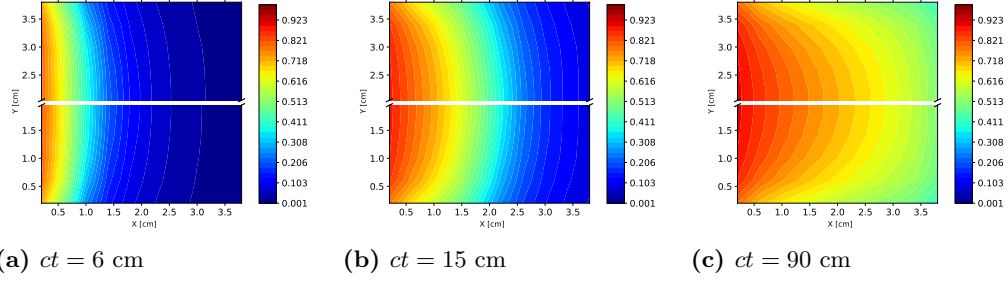**(a)** $ct = 6$ cm **(b)** $ct = 15$ cm **(c)** $ct = 90$ cm
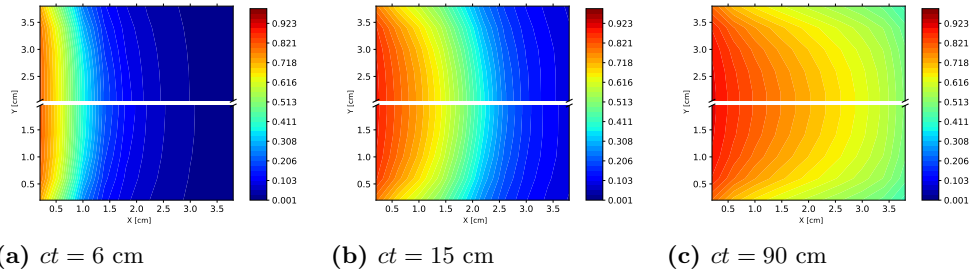
Figure 3.14 Temperature (in keV) computed by the multi-level QD method with using the MSS transport scheme $\tau=2\times10^{-3}$sh using (i) the monotonized hybrid method (top-half) and (ii) the hybrid method (bottom-half) on a 10x10 mesh.

(a) $ct = 6$ cm **(b)** $ct = 15$ cm **(c)** $ct = 90$ cm
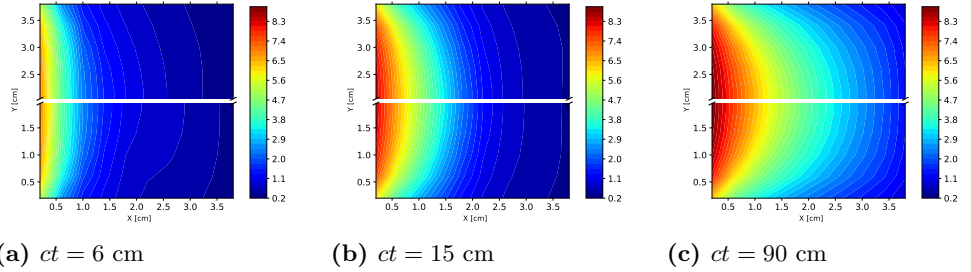
Figure 3.15 Total energy density ($E\times10^{-13}\frac{erg}{cm^3}$) computed by the multi-level QD method using the MSS transport scheme with $\tau=2\times10^{-3}$sh using (i) the monotonized hybrid method (top-half) and (ii) the hybrid method (bottom-half) on a 10x10 mesh.
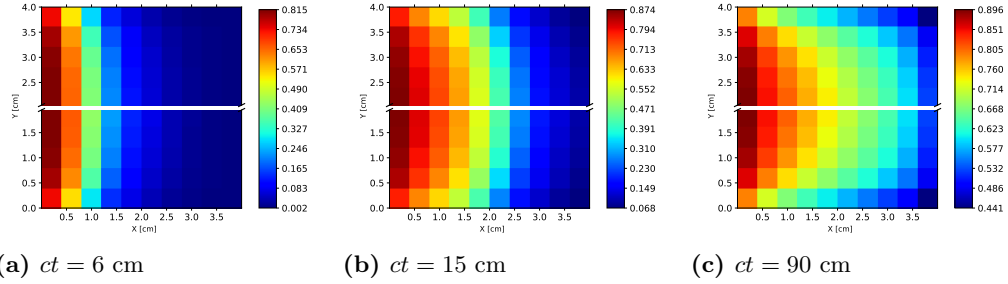

(a) $ct = 6$ cm **(b)** $ct = 15$ cm **(c)** $ct = 90$ cm
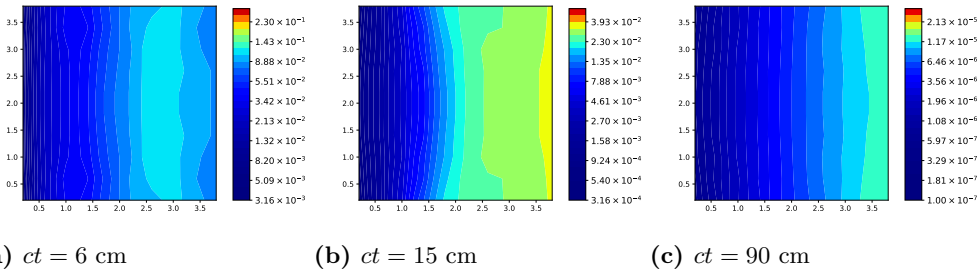
Figure 3.16 Relative difference in temperature computed by the multi-level QD method using the MSS transport scheme with $\tau=2\times10^{-3}$sh using (i) the monotonized hybrid method (top-half) and (ii) the hybrid method (bottom-half) on a 10x10 mesh.

45

(a) $ct = 6$ cm   **(b)** $ct = 15$ cm   **(c)** $ct = 90$ cm
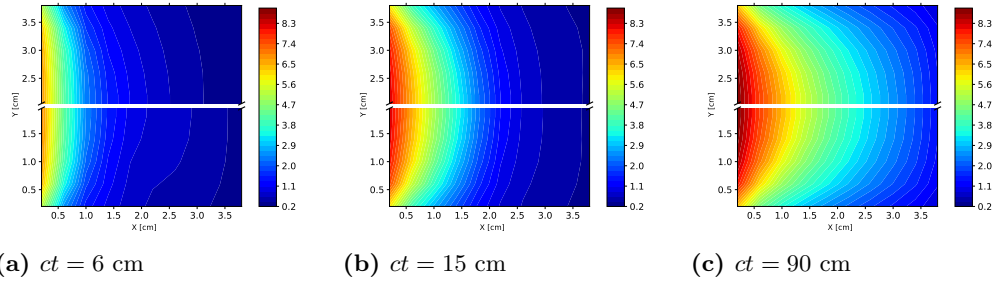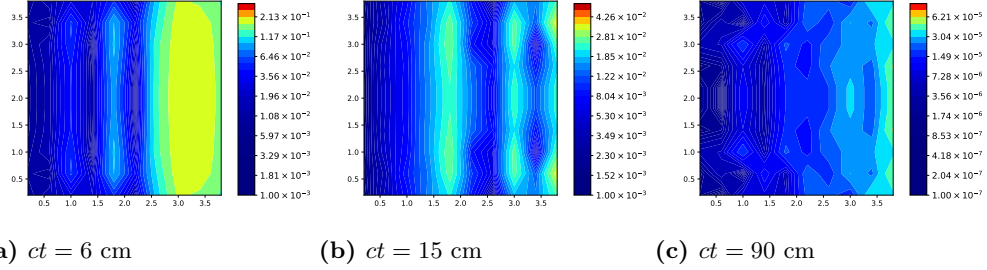
Figure 3.17 Relative difference in total energy density ($E \times 10^{-13} \frac{erg}{cm^3}$) computed by the multi-level QD method using the MSS transport scheme with $\tau = 2 \times 10^{-3}$sh using (i) the monotonized hybrid method (top-half) and (ii) the hybrid method (bottom-half) on a 10x10 mesh.


(a) $ct = 6$ cm   **(b)** $ct = 15$ cm   **(c)** $ct = 90$ cm
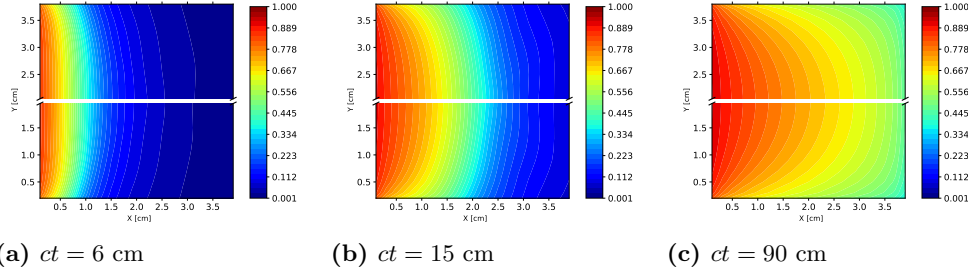
Figure 3.18 Temperature (in keV) computed by the multi-level QD method with using the MSS transport scheme $\tau = 2 \times 10^{-3}$sh using (i) the monotonized hybrid method (top-half) and (ii) the hybrid method (bottom-half) on a 20x20 mesh.

(a) $ct = 6$ cm   **(b)** $ct = 15$ cm   **(c)** $ct = 90$ cm
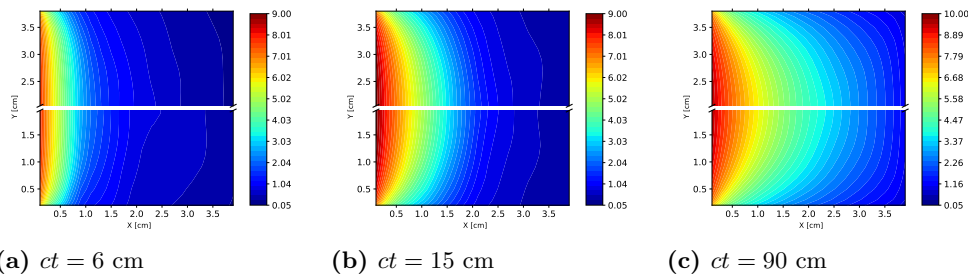
Figure 3.19 Total energy density ($E \times 10^{-13} \frac{erg}{cm^3}$) computed by the multi-level QD method using the MSS transport scheme with $\tau = 2 \times 10^{-3}$sh using (i) the monotonized hybrid method (top-half) and (ii) the hybrid method (bottom-half) on a 20x20 mesh.

46

The monotonization procedure is done in each group. The material temperature and total energy density encompass the physics averaged over frequency; therefore, these results show an accumulative effect of monotonization. To distinguish how the method performs in different regimes, the group energy density E_g is analyzed. Figure 3.20 shows the radiation energy density in group 1 (0 keV $\leq \nu \leq$ 0.3 keV) for each method at $ct = 6$ cm on a 10x10 mesh. This group is optically thick and the hybrid scheme does not produce any oscillations. The other optically thick groups perform similarly for all moments of time. Figure 3.21 shows the cell-averaged values of the energy density in group 1 on a 20x20 mesh. There is no oscillatory behavior on this mesh either. Monotonization is not necessary in this regime.

(a) First Order   (b) Hybrid   (c) Monotonized Hybrid
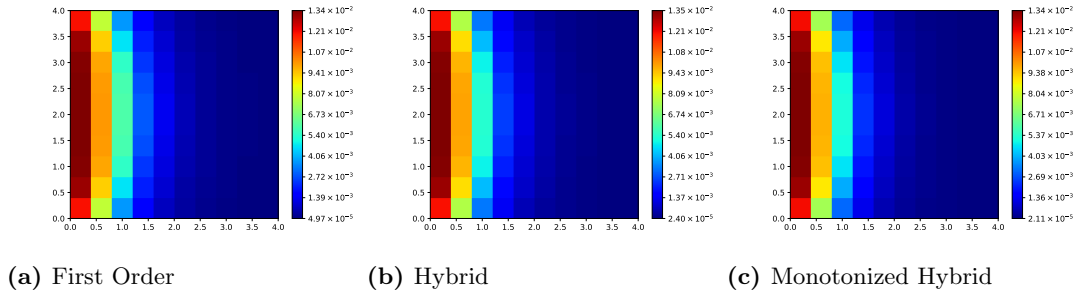
Figure 3.20 Cell-averaged values of the energy density (in $E \times 10^{-13} \frac{erg}{cm^3}$) computed with $\tau = 2 \times 10^{-3}$sh by the multi-level QD method using the MSS transport scheme in Group 1 on a 10x10 mesh.

(a) First Order   (b) Hybrid   (c) Monotonized Hybrid
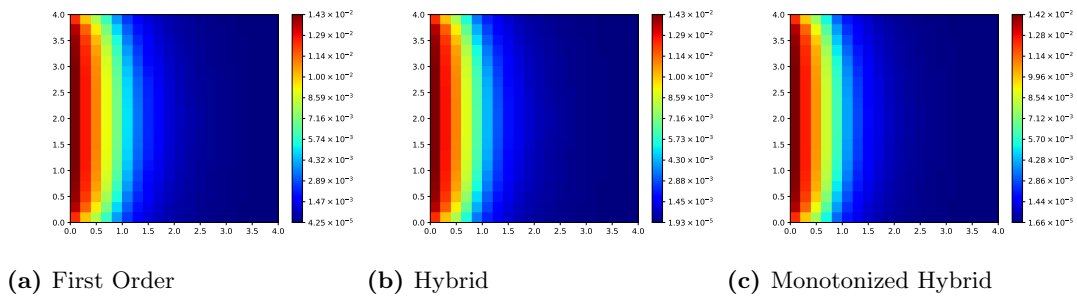
Figure 3.21 Cell-averaged values of the energy density (in $E \times 10^{-13} \frac{erg}{cm^3}$) computed with $\tau = 2 \times 10^{-3}$sh by the multi-level QD method using the MSS transport scheme in Group 1 on a 20x20 mesh.

47

Figure 3.22 shows the radiation energy density in group 13 (7 keV $\leq \nu \leq$ 9 keV) on a 10x10 mesh. This group is an intermediate energy group of the cusp of being a high energy group. The intermediate groups are mildly affected by the hybrid scheme but do not have non-monotonicity until group 13. This group is also important because the magnitude of the radiation is significant; therefore, the oscillatory effects will contribute noticeably to the total solution. Figure 3.23 shows the solution in group 13 on a 20x20 mesh. This mesh highlights non-monotonic behavior in regions besides what is seen beyond the wave front. There is a slight effect near the top and bottom boundary around $x = 1$ cm. There is also oscillatory behavior at this point and at the centerline, $y = 2$ cm. The monotonized hybrid scheme does well in correcting this behavior.

(a) First Order   **(b)** Hybrid   **(c)** Monotonized Hybrid
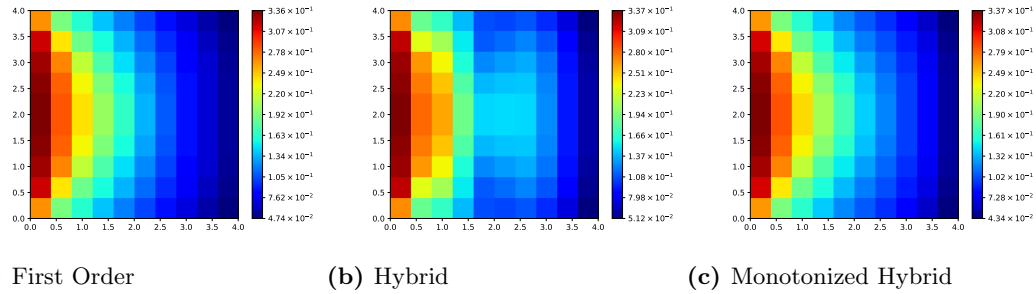
Figure 3.22 Cell-averaged values of the energy density (in $E \times 10^{-13} \frac{erg}{cm^3}$) computed with $\tau = 2 \times 10^{-3}$sh by the multi-level QD method using the MSS transport scheme in Group 13 on a 10x10 mesh.

(a) First Order   **(b)** Hybrid   **(c)** Monotonized Hybrid
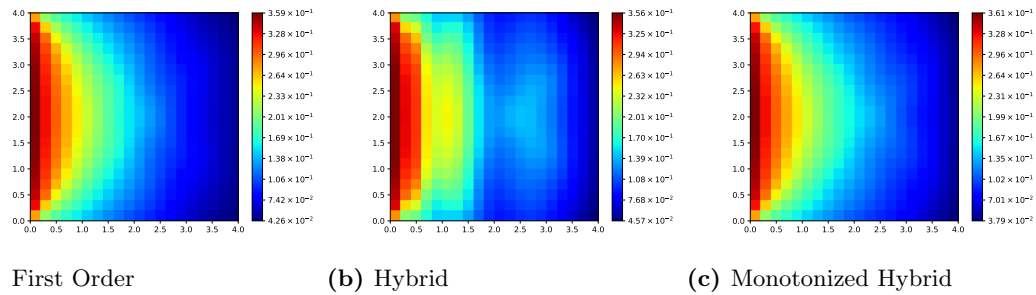
Figure 3.23 Cell-averaged values of the energy density (in $E \times 10^{-13} \frac{erg}{cm^3}$) computed with $\tau = 2 \times 10^{-3}$sh by the multi-level QD method using the MSS transport scheme in Group 13 on a 20x20 mesh.

48

Figure 3.24 shows the radiation energy density in group 16 (15 keV $\leq \nu \leq$ 20 keV) on a 10x10 mesh. This is a high-energy group and the oscillations are more prominent. Figure 3.25 shows the solution in group 16 for the 20x20 test case. There is significant oscillatory behavior in both the x-direction and the y-direction. The monotonized hybrid method does well in this group as well. The solution in a few orders of magnitude smaller than group 13 but the highly non-monotonic behavior will still have an effect.

(a) First Order   **(b)** Hybrid   **(c)** Monotonized Hybrid
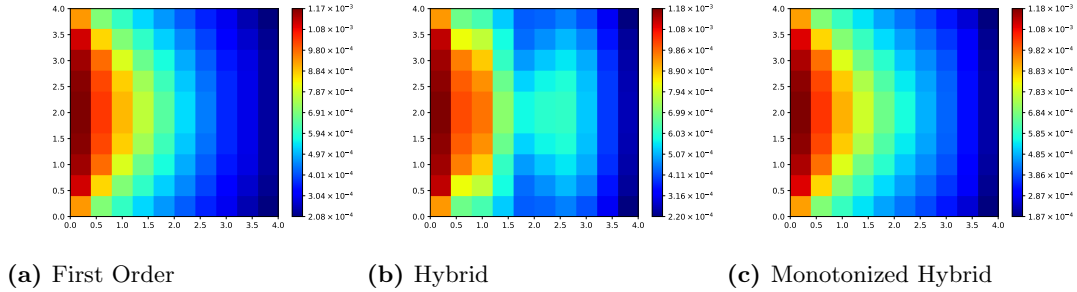
Figure 3.24 Cell-averaged values of the energy density (in $E \times 10^{-13} \frac{erg}{cm^3}$) computed with $\tau{=}2{\times}10^{-3}$sh by the multi-level QD method using the MSS transport scheme in Group 16 on a 10x10 mesh.

(a) First Order   **(b)** Hybrid   **(c)** Monotonized Hybrid
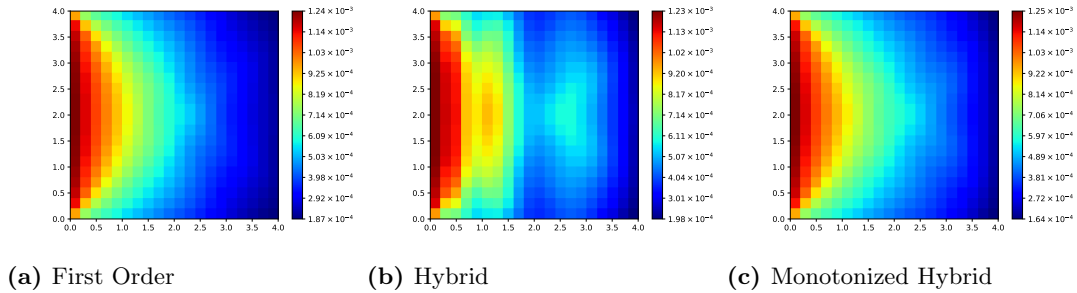
Figure 3.25 Cell-averaged values of the energy density (in $E \times 10^{-13} \frac{erg}{cm^3}$) computed with $\tau{=}2{\times}10^{-3}$sh by the multi-level QD method using the MSS transport scheme in Group 16 on a 20x20 mesh.

Figure 3.26 shows the spatial distribution of θ_g for the three groups of interest on a 10x10 mesh. Group 1 only has a derivative that is too large on the boundary of incoming radiation. The maximum θ is 0.7 therefore the L-TRAP scheme never switches to the first order in the optically thick group. Group 13 and Group 16 have similar distributions, but Group 16 has more cases of violating the monotonicity condition. In Group 13, there are a few cells on the boundary that revert to $\theta = 1$ and on the wave front, most cells have a θ close to 1. A meaningful amount

49

of non-local radiation has not reached the right boundary yet and therefore the gradient is small and the second-order scheme works fine. Figure 3.27 shows the spatial distribution of θ_g for the 20x20 test case. Since the mesh is refined, the gradient will be sharp and therefore there will be large derivatives. This effect is seen with the weights in group 1. There is no oscillatory behavior in the solution but the monotonicity condition is violated in a notable number of cells near the incoming boundary. Group 13 and 16 require monotonization at the wave front and near boundaries like the 10x10 case.
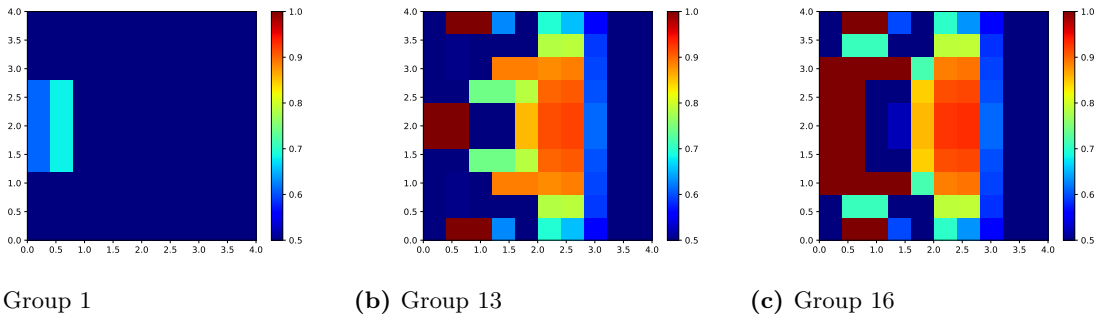
(a) Group 1   **(b)** Group 13   **(c)** Group 16

Figure 3.26 θ_g computed using the MSS transport scheme with $\tau=2\times10^{-3}$ sh by the monotonized hybrid scheme at ct = 6 cm on a 10x10 mesh.

(a) Group 1   **(b)** Group 13   **(c)** Group 16
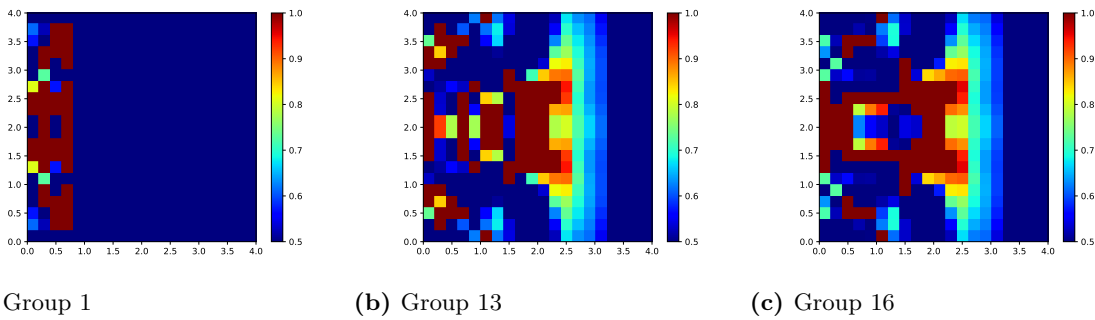
Figure 3.27 θ_g computed using the MSS transport scheme with $\tau=2\times10^{-3}$ sh by the monotonized hybrid scheme at ct = 6 cm on a 20x20 mesh.

While preserving monotonicity is important, the main goal is to improve on accuracy. Figure 3.28 shows the relative difference in the L_∞ norm between the solution at $\tau=2\times10^{-3}$ sh on

a 10x10 mesh and the numerically converged reference solution in time on the same spatial and angular mesh. This reference solution is obtained by doing successive refinements in time and using Aitken's method to compute an extrapolated solution. Refinement is done until the extrapolated solution has converged to the desired level of precision. There is a significant increase in accuracy in the material temperature when using the hybrid scheme. At the minimum, there is an order of magnitude smaller relative difference.

(a) $||T - T_{ref}||_{L_\infty}/||T_{ref}||_{L_\infty}$　　　　**(b)** $||E - E_{ref}||_{L_\infty}/||E_{ref}||_{L_\infty}$
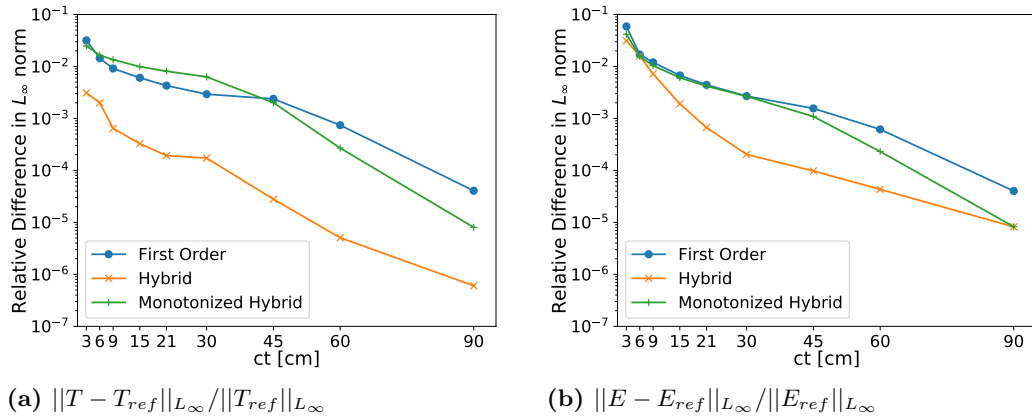
Figure 3.28 The relative difference of the solution obtained by the multi-level QD method using the MSS transport scheme compared to the reference solution in the L_∞ norm, $\tau = 2 \times 10^{-3}$ sh on a 10x10 mesh

(a) $||T - T_{ref}||_{L_2}/||T_{ref}||_{L_2}$　　　　**(b)** $||E - E_{ref}||_{L_2}/||E_{ref}||_{L_2}$
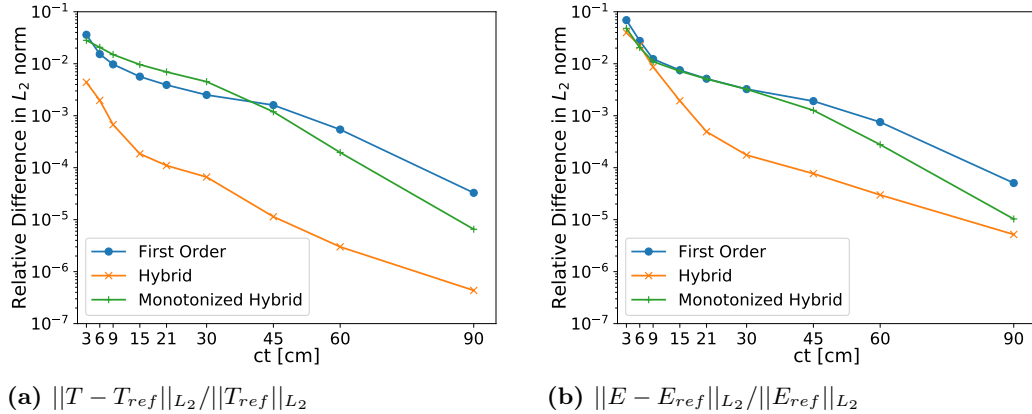
Figure 3.29 The relative difference of the solution obtained by the multi-level QD method using the MSS transport scheme compared to the reference solution in the L_2 norm, $\tau = 2 \times 10^{-3}$ sh on a 10x10 mesh.

When the change rate is large, the temperature obtained by the monotonized hybrid method is slightly less accurate than the first-order scheme. The total energy density does not show an

improvement on accuracy until around $ct = 9$ cm where the separation begins for the hybrid scheme. The monotonized hybrid method is close to the first-order scheme in this case. It tends to the accuracy of the hybrid scheme when equilibrium is reached which is expected. Figure 3.29 shows the relative difference in the L_2 norm on a 10x10 mesh. The behavior in this norm resembles that of the L_∞ norm. Figure 3.30 shows the convergence in time of the material temperature and total energy density in the L_∞ norm at $ct = 6$ cm. The three methods have first order convergence as expected. The QD factors are calculated using the solution from a first-order time discretization of the RT equation which restricts the hybrid method from achieving a faster rate of convergence. The monotonized hybrid scheme has a temporary increase in convergence rate for a few time steps. This is due to the L-TRAP scheme moving from a scheme dominated with $\theta = 1$ to a scheme dominated with $\theta = 0.5$. It still converges with the first order in the limit. The energy density has a more complex behavior compared to the temperature which shifts more uniformly. The density shows a decrease in the rate and then a sudden increase which appears to be compensation for the small increase in the difference on the previous time step. This behavior can be attributed to the more complicated nature of the radiation wave which has contribution from local and non-local radiation, where the material temperature is a local quantity.
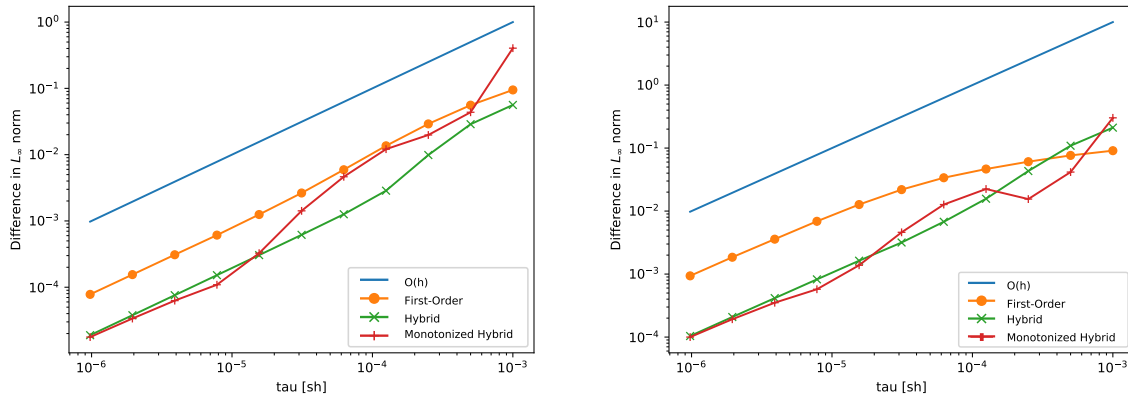
(a) $||T_\tau - T_{\tau/2}||_{L_\infty}$

(b) $||E_\tau - E_{\tau/2}||_{L_\infty}$

Figure 3.30 Convergence study at ct=6cm in the L_∞ norm for the solution obtained by the multilevel QD method using the MSS transport scheme on a 10x10 mesh.

The convergence behavior is similar in the L_1 and L_2 norms. At moments of time where the temperature and radiation waves are more developed, the convergence of the monotonized hybrid scheme resembles that of the hybrid scheme even with a large time step. It can be concluded

that monotonization is only necessary in the early stages of wave development and only for the higher energy groups.

3.4.2 Modified Simple Corner Balance (MSCB) Method

In this section, similar analysis is presented regarding accuracy, convergence, and shape of the solution obtained by the multi-level QD method using the MSCB transport scheme. This analysis reinforces what is seen with the MSS method and shows the performance with a scheme commonly used for TRT problems. Figures 3.31 and 3.32 compare the solution of the first-order scheme with that of the hybrid scheme using the MSCB method on a 10x10 mesh. There is change in the shape of radiation wave at $ct = 6$ cm that resembles the behavior seen with the MSS method. This effect does not appear in the comparison at the other two stages of wave development. Figures 3.33 and 3.34 shows the relative difference in the solution between the first-order and hybrid scheme on a 10x10 mesh. The largest difference at each stage is at the outgoing boundary. At $ct = 90$ cm, equilibrium is reached and the largest relative difference is on the order of 10^{-5}. Figures 3.35 and 3.36 compare the solution of the monotonized hybrid scheme with that of the hybrid scheme on a 10x10 mesh. The monotonized hybrid scheme generates a solution without oscillations. This corroborates the behavior seen with the montonized hybrid scheme applied to the multi-level QD method with the MSS transport scheme.

(a) $ct = 6$ cm   **(b)** $ct = 15$ cm   **(c)** $ct = 90$ cm
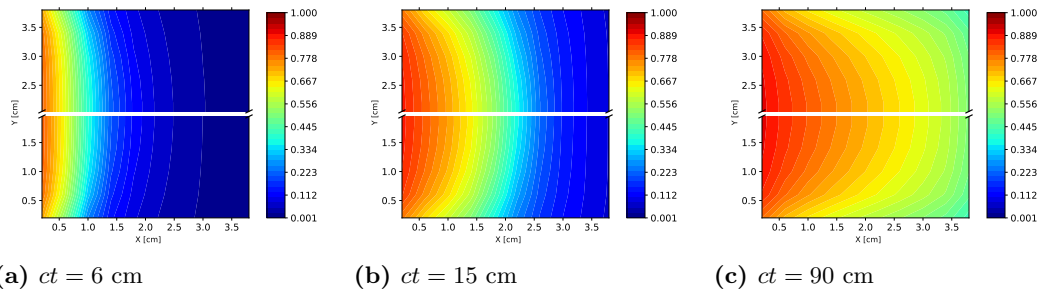
Figure 3.31 Temperature (in keV) computed by the multi-level QD method using the MSCB transport scheme with $\tau = 2 \times 10^{-3}$sh using (i) the first order method (top-half) and (ii) the hybrid method (bottom-half) on a 10x10 mesh.

53

(a) $ct = 6$ cm **(b)** $ct = 15$ cm **(c)** $ct = 90$ cm
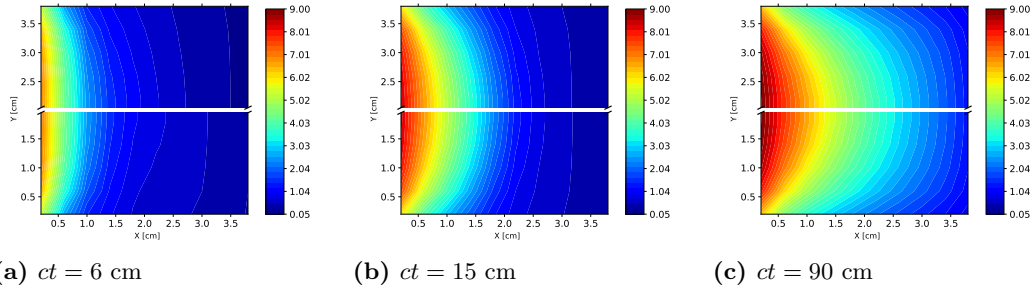
Figure 3.32 Total energy density ($E \times 10^{-13} \frac{erg}{cm^3}$) computed by the multi-level QD method using the MSCB transport scheme with $\tau = 2 \times 10^{-3}$sh using (i) the first order method (top-half) and (ii) the hybrid method (bottom-half) on a 10x10 mesh.

(a) $ct = 6$ cm **(b)** $ct = 15$ cm **(c)** $ct = 90$ cm
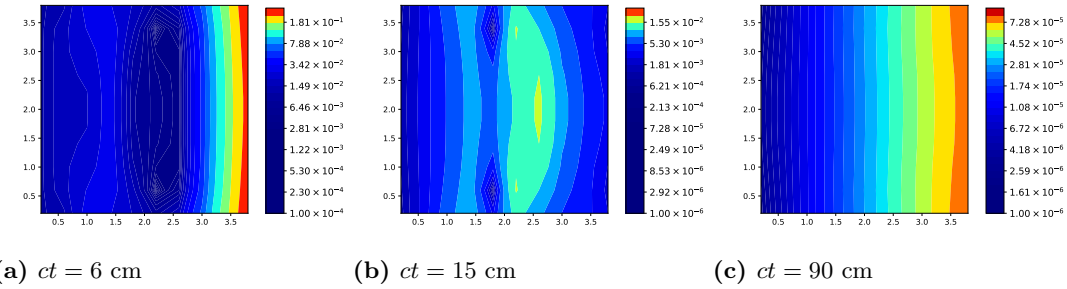
Figure 3.33 Relative difference in temperature computed by the multi-level QD method using the MSCB transport scheme with $\tau = 2 \times 10^{-3}$sh using (i) the first-order method (top-half) and (ii) the hybrid method (bottom-half) on a 10x10 mesh.

(a) $ct = 6$ cm **(b)** $ct = 15$ cm **(c)** $ct = 90$ cm
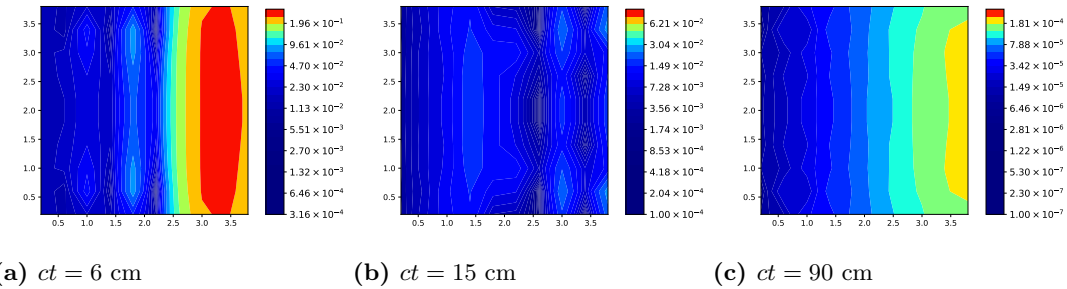
Figure 3.34 Relative difference in total energy density ($E \times 10^{-13} \frac{erg}{cm^3}$) computed by the multi-level QD method using the MSCB transport scheme with $\tau = 2 \times 10^{-3}$sh using (i) the first-order method (top-half) and (ii) the hybrid method (bottom-half) on a 10x10 mesh.

(a) $ct = 6$ cm   **(b)** $ct = 15$ cm   **(c)** $ct = 90$ cm
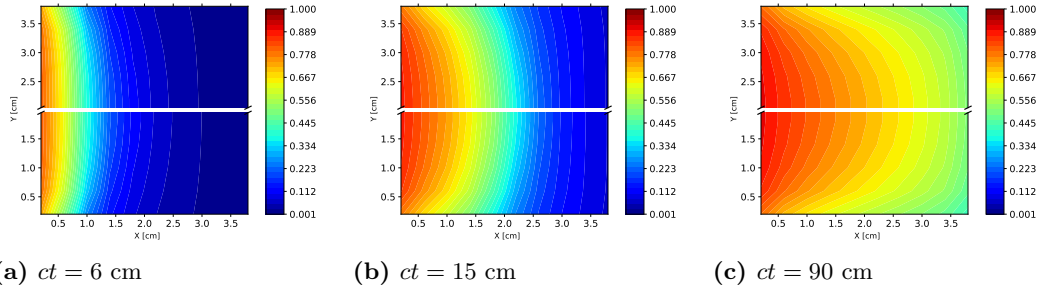
Figure 3.35 Temperature (in keV) computed by the multi-level QD method using the MSCB transport scheme with $\tau=2\times10^{-3}$sh using (i) the monotonized hybrid method (top-half) and (ii) the hybrid method (bottom-half) on a 10x10 mesh.

(a) $ct = 6$ cm   **(b)** $ct = 15$ cm   **(c)** $ct = 90$ cm
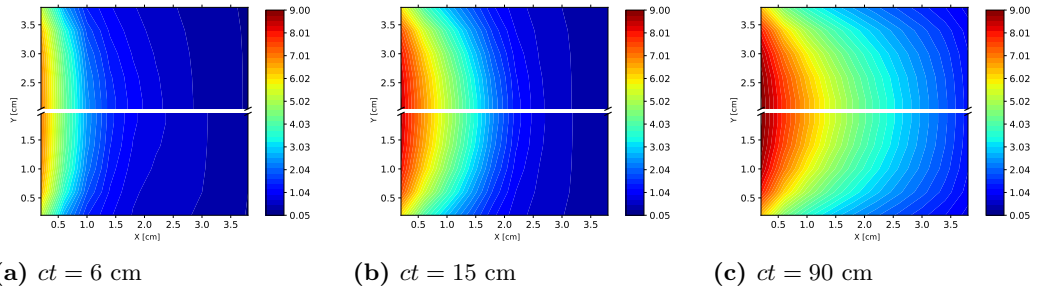
Figure 3.36 Total energy density ($E\times10^{-13}\frac{erg}{cm^3}$) computed by the multi-level QD method using the MSCB transport scheme with $\tau=2\times10^{-3}$sh using (i) the monotonized hybrid method (top-half) and (ii) the hybrid method (bottom-half) on a 10x10 mesh.

(a) $ct = 6$ cm   **(b)** $ct = 15$ cm   **(c)** $ct = 90$ cm
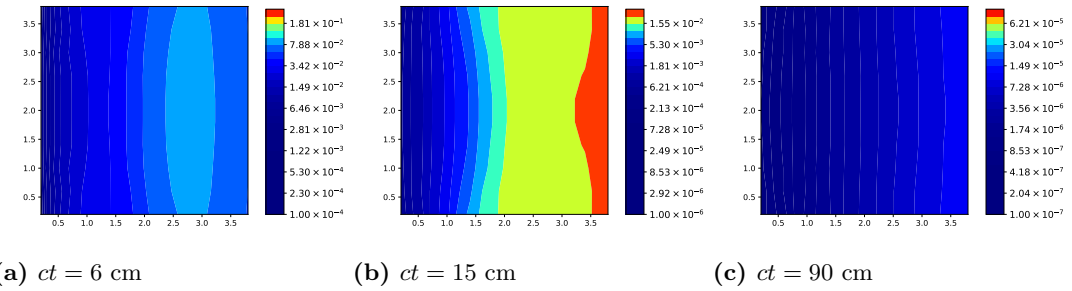
Figure 3.37 Relative difference in temperature computed by the multi-level QD method using the MSCB transport scheme with $\tau=2\times10^{-3}$sh using (i) the monotonized hybrid method (top-half) and (ii) the hybrid method (bottom-half) on a 10x10 mesh.

55

(a) $ct = 6$ cm **(b)** $ct = 15$ cm **(c)** $ct = 90$ cm
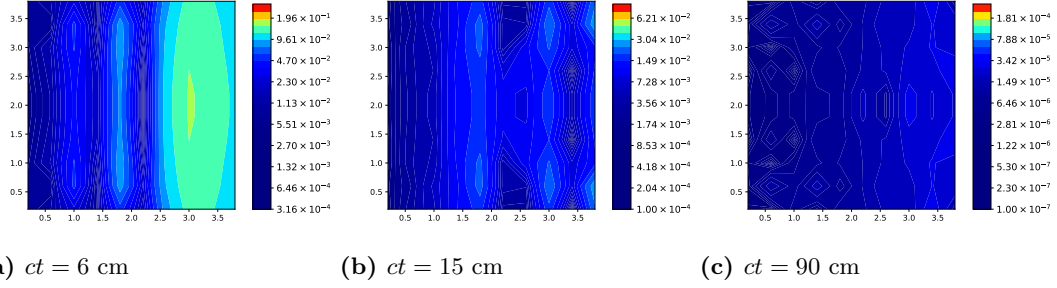
Figure 3.38 Relative difference in total energy density ($E \times 10^{-13} \frac{erg}{cm^3}$) computed by the multi-level QD method using the MSCB transport scheme with $\tau = 2 \times 10^{-3}$sh using (i) the monotonized hybrid method (top-half) and (ii) the hybrid method (bottom-half) on a 10x10 mesh.

The group energy density is examined in group 1 (0 keV $\leq \nu \leq$ 0.3 keV), group 13 (7 keV $\leq \nu \leq$ 9 keV), and group 16 (15 keV $\leq \nu \leq$ 20 keV) for the first-order, hybrid, and monotonized hybrid schemes using the MSCB method on a 10x10 mesh. The solution generated with the hybrid scheme is non-monotonic in the intermediate and high energy groups. This behavior is not seen in the optically thick group as seen in Figure 3.39. The oscillatory behavior is not as extreme compared to the MSS method. Figure 3.40 and 3.41 shows the monotonization procedure removes the oscillations in the radiation wave.

(a) First Order **(b)** Hybrid **(c)** Monotonized Hybrid
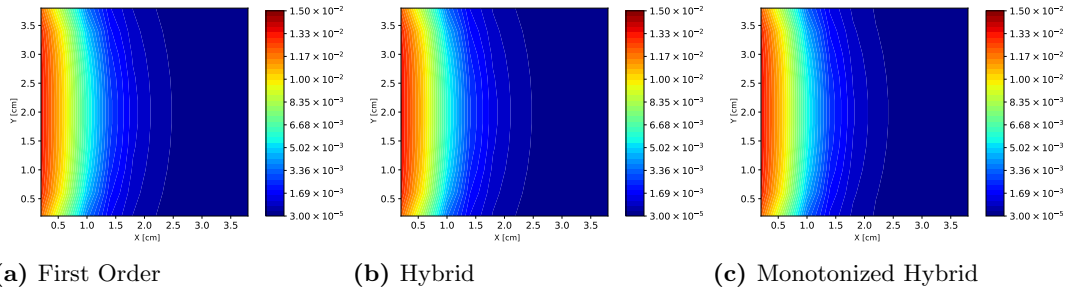
Figure 3.39 Energy Density (in $E \times 10^{-13} \frac{erg}{cm^3}$) computed with $\tau = 2 \times 10^{-3}$sh by the multi-level QD method in Group 1 using the MSCB transport scheme on a 10x10 mesh.

56

(a) First Order   **(b)** Hybrid   **(c)** Monotonized Hybrid
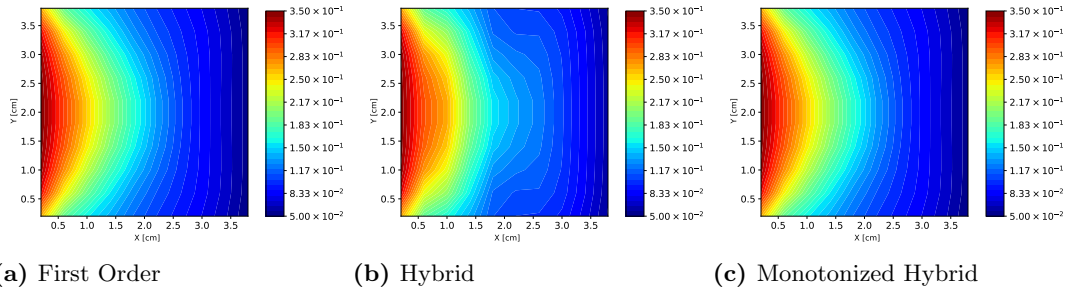
Figure 3.40 Energy Density (in $E \times 10^{-13} \frac{erg}{cm^3}$) computed with $\tau = 2 \times 10^{-3}$sh by the multi-level QD method in Group 13 using the MSCB transport scheme on a 10x10 mesh.

(a) First Order   **(b)** Hybrid   **(c)** Monotonized Hybrid
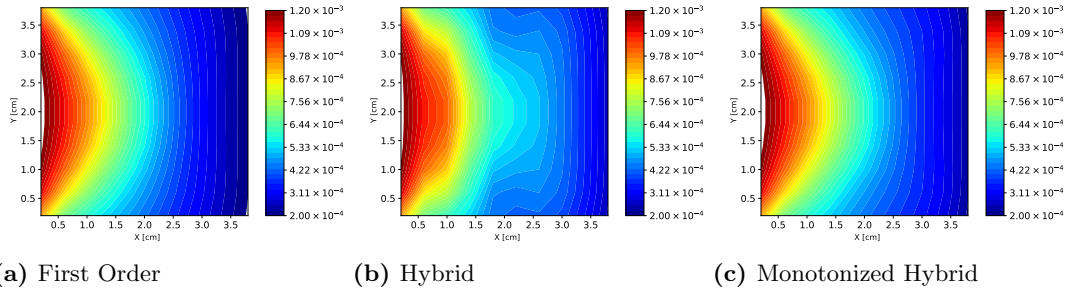
Figure 3.41 Energy Density (in $E \times 10^{-13} \frac{erg}{cm^3}$) computed with $\tau = 2 \times 10^{-3}$sh by the multi-level QD method in Group 16 using the MSCB transport scheme on a 10x10 mesh.

Figure 3.42 shows the spatial maps of θ_g for groups 1, 13, and 16 on a 10x10 mesh. The monotonization procedure estimates the solution in group 13 and group 16 produce derivatives of the wrong sign in a significant number of cells at the wave front, but this seldom occurs in group 1. The behavior in group 1 is similar when the multi-level QD method uses the MSS method and MSCB method. The L-TRAP scheme predicts the derivative has the wrong sign only on the boundary with the MSS scheme used for the high-order transport equation and that the derivative needs restriction at the wave front. The multi-level QD method with MSCB scheme has less cases of violating the monotonicity condition at the incoming boundary, but has more cases with the derivative having the wrong sign at the wavefront.

57

(a) Group 1   **(b)** Group 13   **(c)** Group 16
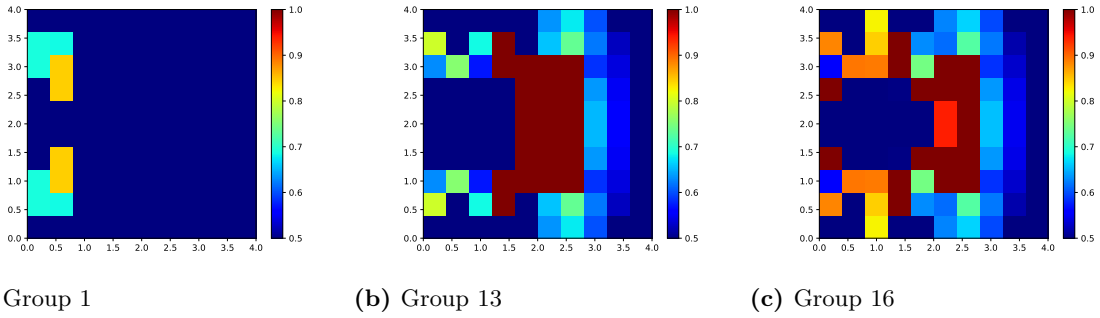
Figure 3.42 θ_g computed with $\tau=2\times10^{-3}$ sh by the monotonized hybrid scheme at ct = 6 cm using the MSCB transport scheme.

Figure 3.43 shows the relative difference in the L_∞ norm between the solution at $\tau=2\times10^{-3}$ sh on a 10x10 mesh and the numerically converged reference solution in time on the same spatial and angular mesh. The hybrid scheme gives better accuracy for both the material temperature and radiation energy density. The accuracy of the monotonized hybrid scheme tends to the first-order method when the change rate is large and to the accuracy of the hybrid scheme as it approaches equilibrium. Figure 3.44 shows the relative difference in the L_2 norm which coincides with that of the L_∞ norm.

(a) $||T - T_{ref}||_{L_\infty}/||T_{ref}||_{L_\infty}$ **(b)** $||E - E_{ref}||_{L_\infty}/||E_{ref}||_{L_\infty}$

Figure 3.43 The relative difference between the solution at $\tau=2\times10^{-3}$sh and the reference solution in the L_∞ norm obtained by the multi-level QD method using the MSCB transport scheme on a 10x10 mesh.

(a) $||T - T_{ref}||_{L_2}/||T_{ref}||_{L_2}$

(b) $||E - E_{ref}||_{L_2}/||E_{ref}||_{L_2}$

Figure 3.44 The relative difference between the solution at $\tau=2\times10^{-3}$sh and the reference solution in the L_2 norm obtained by the multi-level QD method using the MSCB transport scheme on a 10x10 mesh.

The solution obtained with the hybrid scheme has better accuracy than that of the first-order scheme. The L-TRAP monotonization procedure does well in removing the oscillatory behavior produced from using a high-order scheme. It tends to the accuracy of the first-order scheme when significant monotonization is required and to the the hybrid scheme when the monotonicity conditions are not violated. These results are shown using different spatial discretizations of the RT equation: the modified subcell step (MSS) and the modified simple corner balance (MSCB) method. These methods are shown to perform similarly on different spatial meshes as well.

3.5 Adaptive Monotonization Procedures for the Low-Order QD Equations

Monotonization procedures reduce the accuracy of high order methods and add more computational expense. To improve the efficiency of the method, it is beneficial to do monotonization only when it is absolutely necessary. The L-TRAP scheme checks a monotonicity condition in every spatial cell in every energy group which is an expensive operation. This procedure tends to be overly strict in some cases because the quantities used to determine when monotonicity is needed are approximate. Because of this, it performs monotonization where it is not needed. The goal of these alternate methods is to see if monotonization can be done with less expense.

There are a few different variants of how the monotonization procedure can be improved. The results from monotonized hybrid show that monotonzation in groups that are optically

59

thick is not needed. One variant is to perform monotonization using the L-TRAP scheme only in the transparent groups. It is clear which groups are extremely optically thick and thin but it is more difficult to classify the intermediate groups. Different group structures are tested to see how they perform. The naming convention of these methods will consist of *AMH* (Adaptive Monotonized Hybrid) to signify using the same L-TRAP procedure as the monotonized hybrid scheme along with the groups that are monotonized. These are the cases that are analyzed:

- **AMH 8-17**: C-N: Groups 1-7, L-TRAP: Groups 8-17

- **AMH 11-17**: C-N: Groups 1-10, L-TRAP: Groups 11-17

- **AMH 13-15**: C-N: Groups 1-12,16,17, L-TRAP: Groups 13-15

Another variant is to use a first-order scheme in the groups that are considered to need monotonization and then use a second-order method for the remaining groups. This method will be called *Partial Hybrid* scheme because it will be the equivalent of the hybrid scheme in some groups and the equivalent of the first-order scheme in the other groups. The naming convention will be the same where it will append the groups that switch to a first-order scheme as a form of monotonization.

- **P-Hybrid 8-17**: C-N: Groups 1-7, B-E: Groups 8-17

- **P-Hybrid 11-17**: C-N: Groups 1-10, B-E: Groups 11-17

- **P-Hybrid 13-15**: C-N: Groups 1-12,16,17, B-E: Groups 13-15

Each grouping has a specific purpose and should highlight where improvements in the monotonization method can be made. Groups 1-7 do not have oscillatory behavior. Monotonization is not required here at any moment of time. Groups 8-10 are considered intermediate groups and do not exhibit much oscillatory behavior either. These groups are a significant contribution to the spectrum where Group 10 is the largest. If monotonization is not done in these groups, it is expected that there will be a significant improvement in the accuracy. Groups 13-17 are the optically thin groups and they have significant oscillatory behavior. While Groups 16 and 17 may have the largest effects of non-monotonicity, their contribution to the total energy density is minimal therefore monotonization in these two groups should have a negligible effect. Therefore, the final method will just do monotonization in groups with significant oscillatory behavior and contribution to the total energy density.

Figures 3.45 and 3.46 show the accuracy of each montonized hybrid variant by comparing the material temperature and total energy density in different norms. These results are obtained with $\tau = 2 \times 10^{-3}$ sh on a 10x10 spatial grid. For the material temperature, the AMH 8-17 case

shows are very slight improvement compared to the monotonized hybrid scheme. AMH 11-17 shows about half an order of magnitude increase in accuracy over all moments of time. AMH 13-15 shows significant increase in accuracy and is the same order of magnitude as the hybrid scheme. For the total energy density, the overall trend is similar to what is seen for the material temperature. One difference is AMH 11-17 has a dip where it significantly decreases the difference at ct = 9 cm but this does not happen for AMH 13-15 or the hybrid scheme. Another difference is the AMH 13-15 has consistently better accuracy than the hybrid scheme. Figures 3.47 and 3.48 show the accuracy of each P-Hybrid variant by comparing the material temperature and total energy density in different norms. These results are obtained with $\tau=2\times10^{-3}$ sh on a 10x10 spatial grid. The trends are similar to the montonized hybrid variants. Once again, P-Hybrid 13-15 has better accuracy than the hybrid method. The P-Hybrid scheme is significantly cheaper than the AMH scheme because it does not need to use the L-TRAP monotonization procedure.

(a) $||T - T_{ref}||_{L_\infty}/||T_{ref}||_{L_\infty}$ (b) $||E - E_{ref}||_{L_\infty}/||E_{ref}||_{L_\infty}$
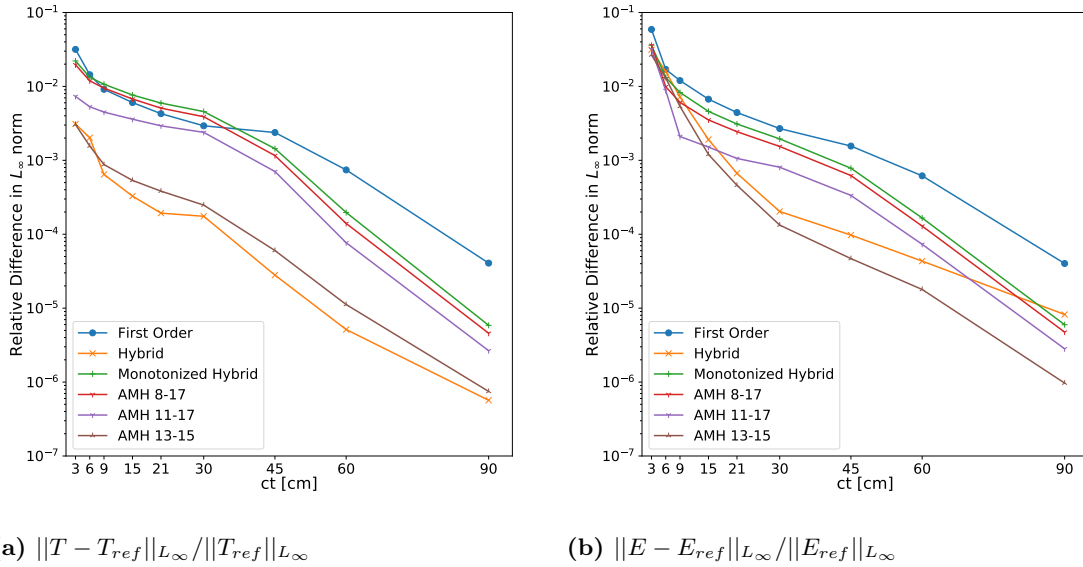
Figure 3.45 The relative difference between the solution at $\tau=2\times10^{-3}$sh and the reference solution in the L_∞ norm obtained by the multi-level QD method using the MSS transport scheme with AMH on a 10x10 mesh.
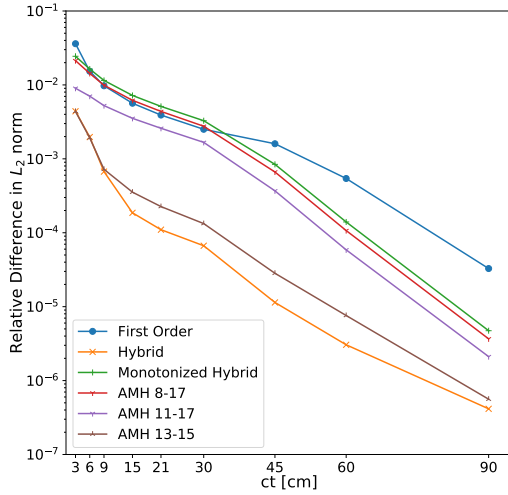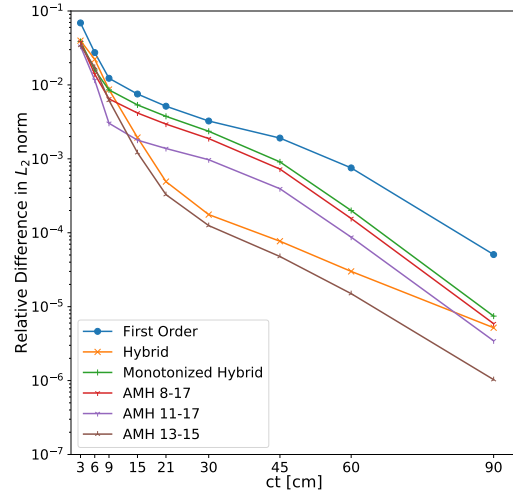
(a) $||T - T_{ref}||_{L_2}/||T_{ref}||_{L_2}$

(b) $||E - E_{ref}||_{L_2}/||E_{ref}||_{L_2}$

Figure 3.46 The relative difference between the solution at $\tau{=}2{\times}10^{-3}$sh and the reference solution in the L_2 norm obtained by the multi-level QD method using the MSS transport scheme with AMH on a 10x10 mesh.
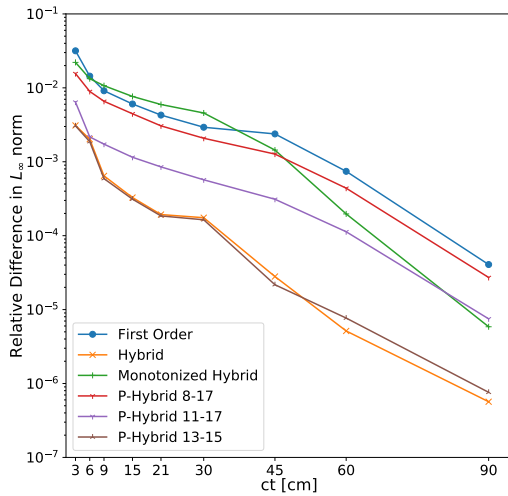
(a) $||T - T_{ref}||_{L_\infty}/||T_{ref}||_{L_\infty}$
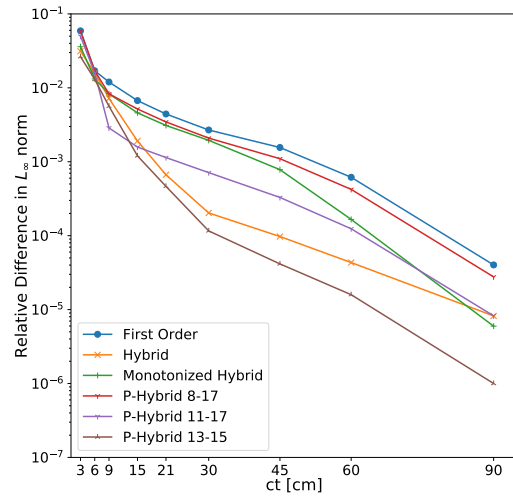
(b) $||E - E_{ref}||_{L_\infty}/||E_{ref}||_{L_\infty}$

Figure 3.47 The relative difference between the solution at $\tau{=}2{\times}10^{-3}$sh and the reference solution in the L_∞ norm obtained by the multi-level QD method using the MSS transport scheme with P-Hybrid on a 10x10 mesh.

62
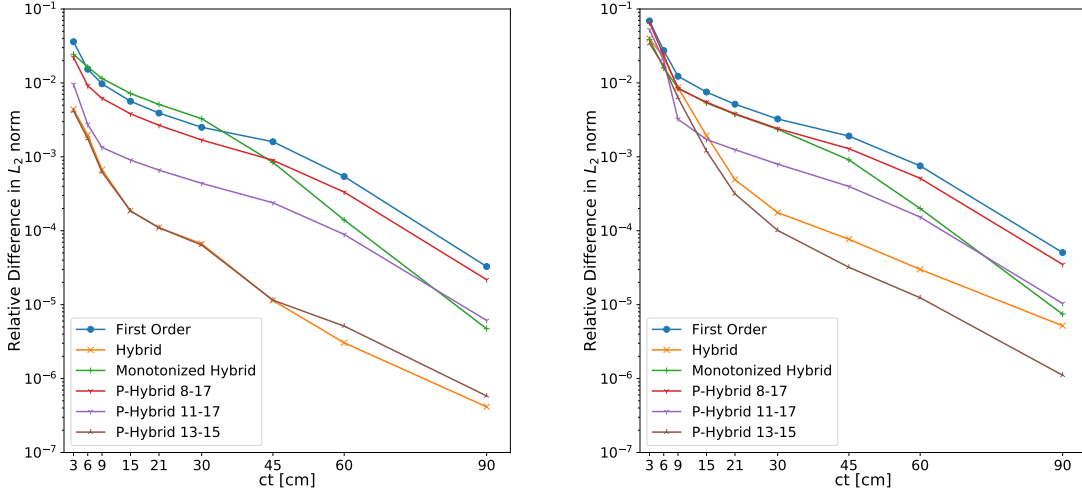
(a) $||T - T_{ref}||_{L_2}/||T_{ref}||_{L_2}$

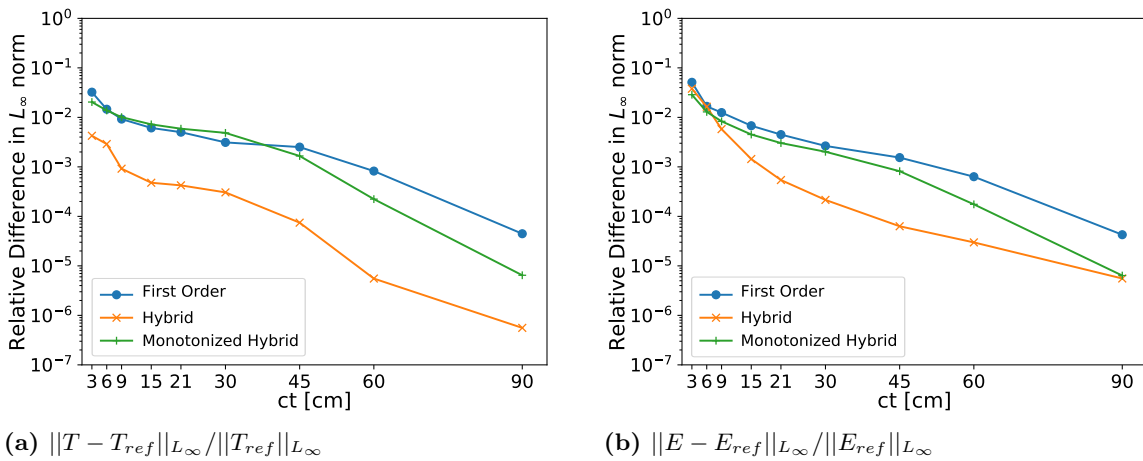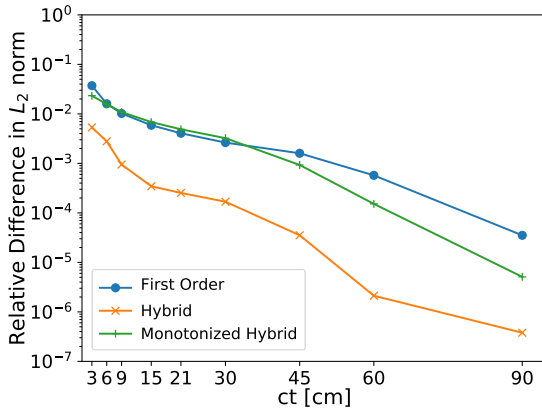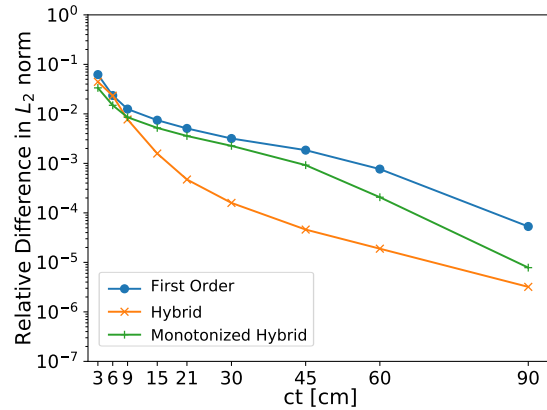**(b)** $||E - E_{ref}||_{L_2}/||E_{ref}||_{L_2}$

Figure 3.48 The relative difference between the solution at $\tau=2\times10^{-3}$sh and the reference solution in the L_2 norm obtained by the multi-level QD method using the MSS transport scheme with P-Hybrid on a 10x10 mesh.

3.6 Analysis of Monotonization Scheme Applied to the Two-Level P_1 Method for TRT Problems

The L-TRAP scheme is applied to the two-level method for solving TRT problems using multigroup P_1 equations instead of the multigroup LOQD equations. This two-level method consists of (i) multigroup P_1 equations and (ii) grey P_1 equations. The time-dependent multigroup low-order QD equations naturally reduce to P_1 equations if the QD tensor $\boldsymbol{f}_g = diag(\frac{1}{3}, \frac{1}{3})$. This also yields $\bar{\boldsymbol{f}} = diag(\frac{1}{3}, \frac{1}{3})$. In TRT problems, regions with significant spatial gradients are common and diffusion theory can result in a nonphysical solution (the energy density times the speed of light exceeds the flux). Various flux-limiting methods are used to prevent this in most cases [53]. Figures 3.49 and 3.50 show the material temperature and the total energy density obtained by the multigroup P1 equations approximated with the B-E scheme using $\tau=2\times10^{-3}$ on a 10x10 mesh. The solution does not exhibit any non-physical behavior. Because these are grey quantities, issues with flux limiting may not be apparent in the solution. These types of issues are most likely to occur in the high-energy groups.

63

(a) $ct = 6$ cm   **(b)** $ct = 15$ cm   **(c)** $ct = 90$ cm
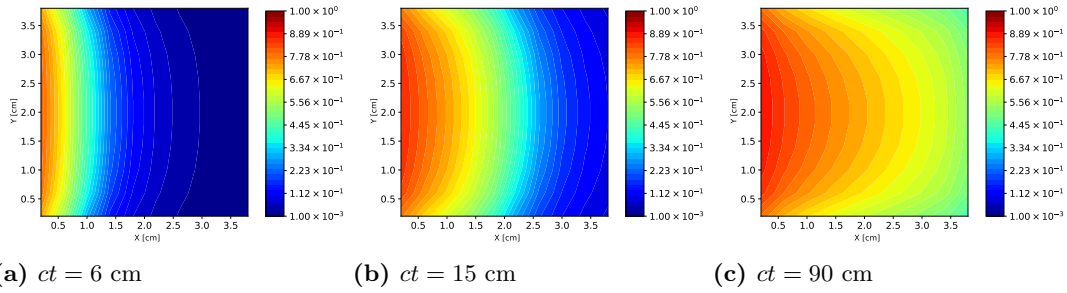
Figure 3.49 Temperature (in keV) computed by the two-level P_1 method using the backward-Euler scheme with $\tau = 2 \times 10^{-3}$sh on a 10x10 mesh.

(a) $ct = 6$ cm   **(b)** $ct = 15$ cm   **(c)** $ct = 90$ cm
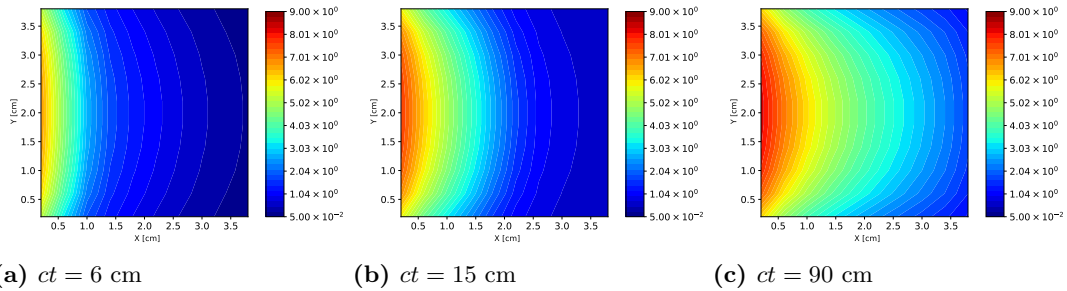
Figure 3.50 Total energy density ($E \times 10^{-13} \frac{erg}{cm^3}$) computed by the two-level P_1 method using the backward-Euler scheme with $\tau = 2 \times 10^{-3}$sh on a 10x10 mesh.

Figures 3.51 and 3.52 show the solution using a C-N time discretization with $\tau = 2 \times 10^{-3}$ sh on a 10x10 mesh. The radiation wave at $ct = 6$ cm is nonmonotonic. Although this issue can occur without flux limiting, this can be attributed to the temporal discretization because the non-physical behavior did not appear when the equations were discretized with a first-order scheme. There is a slight difference in the radiation wave at $ct = 15$ cm compared to solution obtained with the B-E scheme, but there is not oscillatory behavior. Figures 3.53 and 3.54 show the solution using the L-TRAP scheme with $\tau = 2 \times 10^{-3}$ on a 10x10 mesh. This method generates a non-oscillatory radiation wave at $ct = 6$ cm where C-N did not. The solution closely resembles the one calculated using the B-E scheme. Any differences in the solution between the methods appear in the radiation wave; the behavior of the temperature wave is immune to the temporal discretization.

64

(a) $ct = 6$ cm   **(b)** $ct = 15$ cm   **(c)** $ct = 90$ cm
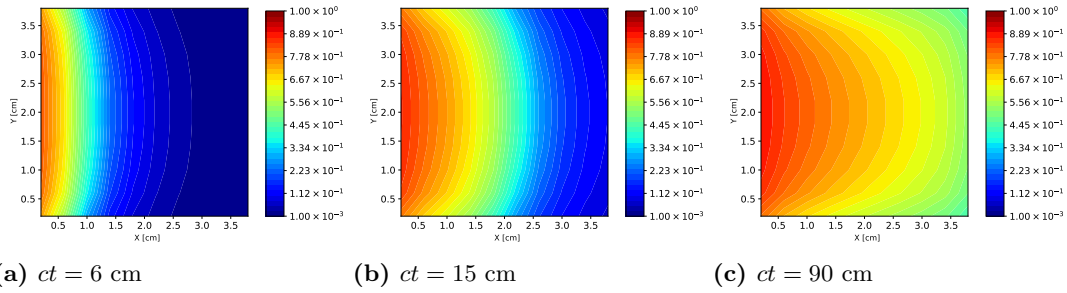
Figure 3.51 Temperature (in keV) computed by the two-level P_1 methods using the Crank-Nicolson scheme with $\tau = 2 \times 10^{-3}$sh on a 10x10 mesh.

(a) $ct = 6$ cm   **(b)** $ct = 15$ cm   **(c)** $ct = 90$ cm
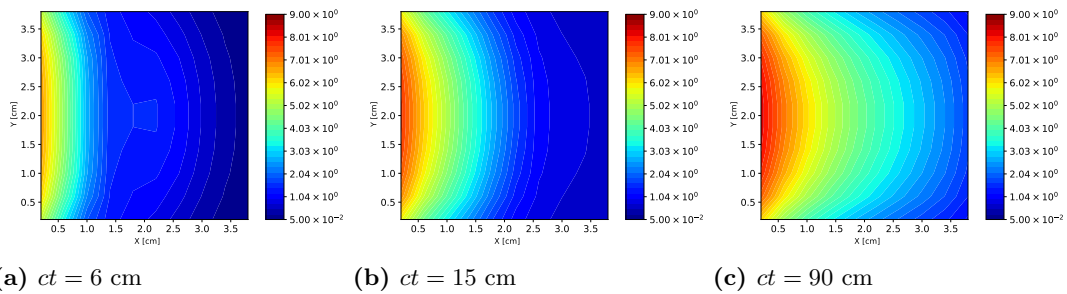
Figure 3.52 Total energy density $(E \times 10^{-13} \frac{erg}{cm^3})$ computed by the two-level P_1 method using the Crank-Nicolson scheme with $\tau = 2 \times 10^{-3}$sh on a 10x10 mesh.

(a) $ct = 6$ cm   **(b)** $ct = 15$ cm   **(c)** $ct = 90$ cm
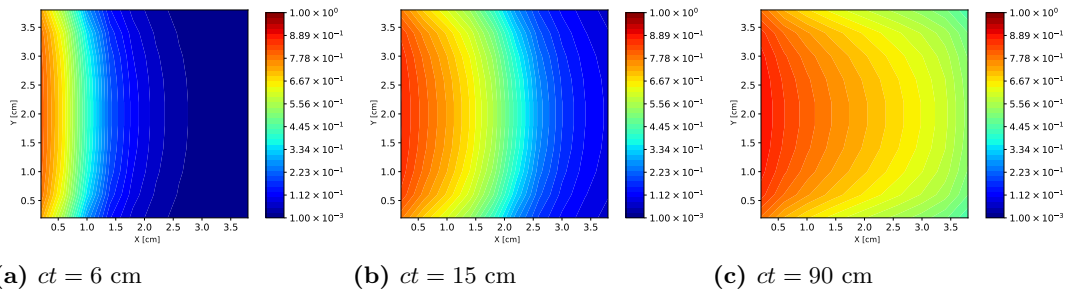
Figure 3.53 Temperature (in keV) computed by the two-level P_1 method using the L-TRAP scheme with $\tau = 2 \times 10^{-3}$sh on a 10x10 mesh.

(a) $ct = 6$ cm   **(b)** $ct = 15$ cm   **(c)** $ct = 90$ cm
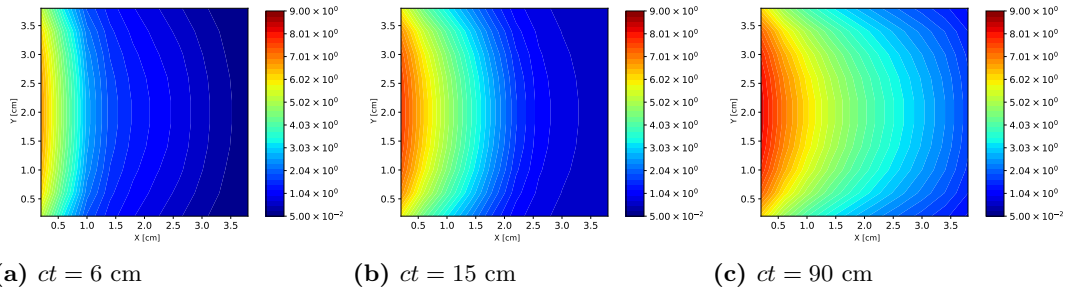
Figure 3.54 Total energy density $(E \times 10^{-13} \frac{erg}{cm^3})$ computed by the two-level P_1 method using the L-TRAP scheme with $\tau = 2 \times 10^{-3}$sh (top-half) on a 10x10 mesh.

Figure 3.55 shows the convergence in time of the material temperature and total energy density for the P_1 equations on a 10x10 mesh. Backward Euler converges with the first order and C-N converges with the second order. The solution with the L-TRAP scheme has two distinct convergence rates: for the first few times steps it converges linearly and then when the time step is small enough, it converges quadratically.
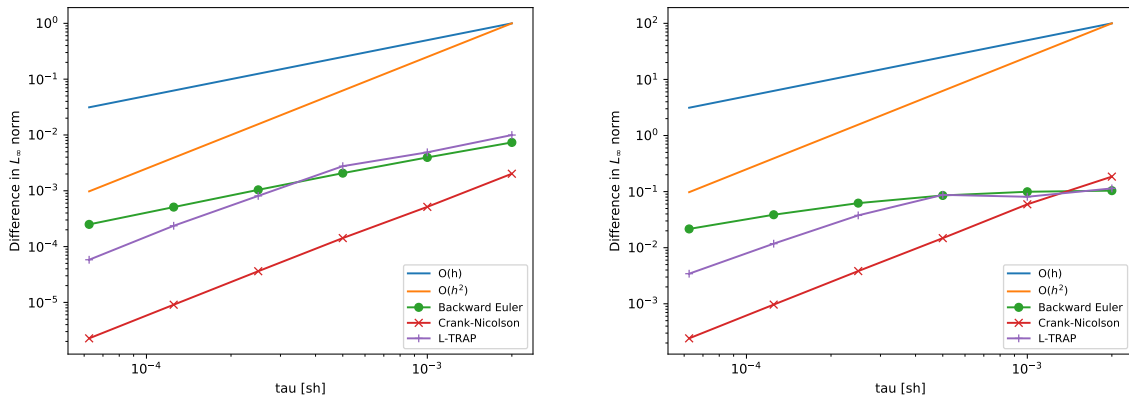
(a) $||T_\tau - T_{\tau/2}||_{L_\infty}$ **(b)** $||E_\tau - E_{\tau/2}||_{L_\infty}$

Figure 3.55 Convergence study at ct=6cm in the L_∞ norm for the two-level P_1 method on a 10x10 mesh.

66

CHAPTER

4

APPROXIMATE MODELS OF TIME DEPENDENCE IN MULTI-LEVEL QD METHODS

In this chapter, approximate models of time dependence in the RT equation are analyzed. The RT equation in α-approximation is analyzed and a new variant of α-approximation is developed. Results show that α-approximation does well in describing the evolution of radiation and temperature waves. Other approximate models are formulated and analyzed based on approximating the intensity from the previous time step. The new variant performs similarly to the original formulation of α-approximation. A part of the results presented in this chapter are published in [38].

4.1 Formulation of Approximate Models of Time Dependence in the RT Equation

The QD method exhibits stable convergence with varying discretization methods for the high-order and low-order problems. This is also the case when using approximate models rather that discretization methods. The RT equation is one of high-dimensionality and this requires some amount of storage of the solution from the previous time step. To get an idea of the storage of the information from the previous time step, the dimensionality of the high-order problem

and low-order problem is compared. For the low-order problem, the solution depends on space and energy group. If there are X number of cells and G number of groups, there will be X * G unknowns. The solution to the high-order problem will have the number of unknowns multiplied by the number of directions M. This increases the number of unknowns by, at least, an order of magnitude. Because of this property of the RT equation, it is desirable to solve the problem without storing this much data if it is possible to still obtain a reasonably accurate solution. The RT equation in α-approximation [11, 17, 18, 54] is studied for this class of problem. In addition, other approximate models are formulated such that the complete vector of the high-dimensional transport solution from previous time step does not need to be stored.

4.1.1 RT Equation in α-approximation

One of the existing approaches for treating the time dependence of the RT equation is the α-approximation [54]. The multigroup RT equation introduced in Chapter 2 is,

$$\frac{1}{c}\frac{\partial I_{g,m}(\boldsymbol{r},t)}{\partial t} + \boldsymbol{\Omega}_m \cdot \boldsymbol{\nabla} I_{g,m}(\boldsymbol{r},t) + \varkappa_{E,g}(T)I_{g,m}(\boldsymbol{r},t) = \varkappa_{pl,g}(T)B_g(T).\tag{4.1}$$

This approximation assumes that the high-order solution changes exponentially over a time step in the following form:

$$I_{g,m}(\boldsymbol{r},t) = \tilde{I}_{g,m}(\boldsymbol{r})e^{\alpha_g(\boldsymbol{r})t},\tag{4.2}$$

where α_g is the rate of change in group g. This is substituted in the RT equation which lead to the following approximation of the time derivative,

$$\frac{\partial I_{g,m}(\boldsymbol{r},t)}{\partial t} \approx \alpha_g(\boldsymbol{r})I_{g,m}(\boldsymbol{r},t).\tag{4.3}$$

α_g can be approximated using the solution from the low-order problem such that,

$$\alpha_g(\boldsymbol{r},t) = \frac{1}{E_g(\boldsymbol{r},t)}\frac{\partial E_g(\boldsymbol{r},t)}{\partial t} = \frac{\partial \ln E_g(\boldsymbol{r},t)}{\partial t}.\tag{4.4}$$

E_g is the group energy density obtained by solving the MLOQD equations. With this approximation, α_g depends solely on the low-order solution and the previous intensity is no longer required. The time-dependent high-order RT equation with the α-approximation takes the form of the steady-state equation with the modified opacity,

$$\boldsymbol{\Omega}_m \cdot \boldsymbol{\nabla} I_{g,m}^n(\boldsymbol{r}) + \left(\varkappa_{E,g}^n(T) + \frac{\alpha_g^n(\boldsymbol{r})}{c}\right)I_{g,m}^n(\boldsymbol{r}) = \varkappa_{pl,g}^n(T)B_g^n(T).\tag{4.5}$$

68

Equation (4.5) is discretized in angle and frequency at the current level in time, n. For the RT equation in α-approximation, the effective total opacity is defined as,

$$\tilde{\varkappa}(\boldsymbol{r}) = \varkappa_{E,g}^n(T) + \frac{\alpha_g^n(\boldsymbol{r})}{c}, \tag{4.6}$$

and the effective source term is,

$$S(\boldsymbol{r}) = \varkappa_{pl,g}^n(T)B_g^n(T). \tag{4.7}$$

This can be compared to Equation (2.43) which is the RT equation discretized in time using the B-E scheme. Note that the effective source term is just the Planckian source and no longer depends on the intensity.

4.1.2 RT Equation in Modified α-approximation

While the original formulation of α-approximation is general, the modified α-approxmiation is based off the backward-Euler time discretization of the RT equation. The multigroup RT equation with B-E temporal discretization introduced in Chapter 2 is,

$$\frac{1}{c}\frac{I_{g,m}^n(\boldsymbol{r}) - I_{g,m}^{n-1}(\boldsymbol{r})}{\tau^n} + \boldsymbol{\Omega}_m \cdot \boldsymbol{\nabla} I_{g,m}^n(\boldsymbol{r}) + \varkappa_{E,g}^n(T)I_{g,m}^n(\boldsymbol{r}) = \varkappa_{pl,g}^n(T)B_g^n(T), \tag{4.8}$$

Here it is assumed that the group intensity varies exponentially with during a time step such that,

$$I_{g,m}^n(\boldsymbol{r}) = I_{g,m}^{n-1}(\boldsymbol{r})e^{\alpha_g^n(\boldsymbol{r})\tau^n}, \tag{4.9}$$

Solving for the intensity on the previous time step, the approximation is,

$$I_{g,m}^{n-1}(\boldsymbol{r}) = I_{g,m}^n(\boldsymbol{r})e^{-\alpha_g^n(\boldsymbol{r})\tau^n}. \tag{4.10}$$

Substituting this approximation back into the RT equation gives us,

$$\frac{I_{g,m}^n(\boldsymbol{r})}{c\tau^n}\left(1 - e^{-\alpha_g^n(\boldsymbol{r})\tau^n}\right) + \boldsymbol{\Omega}_m \cdot \boldsymbol{\nabla} I_{g,m}^n(\boldsymbol{r}) + \varkappa_{E,g}^n(T)I_{g,m}^n(\boldsymbol{r}) = \varkappa_{pl,g}^n(T)B_g^n(T), \tag{4.11}$$

and once again this equation is rearranged such that it is in the form of a steady-state equation,

$$\boldsymbol{\Omega}_m \cdot \boldsymbol{\nabla} I_{g,m}^n(\boldsymbol{r}) + \left(\varkappa_{E,g}^n(T) + \frac{1}{c\tau^n}\left(1 - e^{-\alpha_g^n(\boldsymbol{r})\tau^n}\right)\right)I_{g,m}^n(\boldsymbol{r}) = \varkappa_{pl,g}^n(T)B_g^n(T). \tag{4.12}$$

α_g is calculated the same way as the α-approximation, namely, using Equation (4.4). The effective source term is the same as in the α-approximation, but there is a difference in the

69

effective opacity term. Note that with this approximation, there is dependence on the time step; whereas, α-approximation does not.

4.1.3 Model based on P_0-approximation of the Intensity

Another approach is to use models to approximate the intensity at the previous time step based on the RT equation discretized temporally with the B-E scheme (Equation (4.8)). The P_0-approximation assumes the group intensity from the previous time step is isotropic hence,

$$I_{g,m}^{n-1}(\boldsymbol{r}) = \frac{c}{4\pi} E_g^{n-1}(\boldsymbol{r}). \tag{4.13}$$

Substituting this approximation into Equation (4.8) gives us,

$$\frac{1}{c} \frac{I_{g,m}^n(\boldsymbol{r}) - \frac{c}{4\pi} E_g^{n-1}(\boldsymbol{r})}{\tau^n} + \boldsymbol{\Omega}_m \cdot \boldsymbol{\nabla} I_{g,m}^n(\boldsymbol{r}) + \varkappa_{E,g}^n(T) I_{g,m}^n(\boldsymbol{r}) = \varkappa_{pl,g}^n(T) B_g^n(T), \tag{4.14}$$

This equation is rearranged to take the form a steady-state one which is,

$$\boldsymbol{\Omega}_m \cdot \boldsymbol{\nabla} I_{g,m}^n(\boldsymbol{r}) + \left(\varkappa_{E,g}^n(T) + \frac{1}{c\tau^n} \right) I_{g,m}^n(\boldsymbol{r}) = \varkappa_{pl,g}^n(T) B_g^n(T) + \frac{1}{4\pi\tau^n} E_g^{n-1}(\boldsymbol{r}). \tag{4.15}$$

For the RT equation with the P_0-approximation of the previous intensity, the effective total opacity is defined as,

$$\tilde{\varkappa}(\boldsymbol{r}) = \varkappa_{E,g}^n(T) + \frac{1}{c\tau^n}, \tag{4.16}$$

and the effective source term is,

$$S(\boldsymbol{r}) = \varkappa_{pl,g}^n(T) B_g^n(T) + \frac{1}{4\pi\tau^n} E_g^{n-1}(\boldsymbol{r}). \tag{4.17}$$

The effective opacity is the same as the RT equation with B-E discretization. The effective source has an additional term from the previous time step. Because the cell-averaged energy density is used to approximate the intensity, the same smearing effect is expected as discussed in Chapter 3.

4.1.4 Model based on Minerbo Approximation of the Intensity

The Minerbo closure [55], also known as the maximum entropy closure, is used to approximate the intensity from the previous time step. This technique is from statistical mechanics and communication theory. It is a two moment approximation that describes the intensity by finding its most likely form consistent with these angular moments. The most likely distribution is the one that maximizes entropy [55–57]. The group intensity from the previous time step is

approximated such that,

$$I_g^{n-1}(\boldsymbol{r},\boldsymbol{\Omega}) \approx \tilde{I}_g^{n-1}(\boldsymbol{r},\boldsymbol{\Omega}) = a_g^{n-1}(\boldsymbol{r})e^{\boldsymbol{b}^{n-1}(\boldsymbol{r})\cdot\boldsymbol{\Omega}}. \qquad (4.18)$$

The conditions of $a_g^{n-1}(\boldsymbol{r})$ and $\boldsymbol{b}(\boldsymbol{r})$ are defined such that,

$$\frac{1}{c}\int_{4\pi}\tilde{I}_g^{n-1}(\boldsymbol{r},\boldsymbol{\Omega})d\Omega = E_g^{n-1}, \qquad (4.19)$$

$$\int_{4\pi}\boldsymbol{\Omega}\tilde{I}_g^{n-1}(\boldsymbol{r},\boldsymbol{\Omega})d\Omega = \boldsymbol{F}_g^{n-1}, \qquad (4.20)$$

which leads to,

$$a_g^{n-1}(\boldsymbol{r})\int_{4\pi}e^{\boldsymbol{b}^{n-1}(\boldsymbol{r})\cdot\boldsymbol{\Omega}}d\Omega = cE_g^{n-1}, \qquad (4.21)$$

$$a_g^{n-1}(\boldsymbol{r})\int_{4\pi}\boldsymbol{\Omega}e^{\boldsymbol{b}^{n-1}(\boldsymbol{r})\cdot\boldsymbol{\Omega}}d\Omega = \boldsymbol{F}_g^{n-1}. \qquad (4.22)$$

Using these relationships, and dropping the index for time and group for simplicity, $\boldsymbol{b}$ is related to E and $\boldsymbol{F}$ which gives,

$$\frac{\boldsymbol{F}}{cE} = \frac{\boldsymbol{b}}{b}\left(\coth b - \frac{1}{b}\right), \qquad (4.23)$$

where $b = |\boldsymbol{b}|$ and a is defined as,

$$a = \frac{cEb}{4\pi\sinh b}. \qquad (4.24)$$

This closure is nonlinear and the equations cannot be solved for analytically. A robust nonlinear method is required to solve the equations. An additional beneficial feature is the approximate intensity is guaranteed to be positive. The RT equation with the Minerbo approximation of the previous intensity is,

$$\boldsymbol{\Omega}_m\cdot\boldsymbol{\nabla}I_{g,m}^n(\boldsymbol{r}) + \left(\varkappa_{E,g}^n(T) + \frac{1}{c\tau^n}\right)I_{g,m}^n(\boldsymbol{r}) = \varkappa_{pl,g}^n(T)B_g^n(T) + \frac{a_g^{n-1}(\boldsymbol{r})}{c\tau^n}e^{\boldsymbol{b}^{n-1}(\boldsymbol{r})\cdot\boldsymbol{\Omega}}. \qquad (4.25)$$

4.2 Truncation Error Analysis of RT Equation in α-approximation

Truncation error analysis is done to analyze the accuracy and behavior of each scheme. It is a means of comparing the expected behavior and asymptotic properties of each method as a compliment to the numerical results. This is done for the RT equation discretized in time and for some of the approximate models of time dependence.

71

4.2.1 RT Equation with Backward-Euler Approximation

First, truncation error analysis is performed for the B-E scheme in time. The RT equation approximated with this method is,

$$\frac{1}{c}\frac{I_g^n - I_g^{n-1}}{\tau^n} + \boldsymbol{\Omega}\cdot\boldsymbol{\nabla}I_g^n + \varkappa_{E,g}^n I_g^n = \varkappa_{pl,g}^n B_g^n. \tag{4.26}$$

The previous intensity, I_g^{n-1} is expanded about $t = t^n$ which leads to,

$$I_g^{n-1} = I_g^n - \tau^n I_{t,g}^n + \frac{\tau^2}{2}I_{tt,g}^n + O(\tau^3), \tag{4.27}$$

where the notation for the derivatives are defined as,

$$I_{t,g}^n \equiv \frac{\partial I_g}{\partial t}, \quad\quad I_{tt,g}^n \equiv \frac{\partial^2 I_g}{\partial t^2}. \tag{4.28}$$

Substituting the expansion back into the equation gives the modified equation,

$$\frac{1}{c\tau^n}\left(\tau^n I_{t,g}^n - \frac{\tau^2}{2}I_{tt,g}^n + O(\tau^3)\right) + \boldsymbol{\Omega}\cdot\boldsymbol{\nabla}I_g^n + \varkappa_{E,g}^n I_g^n = \varkappa_{pl,g}^n B_g^n, \tag{4.29}$$

which simplifies to,

$$\frac{1}{c}I_{t,g}^n + \boldsymbol{\Omega}\cdot\boldsymbol{\nabla}I_g^n + \varkappa_{E,g}^n I_g^n - \varkappa_{pl,g}^n B_g^n = \frac{\tau^n}{2c}I_{tt,g}^n + O(\tau^2), \tag{4.30}$$

It is well known that this is a first-order accurate scheme and this is seen with the leading order error term. This modified equation is compared to the RT equation with approximate models of time dependence.

4.2.2 RT Equation in α-approximation

Truncation error analysis is done for the RT equation in α-approximation. α-approximation is applied for the current time step $(t^{n-1} \leq t \leq t^n)$ and the RT equation is evaluated at the current moment of time to get,

$$\boldsymbol{\Omega}\cdot\nabla I_g^n + \left(\varkappa_{E,g}^n + \frac{\alpha_g^n}{c}\right)I_g^n = \varkappa_{pl,g}^n B_g^n. \tag{4.31}$$

The approximate rate α_g^n is equal to,

$$\alpha_g^n = \frac{1}{\tau^n}\ln\left(\frac{E_g^n}{E_g^{n-1}}\right). \tag{4.32}$$

The expansion of E_g^{n-1} about $t = t^n$ is the following,

72

$$E_g^{n-1} = E_g^n - \tau^n E_{t,g}^n + \frac{\tau^2}{2} E_{tt,g}^n + O(\tau^3). \tag{4.33}$$

The Taylor series expansion of α_g^n results in,

$$\alpha_g^n = \frac{E_{t,g}^n}{E_g^n} - \tau^n \left(\frac{E_{tt,g}^n}{E_g^n} - \left(\frac{E_{t,g}^n}{E_g^n} \right)^2 \right) + O(\tau^2), \tag{4.34}$$

which gives the modified equation,

$$\frac{1}{c} \frac{I_g^n}{E_g^n} E_{t,g}^n + \mathbf{\Omega} \cdot \nabla I_g^n + \varkappa_{E,g}^n I_g^n - \varkappa_{pl,g}^n B_g^n = \frac{\tau^n}{2c} \left(\frac{E_{tt,g}^n}{E_g^n} - \left(\frac{E_{t,g}^n}{E_g^n} \right)^2 \right) I_g^n + O(\tau^2). \tag{4.35}$$

Compared to the B-E scheme, this method has some differences in the truncation errors. The leading order term for the B-E scheme is $\frac{\tau^n}{2c} I_{tt,g}^n$ and for the RT equation in α-approximation it is $\frac{\tau^n}{2c} \left(\frac{E_{tt,g}^n}{E_g^n} - \left(\frac{E_{t,g}^n}{E_g^n} \right)^2 \right) I_g^n$. The essential difference is the factor at the intensity in the first term, namely, $\frac{E_{t,g}^n}{E_g^n}$ due to approximate change rate. As the change rate goes to zero, the RT equation in α-approximation will tend to the same steady state equation as the B-E method. When the change rate is large, it is expected that there will be some difference between the two methods. In addition, the solution is expected to deviate from that of the B-E scheme when the intensity is highly anisotropic. Since α_g^n is calculated using the energy density, these rates do not take the anisotropy into account. These methods will also have a discrepancy in the solution with refinement in time when the change rate is large.

4.2.3 RT Equation in Modified α-approximation

Truncation error analysis is done for the RT equation in modified α-approximation. Modified α-approximation is applied to the RT equation and it is evaluated at the current moment of time to get,

$$\mathbf{\Omega} \cdot \nabla I_g^n + \left(\varkappa_{E,g}^n + \frac{1}{c\tau^n} \left(1 - e^{-\alpha_g^n \tau^n} \right) \right) I_g^n = \varkappa_{pl,g}^n B_g^n. \tag{4.36}$$

Based on the defintion of α_g in Equation (4.32),

$$e^{-\alpha_g^n \tau^n} = \frac{E_g^{n-1}}{E_g^n}, \tag{4.37}$$

73

thus giving the equation,

$$\boldsymbol{\Omega} \cdot \nabla I_g^n + \left(\varkappa_{E,g}^n + \frac{1}{c\tau^n} \left(1 - \frac{E_g^n}{E_g^{n-1}} \right) \right) I_g^n = \varkappa_{pl,g}^n B_g^n. \tag{4.38}$$

The expression for the expansion of $\frac{E_g^{n-1}}{E_g^n}$ about $t = t^n$ is,

$$\frac{E_g^{n-1}}{E_g^n} = 1 - \tau^n \left[\frac{E_{t,g}^n}{E_g^n} - \frac{\tau^n}{2} \frac{E_{tt,g}^n}{E_g^n} + O(\tau^2) \right], \tag{4.39}$$

and substituting this into the RT equation gives,

$$\boldsymbol{\Omega} \cdot \nabla I_g^n + \left(\varkappa_{E,g}^n + \frac{1}{c} \left(\frac{E_{t,g}^n}{E_g^n} - \frac{\tau^n}{2} \frac{E_{tt,g}^n}{E_g^n} + O(\tau^2) \right) \right) I_g^n = \varkappa_{pl,g}^n B_g^n. \tag{4.40}$$

The terms are rearranged and the modified equation of the RT equation in modified α-approximation is,

$$\frac{1}{c} \frac{I_g^n}{E_g^n} E_{t,g}^n + \boldsymbol{\Omega} \cdot \nabla I_g^n + \varkappa_{E,g}^n I_g^n - \varkappa_{pl,g}^n B_g^n = \frac{\tau^n}{2c} \frac{I_g^n}{E_g^n} E_{tt,g}^n + O(\tau^2). \tag{4.41}$$

The leading order truncation error term differs from the one of the RT equation in α-approximation. As τ^n goes to 0, the solution obtained from this method and α-approximation will tend to the solution of the same approximate equation.

4.2.4 Model based on P_0-approximation of the Intensity

The same can be done for the RT equation with the P_0-approximation of the previous intensity. E_g^{n-1} is expanded about $t = t^n$ as show in Equation (4.33). Substituting the expansion into the RT equation with the P_0-approximation gives the modified equation,

$$\frac{1}{c} E_{t,g}^n + \boldsymbol{\Omega} \cdot \nabla I_g^n + \varkappa_{E,g}^n I_g^n - \varkappa_{pl,g}^n B_g^n + \frac{1}{c\tau^n} \left(I_g^n - \frac{1}{4\pi} E_g^n \right) = \frac{\tau^n}{2c} E_{tt,g}^n + O(\tau^2). \tag{4.42}$$

When the change rate is large, the solutions will not match. There are a few extra terms with time derivatives that are not seen in the other methods. The modified equation shows that this method will only tend to the same solution as the B-E scheme when the intensity is isotropic and the change rate is small. Even at equilibrium, there will be a discrepancy unless the intensity is isotropic.

74

4.3   Numerical Results

The approximate models of time dependence are analyzed with numerical tests. The Fleck and Cummings test case is used for this analysis.

4.3.1 RT Equation in α-approximation

The solution of obtained using the first-order scheme and the RT equation in α-approximation are analyzed. The MSS transport scheme is the spatial discretization method. This is done for a 10x10 spatial mesh and uses quadruple range quadrature set with 36 angles per octant. Note that both methods have the same spatial and temporal discretization for the low-order problem. Figures 4.1 and 4.3 show the temperature and radiation wave for three stages of wave development. The RT equation in α-approximation does well in describing the evolution of the wave for each moment of time. Figures 4.2 and 4.4 show that the largest difference is at ct = 6cm. This is expected because the change rate is large due to the fast changing processes near the incoming radiation. Truncation error analysis shows that there will be a difference in the solution when this occurs. The spatial maps of the relative difference also indicate that the largest difference occurs at the boundary. Since radiation is anisotropic in this subdomain, α-approximation will deviate from the first-order scheme.

(a) $ct = 6$ cm   **(b)** $ct = 15$ cm   **(c)** $ct = 90$ cm

Figure 4.1   Temperature (in keV) computed with τ=2×10^{-3}sh by the multi-level QD method using (i) the first-order scheme (top half) and (ii) RT equation in α-approximation (bottom half).

(a) $ct = 6$ cm   **(b)** $ct = 15$ cm   **(c)** $ct = 90$ cm

Figure 4.2 Relative difference in temperature computed with $\tau=2\times10^{-3}$ sh using the RT equation in the α-approximation and the first-order scheme.

(a) $ct = 6$ cm   **(b)** $ct = 15$ cm   **(c)** $ct = 90$ cm

Figure 4.3 Energy density ($E\times10^{-13}\frac{erg}{cm^3}$) computed with $\tau=2\times10^{-3}$ sh by the multi-level QD method using (i) the first-order scheme (top half) and (ii) RT equation in α-approximation (bottom half).

(a) $ct = 6$ cm   **(b)** $ct = 15$ cm   **(c)** $ct = 90$ cm
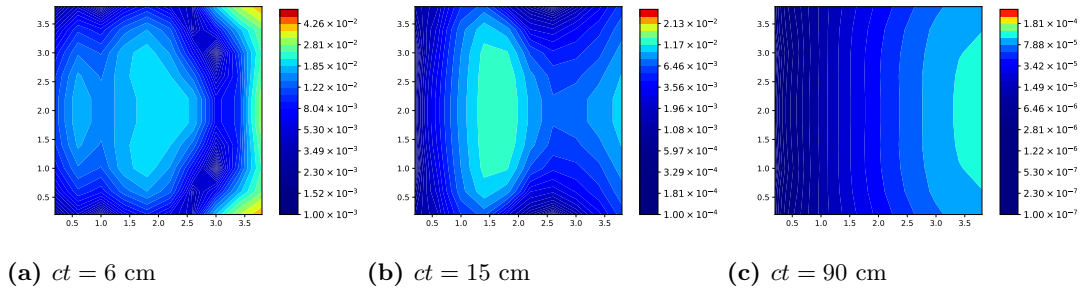
Figure 4.4 Relative difference in the energy density computed with $\tau=2\times10^{-3}$ sh using the RT equation in the α-approximation and the first-order scheme.

76

The differences are quantified in a few norms for temperature in Table 4.5 and for energy density in Table 4.6. The solution obtained with the first-order scheme is considered the reference. The difference is defined to be $||E_{ij} - E_{ref,ij}||_p$ and the relative difference to be $\frac{||E_{ij}-E_{ref,ij}||_p}{||E_{ref,ij}||_p}$ where p $= L_\infty, L_2$. For the L_2 norm, the results show a difference larger than that of the infinity norm in some cases. This is due to the area of test problem which is 0.16 cm^2. They show that maximum relative difference for the temperature is 5.03×10^{-3} and for the total density is 1.21×10^{-1}. As equilibrium is approached, the solutions for by methods tend to the same discrete steady state solution.

Table 4.1 Difference in Temperature computed by the multi-level QD method with the RT equation in α-approximation and the first-order scheme in different norms.

ct	L_∞	L_2	Rel L_∞	Rel L_2
6cm	3.32E-03	4.12E-03	5.03E-03	3.73E-03
15cm	2.80E-03	3.18E-03	5.17E-03	2.55E-03
90cm	2.17E-05	2.40E-05	5.00E-05	1.82E-05

Table 4.2 Difference in Total Energy Density computed by the multi-level QD method with the RT equation in α-approximation and the first-order scheme in different norms.

ct	L_∞	L_2	Rel L_∞	Rel L_2
6cm	7.83E-02	1.14E-02	1.12E-01	1.12E-02
15cm	4.64E-02	5.58E-03	7.43E-02	5.27E-03
90cm	2.17E-05	2.42E-06	5.41E-04	2.99E-05

Figures 4.5 shows the relative difference in temperature between these two methods with refinement in time. Figure 4.6 shows the same for total energy density. The relative difference in both temeperature and density tend to zero as equilibrium is approached. In the early stages of wave development, there is an increase in relative difference with refinement in time. This behavior can be explain with the modified equations. As τ goes to zero, the solutions for the two methods will differ when the change rate is large. Therefore the solutions will not converge with refinement in time for this stage of development.
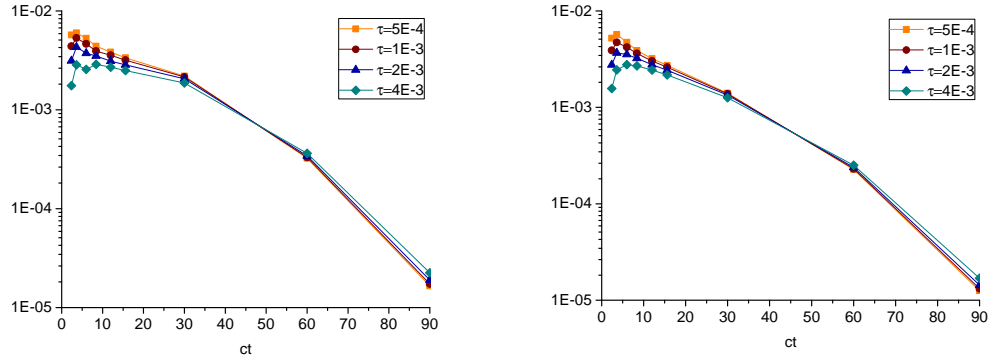
(a) L_∞-norm

(b) L_2-norm

Figure 4.5 The relative difference in temperature in L_∞ and L_2 norm.
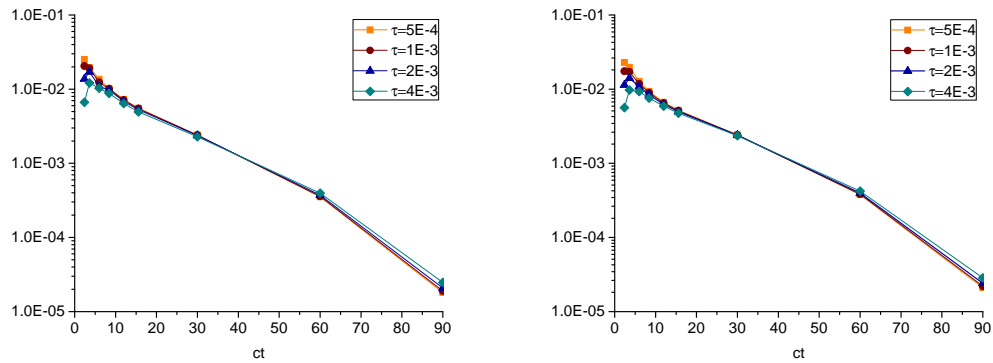
(a) L_∞-norm

(b) L_2-norm

Figure 4.6 The relative difference in energy density in L_∞ and L_2 norm.

4.3.2 RT Equation in Modified α-approximation

The RT equation in modified α-approximation is analyzed as well. The MSS transport scheme is used with a 10x10 spatial mesh and quadruple range quadrature set. The temperature and total energy density are shown in Figures 4.7 and 4.9 for the 3 stages of wave development. The relative differences in temperature and density are shown in Figures 4.8 and 4.10, respectively. The results show that the modified α-approximation gives a similar solution as the α-approximation. Minor differences can be seen in the plots of the relative difference but it exhibits the same general features regarding large change rates and transport effects.

78

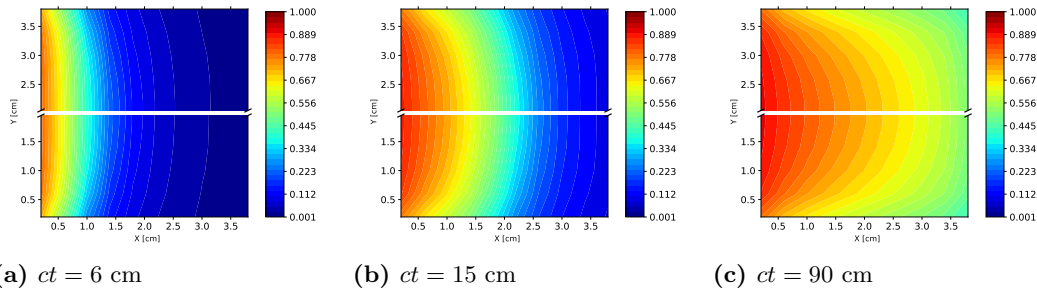**(a)** $ct = 6$ cm   **(b)** $ct = 15$ cm   **(c)** $ct = 90$ cm
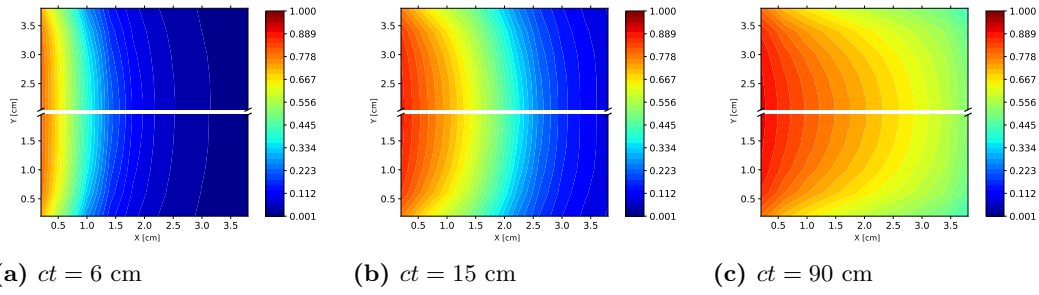
Figure 4.7 Temperature (in keV) computed with $\tau=2\times10^{-3}$sh by the multi-level QD method using (i) the first-order scheme (top half) and (ii) RT equation in modified α-approximation (bottom half).
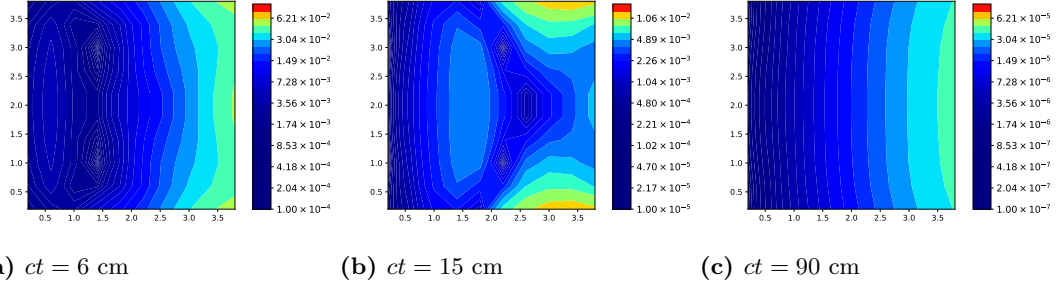

(a) $ct = 6$ cm   **(b)** $ct = 15$ cm   **(c)** $ct = 90$ cm

Figure 4.8 Relative difference in temperature computed with $\tau=2\times10^{-3}$ sh by the multi-level QD method using the RT equation in modified α-approximation and the first-order scheme.

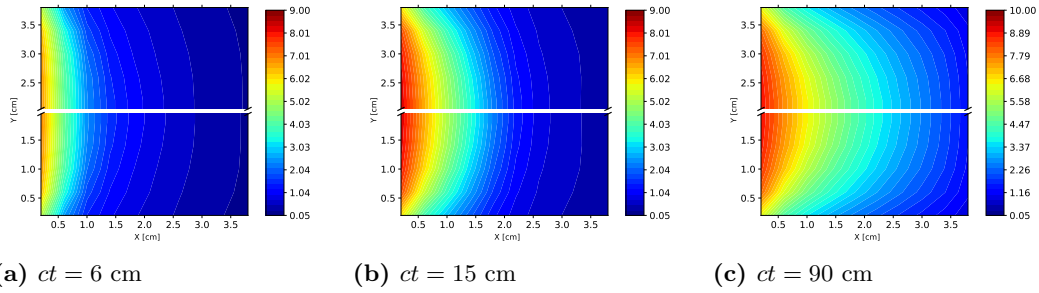**(a)** $ct = 6$ cm   **(b)** $ct = 15$ cm   **(c)** $ct = 90$ cm

Figure 4.9 Energy density ($E\times10^{-13}\frac{erg}{cm^3}$) computed with $\tau=2\times10^{-3}$ sh by the multi-level QD method using (i) the first-order scheme (top half) and (ii) RT equation in modified α-approximation (bottom half).

79

(a) $ct = 6$ cm   **(b)** $ct = 15$ cm   **(c)** $ct = 90$ cm

Figure 4.10 Relative difference in the energy density computed with $\tau=2\times10^{-3}$ sh by the multi-level QD method using the RT equation in the modified α-approximation and the first-order scheme.

In Tables 4.3 and 4.4, the similarities in the errors at each moment of time can be seen. This shows that the modified α-approximation performs similarly to α-approximation at all stages of wave evolution.

Table 4.3 Difference in Temperature computed by the multi-level QD method using the RT equation in the modified α-approximation and the first-order scheme in different norms

ct	L_∞	L_2	Rel L_∞	Rel L_2
6cm	3.73E-03	4.64E-03	5.64E-03	4.18E-03
15cm	2.88E-03	3.27E-03	5.36E-03	2.65E-03
90cm	2.17E-05	2.40E-05	4.99E-05	1.82E-05

Table 4.4 Difference in Total Energy Density computed by the multi-level QD method using the RT equation in the modified α-approximation and the first-order scheme in different norms.

ct	L_∞	L_2	Rel L_∞	Rel L_2
6cm	8.12E-02	1.18E-02	1.18E-01	1.17E-02
15cm	4.73E-02	5.69E-03	7.57E-02	5.37E-03
90cm	2.17E-05	2.42E-06	5.41E-04	2.99E-05

4.3.3 Model based on P_0-approximation of the Intensity

Numerical results are presented with the MSS transport scheme on a 10x10 spatial mesh and using quadruple range quadrature set. The temperature and total energy density obtained by the QD method with (i) the RT equation discretized in time and (ii) the RT equation with the P_0-approximation are shown and compared in Figures 4.11 and 4.13. The relative difference in temperature and in total density are shown in Figures 4.12 and 4.14, respectively.

(a) $ct = 6$ cm **(b)** $ct = 15$ cm **(c)** $ct = 90$ cm

Figure 4.11 Temperature (in keV) computed with $\tau = 2 \times 10^{-3}$sh by the QD method using (i) the first-order scheme (top half) and (ii) RT equation with P_0 approximation (bottom half).

(a) $ct = 6$ cm **(b)** $ct = 15$ cm **(c)** $ct = 90$ cm

Figure 4.12 Relative difference in temperature computed with $\tau = 2 \times 10^{-3}$ sh by the multi-level QD method using the RT equation with P_0 approximation and the first-order scheme.

(a) $ct = 6$ cm **(b)** $ct = 15$ cm **(c)** $ct = 90$ cm

Figure 4.13 Energy density $(E \times 10^{-13} \frac{erg}{cm^3})$ computed with $\tau = 2 \times 10^{-3}$ sh by the QD method using (i) the first-order scheme (top half) and (ii) RT equation with P_0 approximation (bottom half).
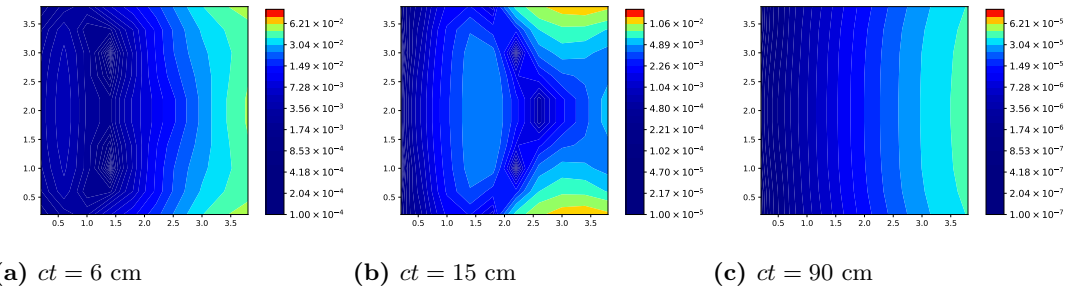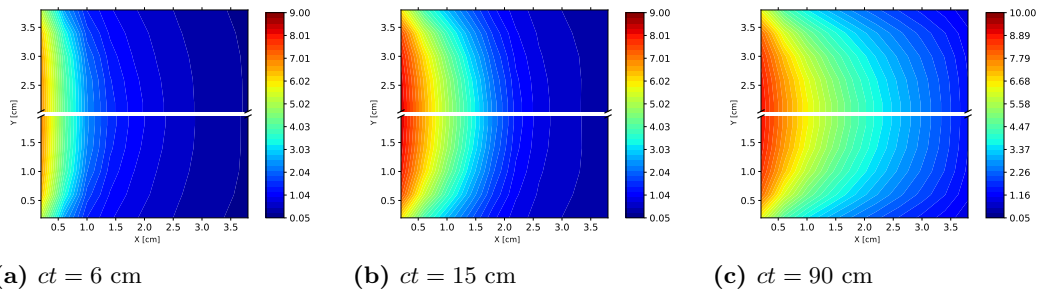
81

(a) $ct = 6$ cm   **(b)** $ct = 15$ cm   **(c)** $ct = 90$ cm
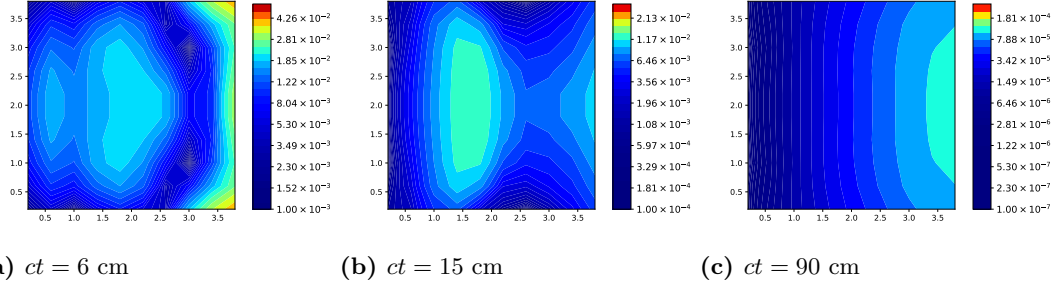
Figure 4.14 Relative difference in the energy density computed with $\tau = 2 \times 10^{-3}$ sh by the multi-level QD method using the RT equation with P_0 approximation and the first-order scheme.

The P_0-approximation introduces a significant smearing effect on the wave front. Also note that the steady state solution is different between the two methods which was shown in the analysis above. From the relative difference maps, it is clear that these methods do not tend to the same steady state solution. In each stage, the largest error is near the boundary where transport effects are largest for this test. The results shown in Tables 4.5 and 4.6 confirm this. At ct=90cm, the difference is large in all norms, most significantly for the total energy density. When looking at the difference in the energy density for each group at ct = 90 cm, the most optically thick group has the smallest maximum difference of 6.01×10^{-5}. As the groups become more optically thin, the difference increases such that the high energy groups have not converged to the same discrete steady state solution. P_0-approximation only does well in diffusive regions, as expected.

Table 4.5 Difference in the Temperature computed by the multi-level QD method with the RT equation in P_0 approximation and the first-order scheme in different norms.

ct	L_∞	L_2	Rel L_∞	Rel L_2
6cm	1.15E-02	1.43E-02	2.26E-02	1.67E-02
15cm	3.21E-02	3.64E-02	5.44E-02	2.69E-02
90cm	2.83E-02	3.13E-02	5.23E-02	1.91E-02

Table 4.6 Difference in the Total Energy Density computed by the multi-level QD method with the RT equation in P_0 approximation and the first-order scheme in different norms.

ct	L_∞	L_2	Rel L_∞	Rel L_2
6cm	4.76E-01	6.93E-02	6.43E-01	6.39E-02
15cm	9.50E-01	1.14E-01	1.22E+00	8.61E-02
90cm	2.83E-02	3.15E-03	1.85E+00	1.02E-01

www.manaraa.com

4.3.4 Model based on Minerbo Approximation of the Intensity

For numerical results, the temperature and total energy density obtained by the QD method with (i) the RT equation discretized in time and (ii) the RT equation with the Minerbo closure are shown and compared in Figures 4.15 and 4.17. The relative difference in temperature and the relative difference in total density are shown in Figures 4.16 and 4.18, respectively. At $ct = 6$ cm, the radiation wave with the Minerbo approximation has a slightly more smeared wave front. This effect is less notable at the more developed stages, but they still exhibit this feature. The largest differences are seen at the boundaries where there are significant transport effects. This is the case for both temperature and energy density.

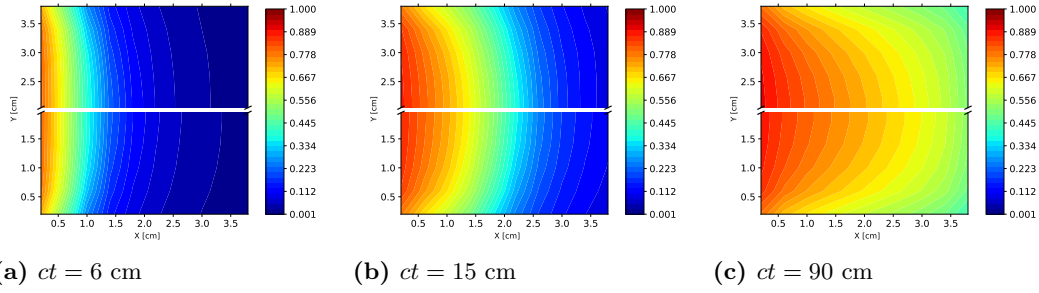| (a) $ct = 6$ cm | (b) $ct = 15$ cm | (c) $ct = 90$ cm |
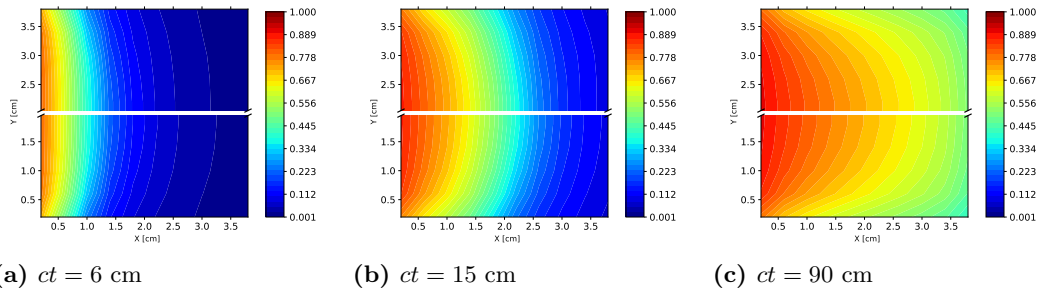
Figure 4.15 Temperature (in keV) computed with $\tau = 2 \times 10^{-3}$ sh by the QD method using (i) the first-order scheme (top half) and (ii) RT equation with the Minerbo closure (bottom half).

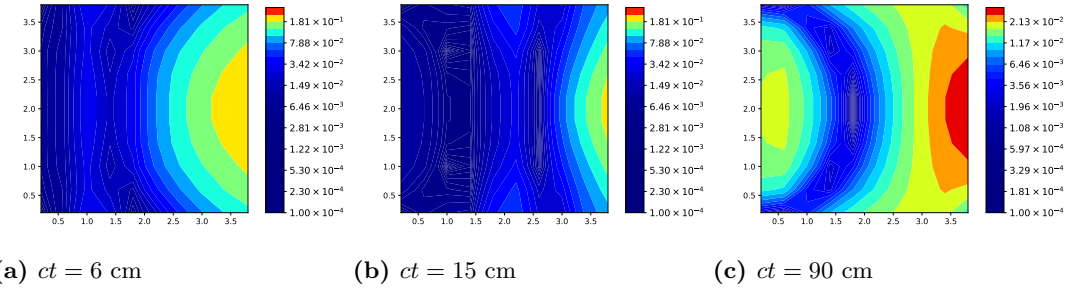| (a) $ct = 6$ cm | (b) $ct = 15$ cm | (c) $ct = 90$ cm |
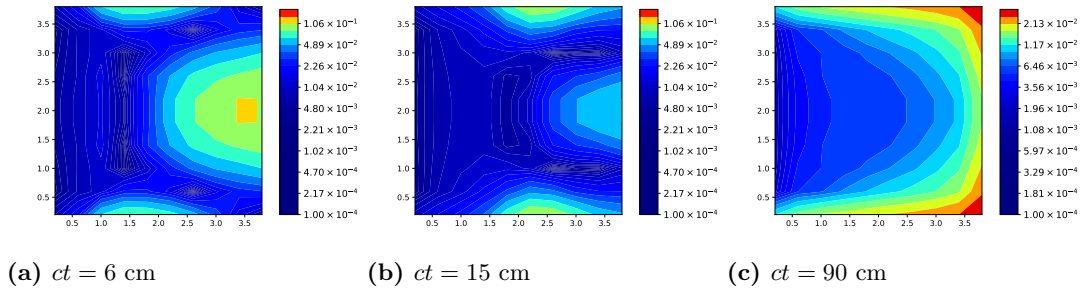
Figure 4.16 Relative difference in temperature computed with $\tau = 2 \times 10^{-3}$ sh by the multi-level QD method using the RT equation with the Minerbo closure and the first-order scheme.

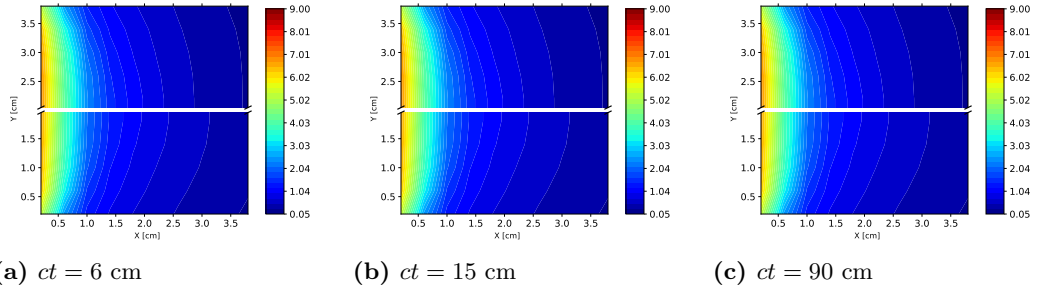**(a)** $ct = 6$ cm   **(b)** $ct = 15$ cm   **(c)** $ct = 90$ cm
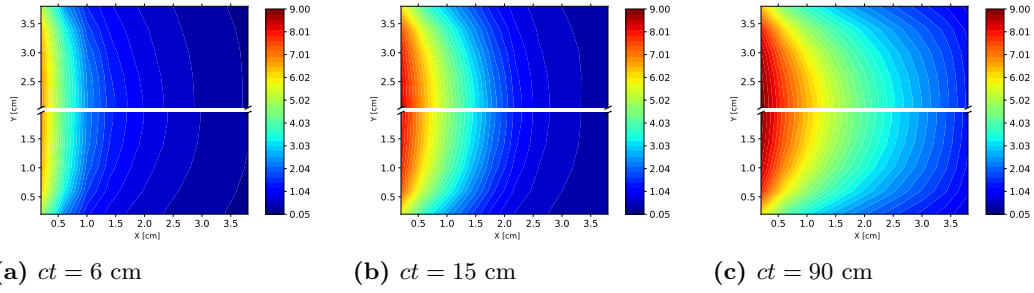
Figure 4.17 Energy density ($E \times 10^{-13} \frac{erg}{cm^3}$) computed with $\tau = 2 \times 10^{-3}$ sh by the QD method using (i) the first-order scheme (top half) and (ii) RT equation with the Minerbo closure (bottom half).

(a) $ct = 6$ cm   **(b)** $ct = 15$ cm   **(c)** $ct = 90$ cm
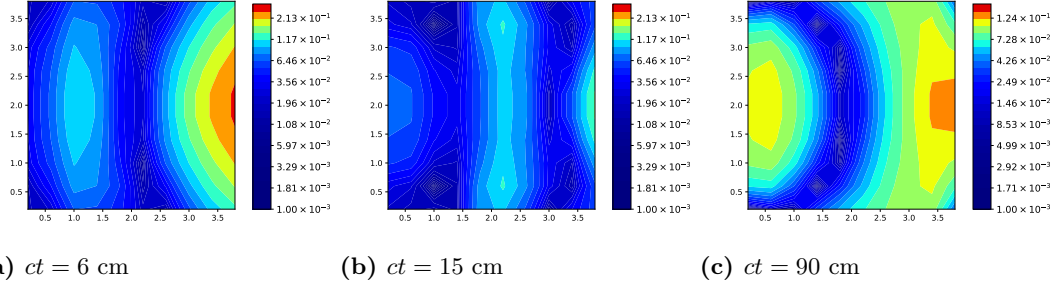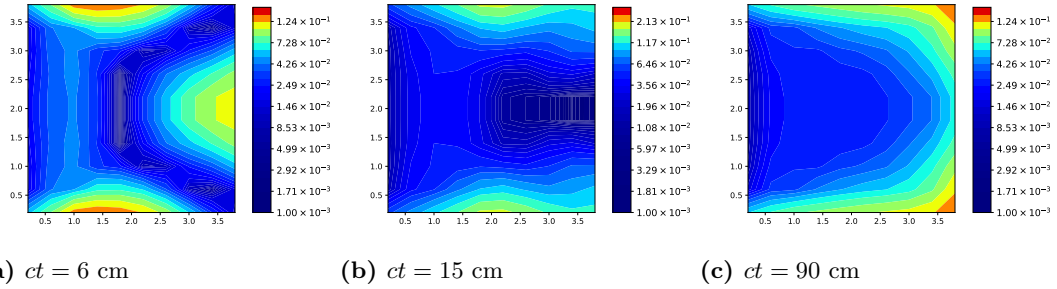
Figure 4.18 Relative difference in the energy density computed with $\tau = 2 \times 10^{-3}$ sh by the multi-level QD method using the RT equation with the Minerbo closure and the first-order scheme.

The solution obtained with the RT equation with the Minerbo approximation is compared to the solution calculated with the first-order scheme. The temperature and density does not tend to the same solution at equilibrium as the time-dependent method. The density is a couple orders of magnitude closer to the solution of the first-order scheme relative to the difference between the P_0-based approximation and the first-order scheme.

Table 4.7 Difference in the Temperature computed by the multi-level QD method using the RT equation with Minerbo closure and the first-order scheme in different norms.

ct	L_∞	L_2	Rel L_∞	Rel L_2
6cm	1.59E-02	1.97E-02	1.77E-02	1.32E-02
15cm	2.63E-02	2.98E-02	3.53E-02	1.74E-02
90cm	1.31E-02	1.44E-02	2.94E-02	1.07E-02

84

Table 4.8 Difference in the Total Energy Density computed by the multi-level QD method using the RT equation with Minerbo closure and the first-order scheme in different norms.

ct	L_∞	L_2	Rel L_∞	Rel L_2
6cm	2.77E-01	4.03E-02	3.55E-01	3.53E-02
15cm	3.40E-01	4.09E-02	5.50E-01	3.90E-02
90cm	3.62E-02	4.03E-02	6.23E-01	3.44E-02

CHAPTER

5

ANALYSIS OF ITERATIONS OF THE MULTI-LEVEL QD METHOD

An important aspect of methods development is optimizing the efficiency of the algorithm. A good metric to compare this aspect is by the number of iterations. Assuming each method does the same amount of computational work per iteration, one that requires less iterations is more efficient. The multilevel QD method consists of transport (outer) iterations, multigroup iterations, and grey (inner) iterations. In this chapter, the transport and multigroup iterations are analyzed for the first-order, hybrid, and monotonized hybrid scheme, as well as the MLQD method with RT in α-approximation.

5.1   Iteration Schemes for Multi-Level QD Methods

In Chapter 2, the algorithm for the first-order scheme is presented. Now, the iterative scheme for other multilevel QD methods are described to highlight the differences. The hybrid scheme does not change with regards to the algorithm besides using a different temporal discretization method for the low-order equations. Algorithm 3 shows how the MLQD equations are solved for the monotonized-hybrid scheme. There is no difference in the methodology for the high-order problem. In the low-order problem, there is an extra stage of calculations which can be interpreted as a predictor step. The weights, θ_g, that define the temporal discretization depend

on the solution from this stage. This adds extra nonlinearity to the problem in comparison to the weights of the B-E and C-N schemes which are independent of the solution.

Algorithm 3: Iteration scheme for solving multi-level system of QD equations with the monotonized-hybrid method.

---

while $t^n < t^{end}$ **do**

    while $||\Delta T^{(s)}|| > \epsilon_T ||T^{(s)}|| + \epsilon_T^*, ||\Delta E^{(s)}|| > \epsilon_E ||E^{(s)}|| + \epsilon_E^*$ **do**

        • Transport iteration: given $T^{(s)}$;

        $s = 0:\quad T^{(0)} = T^{n-1}, f_{g,\beta\gamma}^{(1/2)} = f_{g,\beta\gamma}^{n-1}$;

        if $s > 0$ **then**

            Solve time-dependent multigroup RT eqs. for $I_g^{(s+1/2)}$;

            Compute group QD factors $f_{g,\beta\gamma}^{(s+1/2)}$;

        end

        while $||\Delta T^{(l,s)}|| > \tilde{\epsilon}_T ||T^{(l,s)}|| + \tilde{\epsilon}_T^*, ||\Delta E^{(l,s)}|| > \tilde{\epsilon}_E ||E^{(l,s)}|| + \tilde{\epsilon}_E^*$ **do**

            • Multigroup low-order iteration: given $T^{(l,s)}$ and $f_{g,\beta\gamma}^{(s+1/2)}$;

            Solve MLOQD eqs. with $\theta = 1$ for $E_g^{(l+1/2,s)}$ and $\boldsymbol{F}_g^{(l+1/2,s)}$;

            Compute $\theta_g^{(l,s)}$ using L-TRAP procedure;

            Solve MLOQD eqs. with $\theta = \theta_g^{(l,s)}$ for $E_g^{(l+1,s)}$ and $\boldsymbol{F}_g^{(l+1,s)}$;

            Compute grey opacities $\bar{\varkappa}_E^{(l+1,s)}, \bar{\varkappa}_{ros}^{(l+1,s)}$ and factors $\bar{f}_{\beta\gamma}^{(l+1,s+1/2)}$;

            • Grey low-order iteration: solve GLOQD eqs. coupled with EB eq. for

              $E^{(l+1,s)}, \boldsymbol{F}^{(l+1,s)}$, and $T^{(l+1,s)}$

        end

        $T^{(s+1)} \leftarrow T^{(l+1,s)}$;

    end

    $T^n \leftarrow T^{(s+1)}$;

end

Algorithm 4 displays the iteration method when solving the MLQD equations with the RT equation in α-approximation. Compared to the Algorithm 1, there is no difference in the low-order equations. An extra calculation is required to compute the approximate rates, α_g, for each outer iteration. Since α_g is dependent on the group energy density from the low-order problem, extra nonlinearity is introduced in this method.

Algorithm 4: Iteration scheme for solving multi-level system of QD equations with RT equation in α-approximation.

---

while $t^n < t^{end}$ **do**

    while $||\Delta T^{(s)}|| > \epsilon_T ||T^{(s)}|| + \epsilon_T^*, ||\Delta E^{(s)}|| > \epsilon_E ||E^{(s)}|| + \epsilon_E^*$ **do**

        • Transport iteration: given $T^{(s)}$;

        $s = 0$: $T^{(0)} = T^{j-1}$, $f_{g,\beta\gamma}^{(1/2)} = f_{g,\beta\gamma}^{n-1}$;

        if $s > 0$ **then**

            Compute $\alpha_g^{(s)}$ with $E_g^{(n-1)}$ and $E_g^{(n,s)}$;

            Solve multigroup RT eqs. with α-approximation for $I_g^{(s+1/2)}$;

            Compute group QD factors $f_{g,\beta\gamma}^{(s+1/2)}$;

        end

        while $||\Delta T^{(l,s)}|| > \tilde{\epsilon}_T ||T^{(l,s)}|| + \tilde{\epsilon}_T^*, ||\Delta E^{(l,s)}|| > \tilde{\epsilon}_E ||E^{(l,s)}|| + \tilde{\epsilon}_E^*$ **do**

            • Multigroup low-order iteration: given $T^{(l,s)}$ and $f_{g,\beta\gamma}^{(s+1/2)}$;

            Solve MLOQD eqs. for $E_g^{(l+1,s)}$ and $\boldsymbol{F}_g^{(l+1,s)}$;

            Compute grey opacities $\bar{\varkappa}_E^{(l+1,s)}$, $\bar{\varkappa}_{ros}^{(l+1,s)}$ and factors $\bar{f}_{\beta\gamma}^{(l+1,s+1/2)}$;

            • Grey low-order iteration: solve GLOQD eqs. coupled with EB eq. for

              $E^{(l+1,s)}$, $\boldsymbol{F}^{(l+1,s)}$, and $T^{(l+1,s)}$

        end

        $T^{(s+1)} \leftarrow T^{(l+1,s)}$;

    end

    $T^n \leftarrow T^{(s+1)}$;

end

5.2   Analysis of Transport Iterations

First, the transport iterations for each MLDQ method are analyzed. Figure 5.1 shows the number of transport iterations for all considered methods as a function of time for Fleck and Cummings test case with $\tau = 2 \times 10^{-3}$ sh using the modified subcell step (MSS) method. This is done for a 10x10 spatial mesh, 17 groups, and quadruple range quadrature set [52]. The parameters of convergence criteria for transport iterations are $\epsilon_T = \epsilon_E = 10^{-7}$ and for the multigroup low-order iterations are $\tilde{\epsilon}_T = \tilde{\epsilon}_E = 10^{-8}$.

The number of transport iterations per time step is small in case of the first-order scheme. On the first time there is seven transport iterations and by ct = 10 cm there is no more than three. The hybrid scheme has a even fewer number of transport iterations with no more than three after the first time step. The monotonized hybrid scheme requires more iterations on

88

certain time steps than the first and hybrid scheme. There is also increase in number of iterations at some instants; whereas, the first order and hybrid schemes have a steady decrease in the number of transport iterations over time. The reason for the increase in iterations is that the monotonization method introduces extra nonlinearity to the problem. The procedure changes the weights of the temporal discretization based on criteria of a local monotonicity condition that depends on the solution. The behavior in the number of transport iterations is attributed to the non-smooth nature of the L-TRAP algorithm. The monotonization algorithm is discrete in nature. A slight change in the solution can impact which branch of the algorithm is used which can lead to an artificial non-convergence. This occurs rarely and with negligible impact to the solution, but does affect convergence of iterations. The number of transports iterations with the RT equation in α-approximation compared to the first-order scheme is twice as much for most moments of time. Near equilibrium, the number of transport iterations are the same. The rates α_g in the α-approximation are computed from the solution of the time-dependent MLOQD equations; thus, this method adds nonlinearity to the iteration process. The number of transport iterations does decrease montonically over time like the first-order scheme. The observed performance of transport iterations is consistent with prediction of stability analysis of the multi-level QD method for TRT problems [21].
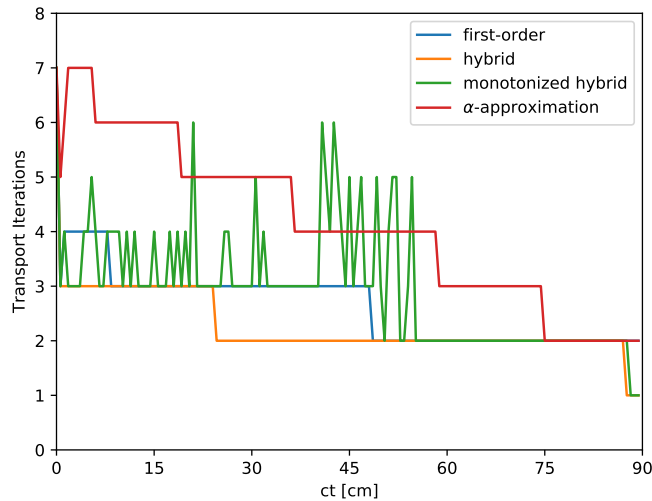

Figure 5.1 Number of transport iterations for the MLQD method discretized with first-order, hybrid, and monotonized hybrid temporal schemes, and the MLQD method with first-order discretization in time of the low-order equations and RT equation in α-approximation.

5.3　Analysis of Multigroup Low-Order Iterations

To continue, the multigroup iterations for each MLDQ method are analyzed. Figure 5.2 shows the total number of multigroup iterations on a time step. The hybrid scheme has the least number of iterations. In the early stage of wave development, α-approximation has the most multigroup iterations as a result of it having the most transport iterations. The monotonized hybrid scheme has spikes in the iterations that correspond to the time steps with spikes in transport iterations.

Figure 5.2　Number of multigroup iterations for the MLQD method discretized with first-order, hybrid, and monotonized hybrid temporal schemes, and the MLQD method with first-order discretization in time of the low-order equations and RT equation in α-approximation.

Figure 5.3 shows the average number of multigroup iterations per transport iteration. The RT equation in α-approximation has about the same average number of iterations as the first-order and hybrid scheme. The montonized hybrid scheme is close to the first-order scheme until ct = 30 cm; afterwards, the number of average multigroup iterations spikes for certain time steps. This is due to the non-smoothness of the L-TRAP algorithm. A modification to the algorithm reduces this effect. Analysis shows the weights of the temporal discretization converge after a few multigroup low-order iterations; any significant change in a weight on successive multigroup iterations occurs due to an alternating selection of paths of the L-TRAP algorithm.

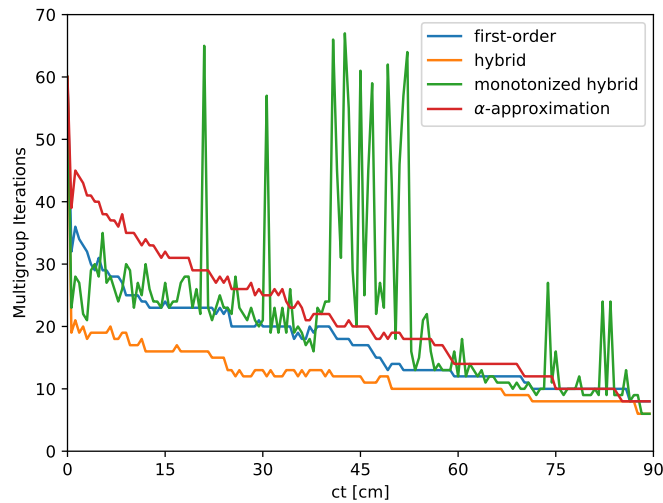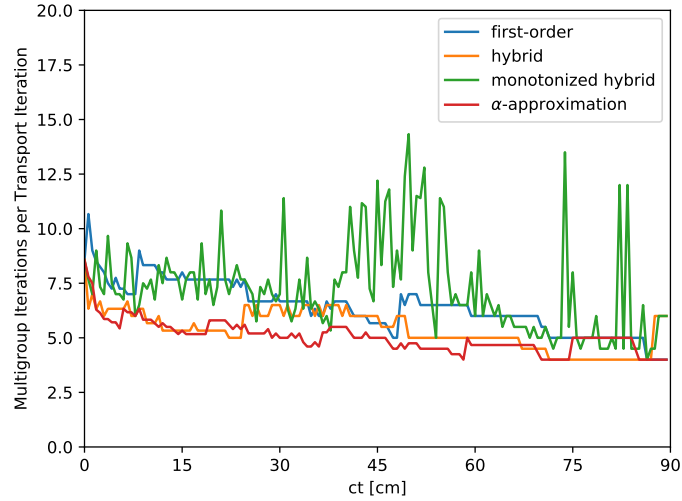**Figure 5.3** Number of multigroup iterations per transport iteration for the MLQD method discretized with first-order, hybrid, and monotonized hybrid temporal schemes, and the MLQD method with first-order discretization in time of the low-order equations and RT equation in α-approximation.

After a specified number of multigroup iterations, the weights on successive multigroup iterations are compared. If they have converged, they are used. If they have not converged, a conservative approach is taken and the weight is changed to 1. Hereafter we refer to this as modified monotonization. Since this rarely occurs (less than 1 percent), this does not have an effect on the solution but it significantly reduces the number of iterations. Figure 5.4 shows the total number of multigroup iterations where the montonized-hybrd scheme is using the modified monotonization procedure. There is a 50% decrease in iterations on the time steps that exhibit the most drastic increases. There are still more multigroup iterations in comparison to the other MLQD methods, but there is a significant decrease compared to the method with the original L-TRAP scheme. Figure 5.5 shows the average number of multigroup iterations per transport iteration where the montonized-hybrd scheme is using the modified monotonization procedure. While there is a large number of total multigroup iterations compared to the other schemes, the average number of multigroup iterations is similar to that of the first-order scheme. It is apparent that the increased total multigroup iterations corresponds to the larger number of transport iterations. The modified monotonization procedure does well in reducing the effect of the artificial increase in iterations due to the non-smooth nature of the L-TRAP scheme.

91

Figure 5.4 Number of multigroup iterations for the MLQD method discretized with first-order, hybrid, and monotonized hybrid with modified montonization temporal schemes, and the MLQD method with first-order discretization in time of the low-order equations and RT equation in α-approximation.

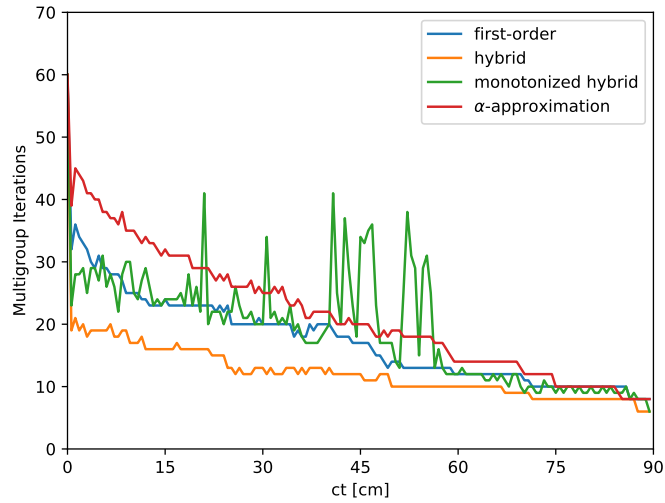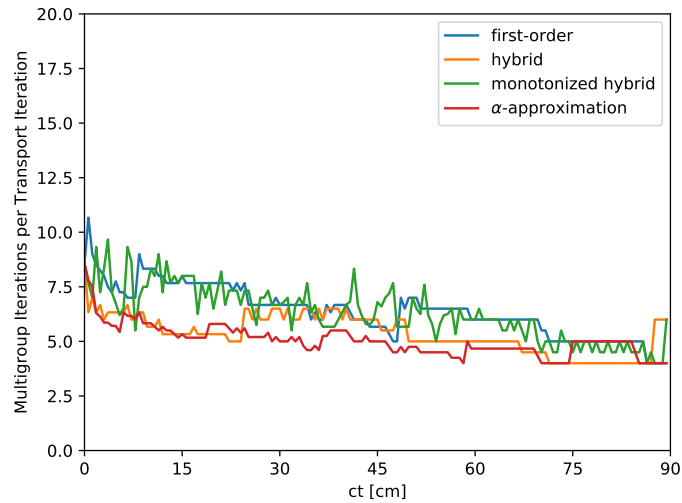**Figure 5.5** Number of multigroup iterations per transport iteration for the MLQD method discretized with first-order, hybrid, and monotonized hybrid with modified monotonization temporal schemes, and the MLQD method with first-order discretization in time of the low-order equations and RT equation in α-approximation.

92

CHAPTER

— 6 —

CONCLUSION

A hybrid temporal discretization scheme for the multilevel system of QD equations is developed. It is based on the backward Euler temporal discretization of the high-order time-dependent radiative transfer equation and a second-order scheme for the time-dependent multigroup low-order QD equations. The discretization of the grey low-order QD equations is consistent with the scheme for the multigroup low-order QD equations. The second-order scheme is applied to the energy balance equation as well. The numerical results show the hybrid scheme generates a more accurate solution compared to the first-order scheme. The hybrid scheme is a first-order accurate method in time. The L-TRAP scheme is applied to the multigroup low-order QD equations with a second-order temporal discretization to perform montonization. This procedure does well in removing the oscillatory behavior produced from the solution of hyperbolic equations discretized with a high-order scheme. The conditions that determine whether or not montonization is required are too strict in some cases. Adaptive monotonization procedures are developed to reduce the excessive work of monotonization when unnecessary. The results indicate the adaptive montonization procedures improve the accuracy of the solution compared to the L-TRAP scheme.

The time dependence of the radiative transfer equation is approximated by several models. The numerical results show that α-approximation does well in describing the evolution of temperature and radiation waves without the need to store the high-order solution from the previous time step. The solution obtained with the RT equation in α-approximation deviates

from the solution generated by the first-order scheme when there are significant transport effects and when the change rate is large. A modified α-approximation is developed based on the backward Euler temporal discretization. This method performs similarly to α-approximation in all aspects. Approximations of the intensity from the previous time step are studied as well. α-approximation generates a more accurate solution compared to these models. It also has desirable properties such as reproducing the same steady state solution at equilibrium on a given spatial grid as the one computed by the time-dependent radiative transfer equation. Both the multilevel QD method with the RT equation in α-approximation and the scheme with montonization of the low-order QD equations adds further nonlinearity to the problem. There is an increase in transport iterations, but not by a significant amount.

BIBLIOGRAPHY

[1] Chandrasekhar, S. *Radiative Transfer*. Dover Publications Inc., 1960.

[2] Shu, F. S. *The Physics of Astrophysics, Volume 1: Radiation*. University Science Books, 1991.

[3] Stamnes, K., Thomas, G. E. & Stamnes, J. J. *Radiative Transfer in the Atmosphere and Ocean*. Cambridge University Press, 2017.

[4] Pomraning, G. C. *The Equations of Radiation Hydrodynamics*. Dover Publications, Inc., 1973.

[5] Godonov, S. K. "A Difference Scheme for Numerical Solution of Discontinuous Solution of Hydrodynamic Equations". *Math. Sbornik* **47** (1959), pp. 271–306.

[6] Fleck, J. A. & Cummings, J. D. "An implicit Monte Carlo Scheme for Calculating Time and Frequency Dependent Nonlinear Radiation Transport." *J. of Comp. Phys.* **8** (1971), pp. 313–342.

[7] Fleck, J. A. *Computational Methods in the Physical Sciences*. McGraw-Hill, 1963.

[8] Campbell, P. M. & Nelson, R. G. "Numerical Methods for Nonlinear Radiation Transport Calculations". *Report UCRL-7838, Lawrence Radiation Laboratory* (1964).

[9] Gol'din, V. Y. "A Quasi-Diffusion Method of Solving the Kinetic Equation". *Comp. Math. and Math. Phys.* **4** (1964), pp. 136–149.

[10] Gol'din, V. Y. & Chetverushkin, B. N. "Methods of Solving One-Dimensional Problems of Radiation Gas Dynamics". *USSR Comput. Math. Math. Phys.* **12** (1972), pp. 177–189.

[11] Gol'din, V. Y., Gol'dina, D. A., Kolpakov, A. V. & Shilkov, A. V. "Mathematical Modeling of Hydrodynamics Processes with High-Energy Density Radiation". *Problems of Atomic Sci. & Eng.: Methods and Codes for Numerical Solution of Math. Physics Problems* **2** (1986). (in Russian), pp. 59–88.

[12] Gol'din, V. Y. & Shilkov, A. V. "Equations of High Temperature Radiative Gas Dynamics in the QD Form". *Preprint of Keldysh Institute of Applied Mathematics, USSR Academy of Sciences* **43** (1981). (in Russian).

[13] Stone, J. M., Mihalas, D. & Norman, M. L. "ZEUS-2D: A Radiation Magnetohydrodynamics Code for Astrophysical Flows in Two Space Dimensions. III. The Radiation Hydrodynamic Algorithms and Tests". *The Astrophysical J. Supp. Series* **80** (1991), pp. 819–845.

[14] Anistratov, D. "Evaluation of Transport Effects and Spatial Domain Decomposition into Transport and Diffusive Subdomains in 1D Geometry". *Trans. Am. Nucl. Soc.* **101** (2009), pp. 390–393.

[15] Anistratov, D. & Stehle, N. "Computational Transport Methodology Based on Decomposition of a Problem Domain into Transport and Diffusive Subdomains". *J. of Comp. Phys.* **231** (2012), pp. 8009–8028.

[16] Stehle, N., Anistratov, D. & Adams, M. "A Hybrid Transport-Diffusion Method for 2D Transport Problems with Diffusive Subdomains". *J. of Comp. Phys.* **270** (2014), pp. 325–344.

[17] Anistratov, D. Y., Aristova, E. N. & Gol'din, V. Y. "A Nonlinear Method for Solving Problems of Radiation Transfer in a Physical System". *Mathematical Modeling* **8:12** (1996). (in Russian), pp. 3–28.

[18] Aristova, E. N., Gol'din, V. Y. & Kolpakov, A. V. "Multidimensional Calculations of Radiation Transport by Nonlinear Quasi-Diffusion Method". *Proc. of Int. Conf. on Math. and Comp., M&C 1999, Madrid* (1999), pp. 667–676.

[19] Aristova, E. N. "Simulation of Radiation Transport in a Channel Based on the Quasidiffusion Method". *Transport Theory and Statistical Physics* **37** (2008), pp. 483–503.

[20] Park, H., Knoll, D. A., Rauenzahn, R. M., Wollaber, A. B. & Densmore, J. D. "A Consistent, Moment-Based, Multiscale Solution Approach for Thermal Radiative Transfer Problems". *Transport Theory and Statistical Physics* **41** (2012), pp. 284–303.

[21] Anistratov, D. Y. "Stability Analysis of a Multilevel Quasidiffusion Method for Thermal Radiative Transfer Problems". *Journal of Computational Physics* **376** (2019), pp. 186–209.

[22] Morel, J. E., Larsen, E. W. & Matzen, M. "A Synthetic Acceleration Scheme for Radiative Diffusion Calculations". *J. of Quantitative Spectroscopy & Radiative Transfer* **34** (1984), pp. 243–261.

[23] Reed, W. H. "The Effectiveness of Acceleration Techniques for Iterative Methods in Transport Theory". *Nuclear Science and Engineering* **45:3** (1971), pp. 245–254.

[24] Morel, J. E. "A Synthetic Acceleration Method for Discrete Ordinates Calculations with Highly Anisotropic Scattering". *Nuclear Science and Engineering* **82:1** (1982), pp. 34–46.

[25] Alcouffe, R. E. "Diffusion Synthetic Acceleration Methods for the Diamond-Differenced Discrete-Ordinates Equations". *Nuclear Science and Engineering* **64:2** (1977), pp. 344–355.

[26] Gelbard, E. M. & Hageman, L. A. "The Synthetic Method as Applied to the Sn Equations". *Nuclear Science and Engineering* **37:2** (1969), pp. 288–298.

[27] Alcouffe, R. E., Clark, B. A. & Larsen, E. W. "The Diffusion-Synthetic Acceleration of Transport Iterations, with Application to Radiation Hydrodynamics Problem". *Multiple Time Scales* (1985), pp. 145–184.

[28] Larsen, E. "A Grey Transport Acceleration Method for Time-Dependent Radiative Transfer Problems". *J. of Comp. Phys.* **78** (1988), pp. 459–480.

[29] Morel, J. E., Yang, B. T. & Warsa, J. S. "Linear Multifrequency-Grey Acceleration Recast for Preconditioned Krylov Iterations". *J. of Comp. Physics* **227** (2007), pp. 244–263.

[30] Banoczi, J. M. & Kelley, C. T. "A Fast Multilevel Algorithm for the Solution of Nonlinear Systems of Conductive-Radiative Heat Transfer Equations". *SIAM J. Sci. Comput.* **19** (1998), pp. 266–279.

[31] Banoczi, J. M. & Kelley, C. T. "A Fast Multilevel Algorithm for the Solution of Nonlinear Systems of Conductive-Radiative Heat Transfer Equations in Two Space Dimensions". *SIAM J. Sci. Comput.* **20** (1999), pp. 1214–1228.

[32] McClarren, R. G., Holloway, J. P. & Brunner, T. A. "On Solutions to P_N equations for Thermal Radiative Transfer". *J. of Comp. Physics* **227** (2008), pp. 2864–2885.

[33] McClarren, R. G., Evans, T. M., Lowrie, R. B. & Densmore, J. D. "Semi-implicit Time Integration for P_N Thermal Radiative Transfer". *J. of Comp. Physics* **227** (2008), pp. 7561–7586.

[34] Lowrie, R. B. "Numerical Analysis of Time Integration Errors for Nonequilibrium Radiation Diffusion". *J. of Comp. Phys.* **226** (2007), pp. 1332–1347.

[35] Adams, M. L. & Larsen, E. W. "Fast Iterative Methods for Discrete-Ordinates Particle Transport Calculations". *Progress in Nuclear Energy* **40** (2002), pp. 3–159.

[36] Anistratov, D. Y. & Gol'din, V. Y. "Difference Scheme Comparison for Quasi-Diffusion Transport System of Equations". *Questions of Nuclear Science and Engineering (VANT)* **17** (1986). (in Russian), pp. 17–23.

[37] Tamang, A. & Anistratov, D. Y. "A Multilevel Projective Method for Solving the Space-Time Multigroup Neutron Kinetics Equations Coupled with the Heat Transfer Equaiton". *Nuclear Science and Engineering* **177** (2014), pp. 1–18.

[38] Ghassemi, P. & Anistratov, D. Y. "Analysis of α-approximation For Nonlinear Radiative Transfer Problems". *Transactions of American Nuclear Society* **113** (2015), pp. 641–644.

[39] Ghassemi, P. & Anistratov, D. Y. "A Multilevel Quasidiffusion Method with Hybrid Temporal Discretization for Thermal Radiative Transfer Problems". *Transactions of American Nuclear Society* **118** (2018), pp. 372–375.

[40] Morel, J. E. "Diffusion-Limit Asymptotics of the Transport Equation, the $P_{1/3}$ Equations, and two flux-limited diffusion theories". *J. of Quantitative Spectroscopy & Radiative Transfer* **65** (2000), pp. 769–778.

[41] Carlson, B. G. & Bell, G. I. "Solution of the Transport Equation by the S_N method". *Proc. U. N. Intl. Conf. Peaceful Uses of Atomic Energy* **P/2386** (1958).

[42] Miller, D. J., Matthews, K. A. & Brennan, C. R. "Split-cell Discrete Ordinates Transport on an Unstructured Grid of triangular cells". *Transport Theory and Statistical Physics* **25:7** (1996), pp. 833–867.

[43] Adams, M. L. "A New Transport Discretization Scheme for Arbitrary Spatial Meshes in XY Geometry". *Proc. ANS Topical Meeting, Advances in Mathematics, Computations, and Reactor Physics, Pittsburgh* **3** (1991), pp. 1–8.

[44] Bakirova, M. I., Karpov, V. Y. & Mukhina, M. I. "A Characteristic-Interpolation Method for Solving a Transfer Equation". *Differential Equations* **22** (1986), pp. 788–794.

[45] Grove, R. E. "The Slice Balance Approach (SBA): A Characteristic-Based, Multiple Balance SN Approach on Unstructured Polyhedral Meshes". *Proceedings of International Conference on Mathematics and Computations, Supercomputing, Reactor Physics and Nuclear Biological Applications (M&C 2005)* (2003), p. 12.

[46] Eaton, T. L. & Adams, M. L. "A New Corner-Balance/Linear-Discontinuous Method for Transport in Slab Geometry". *Trans. Amer. Nucl. Soc.* **70** (1994), p. 158.

[47] Adams, M. L. "Subcell Balance Methods for Radiative Transfer on Arbitrary Grids". *Transport Theory Statist. Phys.* **26** (1997), pp. 385–431.

[48] Adams, M. L. & Nowak, P. F. "Asymptotic Analysis of a Computational Method for Time- and Frequency-Dependent Radiative Transfer". *J. of Comp. Phys.* **146** (1998), pp. 366–403.

[49] Saad, Y. *SPARSEKIT: Sparse Iterative Solver Package*. University of Minnesota, Minneapolis, 2000.

[50] Duraisamy, K., Baeder, J. D. & Liu, J. "Concepts and Application of Time-Limiters to High Resolution Schemes". *J. of Scientific Computing* **19** (2003), pp. 139–162.

[51] Hyunh, H. "Accurate Monotone Cubic Interpolation". *SIAM J. Numer. Anal.* **30** (1993), pp. 57–100.

[52] Abu-Shumays, I. K. "Angular Quadratures for Improved Transport Calculations". *Transport Theory and Statistical Physics* **30** (2001), pp. 169–204.

[53] Bowers, L. & Wilson, J. R. *Numerical Modeling in Applied Physics and Astrophysics*. Boston: Jones and Bartlett, 1991.

[54] Gol'din, V. Y., Kolpakov, A. V. & Degtyarev, V. A. "Approximate Methods for Accounting for Time-Dependent Effects in the Quasi-Diffusion Equations". *Preprint of the Keldysh Inst. of Applied Math., USSR Acad. of Sci., No. 122, 1983* **122** (1983). (in Russian).

[55] Minerbo, G. N. "Maximum Entropy Eddington Factors". *J. of Quantitative Spectroscopy & Radiative Transfer* **20** (1978), pp. 541–545.

[56] Brunner, T. A., Holloway, J. P. & Larsen, E. W. "On the Use of Maximum Entropy Eddington Factors in Shielding Calculations". *Trans. Am. Nucl. Soc.* **77** (1997), pp. 195–196.

[57] Brunner, T. A. & Holloway, J. P. "One-dimensional Riemann Solvers and the Maximum Entropy Closure". *J. of Quantitative Spectroscopy & Radiative Transfer* **69** (2001), pp. 543–566.